STUDY AND REDESIGN OF THE NSCL K500 INJECTION, CENTRAL REGION AND PHASE SELECTION SYSTEMS

By

Steven L. Snyder

A DISSERTATION

Submitted to
Michigan State University
in partial fulfillment of the requirements
for the Degree of

DOCTOR OF PHILOSOPHY

Department of Physics and Astronomy

1995

ABSTRACT

THE STUDY AND REDESIGN OF THE NSCL K500 INJECTION, CENTRAL REGION AND PHASE SELECTION SYSTEMS

The proposed K500-K1200 cyclotron coupling project calls for a redesign of both the inflector and central region of the K500 cyclotron. An increased injection voltage will be needed to reduce space charge effects in the higher-intensity beam, and in order to obtain stripping injection matching with the K1200, the K500 will need to operate in the second harmonic rf mode. To meet the requirements of this higher energy beam (and new rf mode), a new spiral inflector and central region geometry were designed. Extensive orbit code calculations have been carried out on these designs, and used to determine the overall behavior of the beam. Additionally, the calculations were used to determine the effectiveness of the K500 phase selection mechanisms in reducing the phase width of the beam and to measure the ability of the first and second harmonic buncher in increasing the current transmitted in the allowed phase width.

The new spiral inflector and central region were constructed and installed in the K500 cyclotron. During commissioning of the new systems, beam was accelerated to full energy and successfully extracted. Initial studies of the new systems showed results (in terms of phase width and transmitted current) consistent with those obtained from computer calculations.

To Mom and Dad

ACKNOWLEDGMENTS

I would like to thank Felix Marti and M.M. Gordon without whom this thesis would be 114 pages shorter.

I would like to thank whoever came up with the idea of a computerized spell-checker.

I would like to thank H. Blosser, A. Galonsky, W. Repko and W. Hartmann for serving on my guidance committee and all the help they've given me.

I would like to thank the academy, but they really weren't much of a help so I won't.

I would like to thank G. Horner, R. York and T. Grimm for actually making this work.

I would like to thank Stephanie Holland without whom my career would have been several years shorter and all of it spent at the administration building.

A big old thanks to the far seeing National Science Foundation and Michigan State University for the financial support.

Thanks to Jeff Schubert for having pictures when I didn't.

And, most importantly, I want to thank Jennifer Discenna for the endless bus rides, long drives, keeping me sane and making it all worthwhile.

Contents

List of Tables

List of Figures

Chapter 1

INTRODUCTION

The superconducting cyclotron program at the NSCL began in 1973 and in July of 1975, funds were received to build a prototype superconducting magnet for a 500 MeV cyclotron. Construction of this prototype magnet began immediately and was first successfully operated at design current in May 1977. Soon thereafter, in July of 1977, the NSF approved funds to expand the project to a full cyclotron. This cyclotron, the K500, was to be used both in a stand-alone mode and as an injector for a larger superconducting cyclotron (the K1200) to be built later. The first beams were extracted from the K500 in 1982 [1] and it became the main accelerator at the NSCL for the next eight years. At the time beam was first extracted from the K500, the coil winding had already begun for the K1200 magnet. The full plans then included the coupling of the two machines to achieve the highest energies. Initially, the K500 was designed and operated with an internal Penning ion source to provide beam which would then be injected, via foil stripping, into the K1200. However, the advent of Electron Cyclotron Resonance ion sources (ECR's) changed all of that.

Between the first successful operation of the K500 and the commissioning of its sister K1200 machine, a major advance in ion source technology sidetracked the early plan to couple the two machines. A new type of ion source (ECR) produced high-

charge-state beams which, when injected into the K1200, promised to provide a range of ions that would satisfy the demands of the experimental nuclear physics program at that time. The coupling plans were then set aside in favor of separate beam lines from ECR's to each of the K500 and (still under construction) K1200 cyclotrons.

The K500 central region was redesigned to allow for external ion source injection and between 1982 and 1989 it provided beams with a wide range of charge states and final energies. In 1988 the K1200 cyclotron was commissioned [2] and in 1989 the K500 was 'retired' from active nuclear experimental beam production. During the last two years, the K500 has been used as a test bed for improvements of the K1200 systems and more recently, has been used for a reawakened plan to couple the two machines. It is this new coupling plan (specifically the redesign of the K500 cyclotron central region) that is the focus of this thesis.

1.1 The K500⊗K1200 Coupling Project

In early 1993 the focus of the work with the K500 turned from improving the K1200 towards plans to couple the two machines [3]. The K500⊗K1200 Coupling Project will greatly enhance the NSCL's ability to deliver both high intensity-radioactive beams and high energy-heavy mass beams. The increases are achieved by injecting high-intensity, low charge state beams from the ECR ion source into the K500, which will accelerate the beam to energies of $2-16.6$ MeV/u. These low energy beams are then injected into the K1200 via stripping and the resultant high charge states accelerated to full energy. This mode of operation will increase the achievable intensities for light ions (A<40) by an estimated factor of 100-1000 while also providing a 2-4 fold increase in energy for heavier beams [4].

To carry out the coupling of the K500 and K1200 cyclotrons, and achieve the above

noted gains, changes to several system components will be required. Modification of the ECR, K500, K1200 and the fragment separator (which follows the extraction system of the K1200) will all be necessary. The work described here addresses the design, construction and initial testing of the new K500 injection and central region systems required by the project.

1.2 The K500 Cyclotron

The K500 cyclotron was the first cyclotron to use superconducting main coils. There are two pairs of these coils driving the magnet which can provide a maximum magnetic field in the range of 3-5 Tesla. The machine is termed the K500 in reference to its maximum bending strength, K which is 520 MeV and it has a focusing limit of $K_f = 160$ MeV. This corresponds to a limit on the energy per nucleon of $K(Q/A)^2$ or $K_f(Q/A)$, whichever is smaller. Here Q and A are the charge (q/e) and mass number of the ion being accelerated. The main field produced by the superconducting coils is modified by 14 independent, room temperature trim coils and azimuthally varied over three magnetic sectors by the introduction of three spiraled pole tips. The rf accelerating voltage operates in a range of 9-27 MHz and is provided by three spiral dees located in the valleys between the pole tips. Figure 1.1 shows the range of charge states and final energies which the K500 can produce. This operating diagram for the K500 depicts both the machine limits and the region of the diagram which will be used for operations under the coupled project.

The redesign of the K500 systems for the K500⊗K1200 project are motivated by the corresponding changes in the ECR operation, the frequency requirements for coupling the two cyclotrons, and the intensity increases on which the entire project is based. Each of these considerations places its own restrictions on the design and

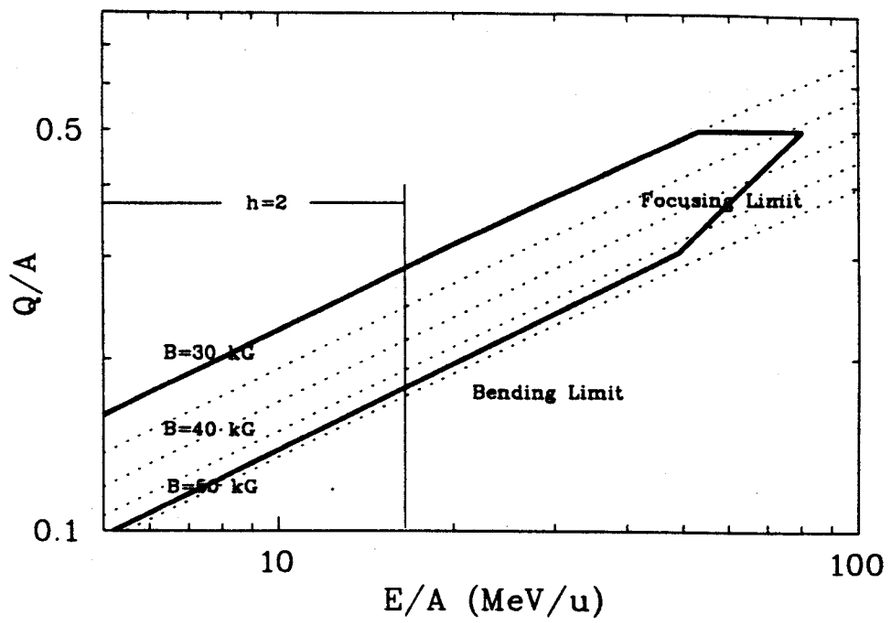

Figure 1.1: The operating diagram for the K500.

operating characteristics of the K500 axial injection, central region and phase selection systems.

Axial Injection

A planned change in the ECR extraction voltage will, in turn, require a redesign of the K500 injection system. The maximum ECR extraction voltage will be raised from 18 to 30 kV in order to increase the source brightness, and the corresponding energy increase of the beam going from the ECR into the K500 will reduce space charge effects in the transfer line and spiral inflector. The beam from the ECR is transported horizontally to a position under the K500 where it is bent upward onto the machine's magnetic axis via a 90° bending magnet, finally arriving at a further bending device which guides the beam into the cyclotron median plane (see figure 1.2). The design of the bending device (a spiral inflector) is determined by

the energy of the incoming beam and the central magnetic field of the cyclotron. The increase in the ECR injection voltage therefore requires the redesign of the K500 spiral inflector to account for the new, higher-energy beam. The redesign will also provide an opportunity to increase the electrode separation in the inflector from the 4 mm found in the present design to 6 mm. This increased aperture will result in a larger acceptance allowing more of the injected beam to enter the cyclotron.

Central Region

The new inflector will sit in a redesigned, second harmonic central region. Second harmonic refers to the ratio of the frequency of the RF accelerating voltage, f_{rf}, to the ion's orbital frequency, f_0. The harmonic number, h is then given by,

$$\begin{aligned} f_{rf} &= h f_0, \\ &\text{where} \\ f_0 = \frac{\omega_0}{2\pi} &\quad \text{with} \quad \omega_0 = \frac{qB_0}{m}. \end{aligned} \tag{1.1}$$

Here, B_0 is the isochronous value of the magnetic field at the center of the machine, q is the particle charge and m is the rest mass. The K500 was traditionally operated in first harmonic ($h = 1$) but, for the coupled cyclotron project, this was increased to second ($h = 2$). The reasons for this switch are associated with both the beam behavior in the K500 and, after transfer, during injection into the K1200. In the coupled mode the K1200 cyclotron acts as a booster for the beam extracted from the K500. In the booster then, the velocity of the injected beam is multiplied by a factor of,

$$M_v = \frac{\beta_f}{\beta_i} = \frac{v_f}{v_i} = \frac{R_f}{R_i}, \tag{1.2}$$

where R_i and R_f are the initial and final average radii of the particle. R_f is the extraction radius of 1.0 m for the K1200, thus to increase M_v, the injection radius

should be as small as possible. The injection radius in the K1200 ($R_{i_{1200}}$) is set by the properties of the beam extracted from the K500. Denoting the RF and orbital frequencies by f_{rf} and f_0 respectively, we can write, for either machine,

$$f_{rf} = hf_0 = \frac{h\beta c}{2\pi R} \Longrightarrow \beta = \frac{2\pi f_{rf} R}{hc}, \tag{1.3}$$

where h is the harmonic number. In order for the particle bunches extracted from the K500 to be accelerated in the K1200, the two RF frequencies must be related by

$$f_{rf_{1200}} = k f_{rf_{500}},$$

where k is an integer. Since $\beta_{f_{500}} = \beta_{i_{1200}}$, we can write (using equations 1.2 and 1.3),

$$\frac{f_{rf_{500}} R_{f_{500}}}{h_{500}} = \frac{f_{rf_{1200}} R_{f_{1200}}}{h_{1200}} \Longrightarrow R_{i_{1200}} = \frac{h_{1200}}{h_{500}} \frac{R_{f_{500}}}{k}. \tag{1.4}$$

Since the extraction radius of the K500 is set at 66.0 cm, there are then three variables with which we can change $R_{i_{1200}}$ and, in turn, the multiplicative factor of the booster cyclotron. The choice of these parameters was determined by the merits associated with changing the K500 to second harmonic.

While the increase in harmonic number is necessary for injection into the K1200 , it also has several additional advantages, the two most relevant to the work described here are the increase in the size of the first turn radius and the increase in the speed of resonance crossings. Gordon [5] has shown that the maximum voltage seen by a particle in one revolution is given by

$$V = 2V_{dee} N_{dee} \sin(\frac{hD}{2}), \tag{1.5}$$

where V_{dee} is the voltage on any one dee, N_{dee} is the number of dees each of which has an angular width D and h is the harmonic number. The sine factor then gives the efficiency of the RF. The accelerating structures in the K500 consist of three 60° dees occupying the valley regions of the magnet gap so that an increase in harmonic

number from $h = 1$ to $h = 2$ translates into a change in efficiency from 50% to nearly 87%. The higher efficiency means both a larger first turn radius and smaller number of turns in the machine. The larger radius of the first turn provides more space for the central region electrodes and inflector housing, while the decrease in the number of turns necessary to reach extraction, means a reduction in vacuum attenuation, a reduction in beam loss on the extraction septum, and an increase in the speed with which the various resonances are crossed. Thus there are measurable gains to be made by choosing $h_{500} = 2$.

To choose the final two parameters (k and h_{1200}) we consider the pragmatic problems associated with reducing the K1200 injection radius. Upon injection into the K1200 cyclotron, the beam will be stripped by means of a carbon foil. The mechanism used to insert and change foils will sit inside one of the dees at the injection radius $R_{i_{1200}}$ which, for ease in construction of the foil mechanism, will be fixed. Since the physical size of the dee shrinks with decreasing radius, the smaller the injection radius, the less space will be available for the stripper foil mechanism. Therefore, this must be taken into consideration when deciding on the parameter values which will determine the injection radius in the K1200. If we hold $h_{500} = 2$, the largest $R_{i_{1200}}$ possible will be 33.0 cm. This location moves the stripper mechanism away from the edge of the dee (simplifying its design) while still maintaining a factor of 3 increase in velocity in the booster machine (see equation 1.2). Therefore, the final two parameters are set at $h_{1200} = k = 1$, which means that the RF frequency is the same for both machines.

Phase Selection and Transmitted Current

Added to the above considerations concerning the necessary changes to the axial injection and central region systems, is the constraint of maximizing the transmitted

current while limiting the phase spread of the beam. To determine these constraints, we start with the energy gain per turn in the K500 given by

$$\frac{dE}{dn} = qV\cos(\phi) \tag{1.6}$$

where V is defined above and

$$\phi = \langle \omega_{rf} t - h\theta \rangle. \tag{1.7}$$

Here, ϕ is the phase of the particle with respect to the RF voltage with the average taken over many gap crossings [5], and $\omega_{rf} = h\omega_0$ is the angular frequency of the RF. In the case of 16.6 MeV/u O^{+3} ions for example, this translates (with a chosen dee voltage of 70 kV, see Chapter 3 and $V = 364$ kV) into about 250 turns to reach the full energy. The end result of these turns is supposed to be the complete extraction of the entire beam during the final turn. This single turn extraction is desirable so as to eliminate high-energy beam losses and reduce activation inside the cyclotron. For such extraction to be possible, the physical size of the beam must be controlled so that there is sufficient radial spacing between the final two turns. To achieve this, the angular width of the individual turns is limited by phase selection.

Phase selection works by limiting the temporal spread of the beam. Recalling that the energy gain per turn is proportional to $\cos(\phi)$, one sees that a spread in the ϕ values of particles in a particular turn translates into a corresponding spread in the energy. To determine a limit on the $\Delta\phi$ permissible, we adopt the criterion that the energy spread of a particular turn at extraction should be no more than one quarter the energy difference between consecutive turns. That is,

$$\Delta E \leq \frac{E_f}{4N}, \tag{1.8}$$

where we have approximated the average energy gain per turn by $\frac{E_f}{N}$ with N being the number of turns in the machine. According to Gordon [6], the fractional energy

spread generated by a phase width $\Delta\phi$ is given by,

$$\frac{\Delta E}{E_f} = \frac{(\Delta\phi)^2}{8}, \tag{1.9}$$

provided that the RF frequency has been adjusted such that ions with $\Delta\phi = 0$ have the maximum energy gain. When this result is combined with equation 1.8 we get,

$$\Delta\phi \leq (\frac{2}{N})^{\frac{1}{2}}. \tag{1.10}$$

Thus for the 250 turns needed in the K500, we have $\Delta\phi \leq 5.1°$ for the full width. This limit does not account for any growth in the energy spread of the beam due to longitudinal space charge forces, and this effect may further change the allowable phase width of the beam. As a reasonable limit we will choose a bunch length of 5° or 2.5° FWHM (assuming a triangular distribution).

Several types of phase selection have been used at the NSCL. In the original K50 cyclotron (a predecessor of the K500), both a phase dependant radial centering error and the phase dependant axial focusing properties were exploited [7]. The axial phase selection worked by placing a vertical window slit at the node of a particular ϕ dependant z oscillation [8]. The radial phase selection utilized an observed E-ϕ correlation in the beam. By placing radial window slits in the beam path at the $n = \frac{1}{2}, 18, and 28$ turns, it was shown [9] [7] that unwanted phases could be removed. The cause of this correlation is due to a change in phase produced by the variation of the field from its isochronous value. In a circularly symmetric isochronous cyclotron the value of the average field, $\bar{B}$ is given by,

$$\bar{B}_{isoch} = \gamma(R)B_0 = B_0[1 - (\frac{R\omega_0}{c})^2]^{-\frac{1}{2}}, \tag{1.11}$$

where $B_0 = \frac{m\omega_0}{q}$ is the isochronous field at R=0, and $h\omega_0 = \omega_{rf}$. The phase change per turn is given by

$$\frac{d\phi}{dn} = 2\pi(\frac{\omega_{rf}}{\omega} - h), \tag{1.12}$$

where ω is the angular frequency of the particle which, when $\bar{B} = B_{isoch}$ gives $h\omega = \omega_{rf}$ and $\frac{d\phi}{dn} = 0$. When $\bar{B}(R)$ varies from B_{isoch}, $h\omega \neq \omega_{rf}$ and we have a changing ϕ. Recalling the relation between the energy gain per turn and the phase (equation 1.7) we obtain the following equation relating E and ϕ,

$$\frac{dE}{d\phi} = \frac{dE}{dn}\frac{dn}{d\phi} = \frac{qV\cos(\phi)}{2\pi(\frac{\omega_{rf}}{\omega} - h)} \tag{1.13}$$

which upon integration yields,

$$\sin(\phi) = \sin(\phi_0) + \frac{2\pi h}{qV}\int_{E_0}^{E}(\frac{\omega_0}{\omega} - 1)dE, \tag{1.14}$$

where we have replaced $\frac{\omega_{rf}}{h}$ with ω_0. Collins has shown [7] that the energy spread within a turn caused by acceleration in a non-isochronous field is, to first order,

$$\Delta E = -\Delta\phi\int_{E_0}^{E}\sin(\phi)dE, \tag{1.15}$$

where $\Delta\phi$ is the phase spread at the starting energy and $\sin(\phi)$ is given by equation 1.14 above. These equations show that the energy spread at any particular energy can be modified by moving the field away from its isochronous value. Figure 1.3 shows both the actual K500 magnetic field and its isochronous value as well as $\sin(\phi)$ for a 16.6 MeV/u O^{+3} beam.

This effect was exploited in the K500 by Milton [10] for the purpose of reducing the phase width of the beam. Since the energy spread given in equation 1.15 is cumulative, the field may be shaped such that a large r-ϕ correlation is achieved at one radius while at some later radius (before extraction) the value of $\int_{E_0}^{E}\sin(\phi)dE$ returns to zero. In the K500 this was done to provide a maximum in the r-ϕ correlation at $r = 18$ cm where a set of adjustable intercepting phase pins are inserted through holes drilled in the centers of consecutive hills. Milton showed that by properly positioning these pins, rays with large $\Delta\phi$ could be intercepted, thus reducing the phase width of the beam from 20° to 4° FWHM [10].

This same method for reducing the phase width will be used in the refurbished K500. However, by reducing the phase width of the beam, we also reduce the amount of transmitted current. So, the two conditions (high intensity, small phase width) are at odds with each other. To help relieve the situation, the K500 is equipped with a buncher located along the vertical beam line just below the K500 yoke. The device takes the input DC beam and compresses its time spread in order to increase the amount of current in the appropriate phase width. The axial injection system and the central region must therefore be designed such that the bunched beam is transmitted in such a way that the currents (after the phase width is reduced) meet the K500⊗K1200 coupling project requirements. This condition is then added to those already discussed concerning the axial injection and second harmonic central region.

1.3 Chapter Overview

The following chapters describe the design of the K500 axial injection and central region systems to meet the above requirements of the K500⊗K1200 coupling project. The studies cover design considerations, beam behavior, construction and initial commissioning of the new system and are divided into the following chapters:

- Chapter 2 - Computational design of the new spiral inflector and simulations of its performance. Calculations of the beam behavior through the axial injection system are presented as are comparisons between the acceptances of the new and old systems. The new inflector design shows an increased acceptance.

- Chapter 3 - Mechanical design of the new second harmonic central region. The design process is described along with initial orbit calculations. Both the radial and vertical motion of reference rays are discussed. The calculations show

that the new design provides a well-centered beam with good vertical focusing properties.

- Chapter 4 - Beam dynamics for the full system. Calculated machine acceptance, phase selection and beam transmission properties are reported here. Additionally, the buncher performance is evaluated as are the turn separation and emittance at extraction. The results show a minimal centering error and that 6% of the input DC beam reaches extraction in the allowable phase width. With the use of an extraction bump good turn separation is obtained at extraction.

- Chapters 5 and 6 - Construction and commissioning of new systems. The production of the inflector and central region designs are discussed along with experimental results from initial runs with the new designs installed. Beam has been successfully accelerated up to full energy with the new designs and the phase width has been reduced to 3° FWHM. Comparisons with the computer calculations show remarkable agreement.

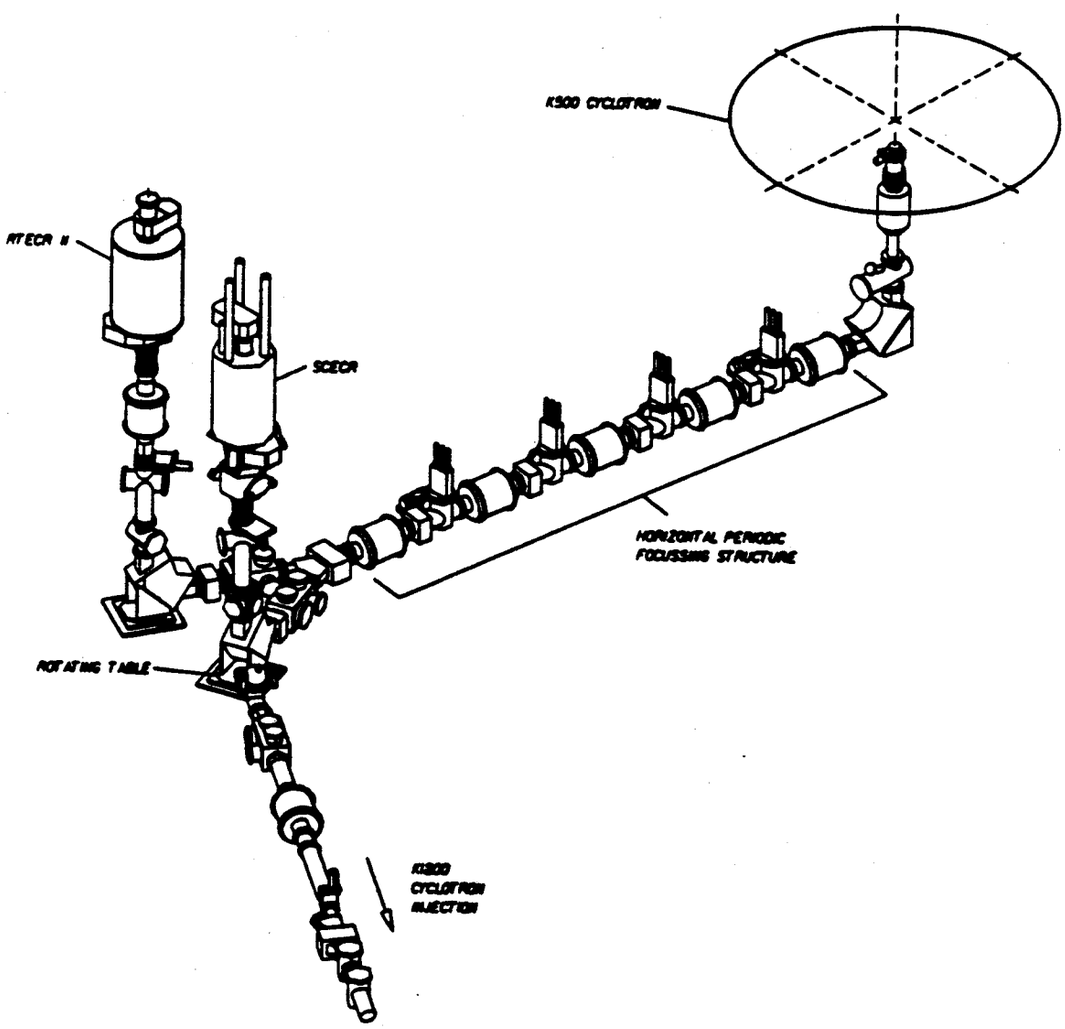

Figure 1.2: The ECR to K500 beam line for the coupled cyclotron project.

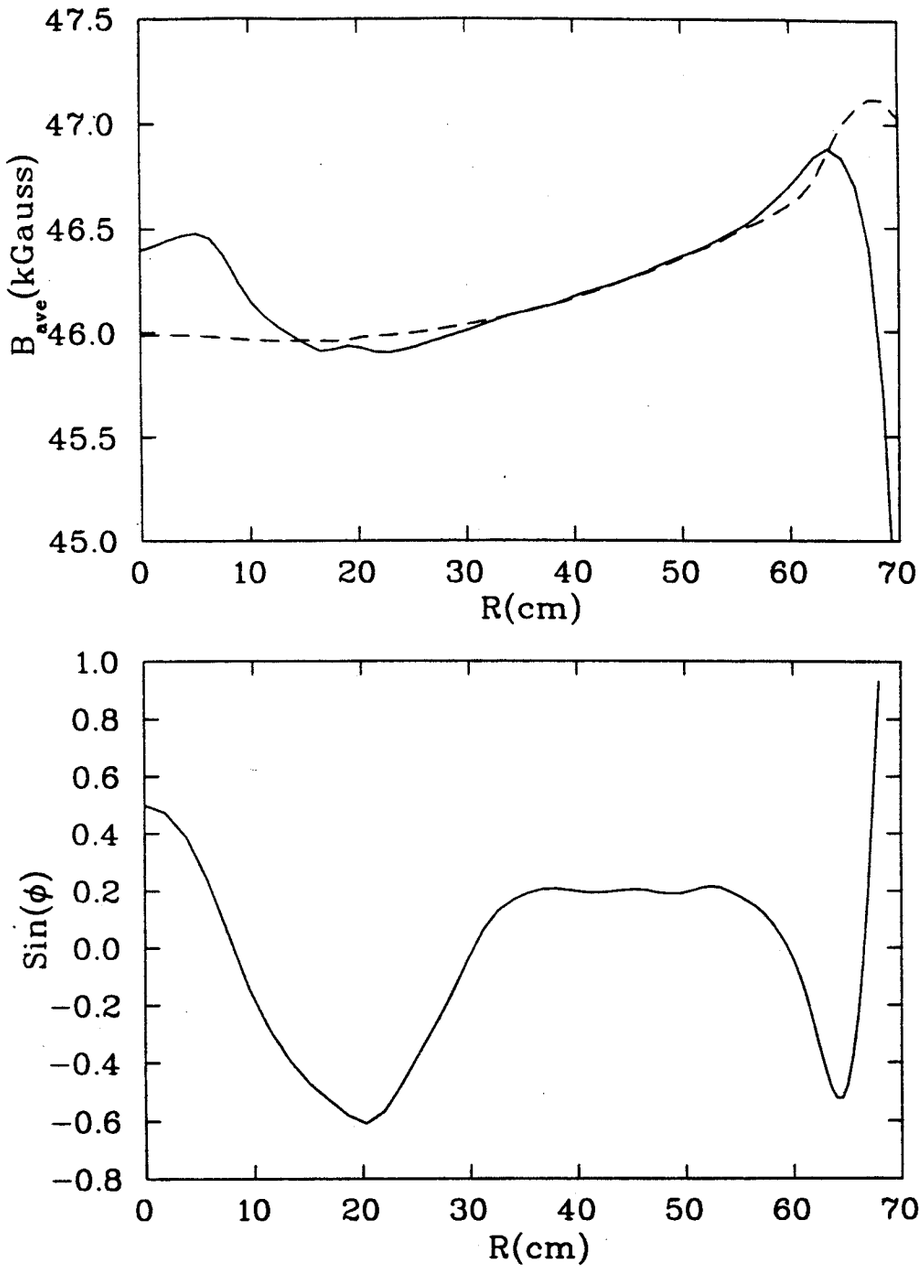

Figure 1.3: Top: The adjusted (solid) and isochronous (dashed) average magnetic field of the K500. The adjusted field will result in a larger phase dependant energy spread (and resulting radial spread) than the the isochronous case. Bottom: Phase vs. R for the length of the machine. Notice that the the phase is pushed negative before the phase pins which are at 18 cm. we would like $\sin(\phi)$ to return positive shortly after the pins, however in this case we are limited by the power of the trim coils.

Chapter 2

INFLECTOR DESIGN

The initial operation of the the K500 cyclotron called for an internal Penning ion source with a first harmonic central region. Ions were pulled from the source by the first set of dee tip electrodes, aptly referred to as the puller. After passing through the puller electrodes the beam continued on its way through the central region and then out into the machine proper. For axial injection from the ECR, the central region was changed in 1985 to include a spiral inflector in place of the ion source [17, 18]. The spiral inflector is a set of electrodes which provide an electric field used to bend the axially injected beam onto the horizontal median plane. The shape of these electrodes is determined by the energy of the injected beam and the central field of the K500.

The proposed K500⊗K1200 coupling project calls for an increased intensity in the K500 injected beam. Considering the space charge limitations on the intensity, a higher energy beam (5.6 keV/u for O^{+3} vs 3.38 keV/u based on an increase in the ECR voltage from 18 to 30 kV) will be needed for injection into the K500. This higher energy, higher intensity beam calls for the design of a new inflector to meet these needs. The design is restricted by the central region which limits the radial size of the inflector to 2.0 cm (so as to fit into the first-turn radius) and requires flexibility in the positioning of the orbit center of emerging ions. A spiral inflector was studied

based on the one presently used in the K1200 [17]. An increase in the axial height (for ease in construction) and gap size (for improved acceptance) over the present inflector were studied and comparisons of the two inflectors made. Acceptances in initially uncoupled x,p_x and y,p_y phase spaces were calculated as were the effects of changing the axial field of the magnet by way of a solenoid along the injection route.

2.1 Inflector Requirements and Features

As the beam is delivered from the ECR up the cyclotron axis, the purpose of the inflector is to bend the beam by 90° from its axial path into the cyclotron median plane. There are a number of devices which could provide the required bending, each with its own advantages and limitations [20] [21] [22]. Initial studies at the NSCL for axial injection [23] [18] into the K500 and K1200 focused on the electrostatic mirror [22] and spiral inflector [21] designs. A comparison of the two methods [24] determined that the fields required by the electrostatic mirror coupled with the spiral inflector's ability to position the exiting orbit made the latter a better choice. In March of 1986 the K500 axial injection system became operational with a spiral inflector as the bending device [24] and was operated in this mode until 1990. The success of this system [1] led to the choice of the spiral inflector as the bending method in the new design.

The spiral inflector was first described by Belmont, Pabot and Root [21] [25], who first calculated the equations of motion through the inflector. The design parameters of a spiral inflector are determined by the required exit radius of the reference orbit and the radius of the first turn in the cyclotron (thereby determining the maximum size for the inflector casing). The spiral inflector equations described by Belmont and Pabot [21] can be used to determine an appropriate electric field and inflector shape

to best match the required machine parameters. The parameters which define the inflector shape are:

$$\rho_m = \frac{p}{qB}, \quad K = \frac{A}{2\rho_m}, \ and \ A = \frac{2E}{q\epsilon}, \tag{2.1}$$

where,

ρ_m = magnetic radius of curvature

q = ion charge

B = magnetic field

E = ion energy

ϵ = electric field in the inflector

A = the electric radius of curvature,

and K is a factor related to the amount of spiral for the central ray. Thus, once the injection energy and magnetic field have been chosen, we still have the value of A (inversely proportional to the electric field) to use in determining the size and shape of the inflector. Figure 2.1 shows the dependence of the axial height of the inflector and the final radius for the reference orbit on electric field for an injection energy of 5.6 keV. An inflector field of 20 kV/cm was chosen to maximize the final radius in a 4.6 Tesla central field (ρ_m = 1.24 cm). This results in a 1.96 cm final (inflector exit) central ray radius and an inflector height of 3.00 cm. In order to determine the overall shape of the inflector, the paths of the reference ray and four additional displaced rays representing the four outer corners of the inflector electrodes were considered. To have a sufficient good-field-region in the inflector, the electrode width was chosen to be twice the gap. Thus for the 6 mm gap considered here an electrode width of

12 mm was used. This will provide an approximately 6 mm wide good-field-region in the inflector. The appropriate equations [21] used to determine these paths are

$$\begin{aligned} x &= \frac{A}{2}\left[\frac{2}{1-4K^2} + \frac{\cos(2K-1)b}{2K-1} - \frac{\cos(2K+1)b}{2K+1}\right] \\ y &= \frac{A}{2}\left[\frac{\sin(2K+1)b}{2K+1} - \frac{\cos(2K-1)b}{2K-1}\right] \qquad (2.2) \end{aligned}$$

and

$$z = -A\sin(b),$$

where b is a dimensionless parameter ranging from 0 to $\frac{\pi}{2}$ such that the path length $s = Ab$, and $z = 0$ at the K500 median plane. Surrounding the boundary determined by these five rays by a 1 mm thick housing (2 mm separation between electrodes and housing) resulted in the final inflector outline shown in figure 2.2 as it will sit in the second harmonic central region.

2.1.1 Inflector Optics

The optical properties of spiral inflectors have been the subject of many studies [25] [26] [27] [28] [29] that focused mostly on the use of transfer matrices to calculate particle behavior. These studies concerned themselves with large inflector designs used in the transport of H^- ions. Early studies done at the NSCL for the small inflectors required by superconducting cyclotrons showed that the close approach of the beam to the inflector electrodes inherent in such designs resulted in higher order effects, neglected in the matrix formalism, being readily observable [24]. As a result, these matrix methods were set aside in favor of a numerical integration of the appropriate equations of motion to calculate particle trajectories through both the inflector and the preceding axial field. While this is many times slower than the matrix transfer methods, such as that used in TRANSPORTR [30], recent advances in computing speed make numerical integration both useful and pragmatic.

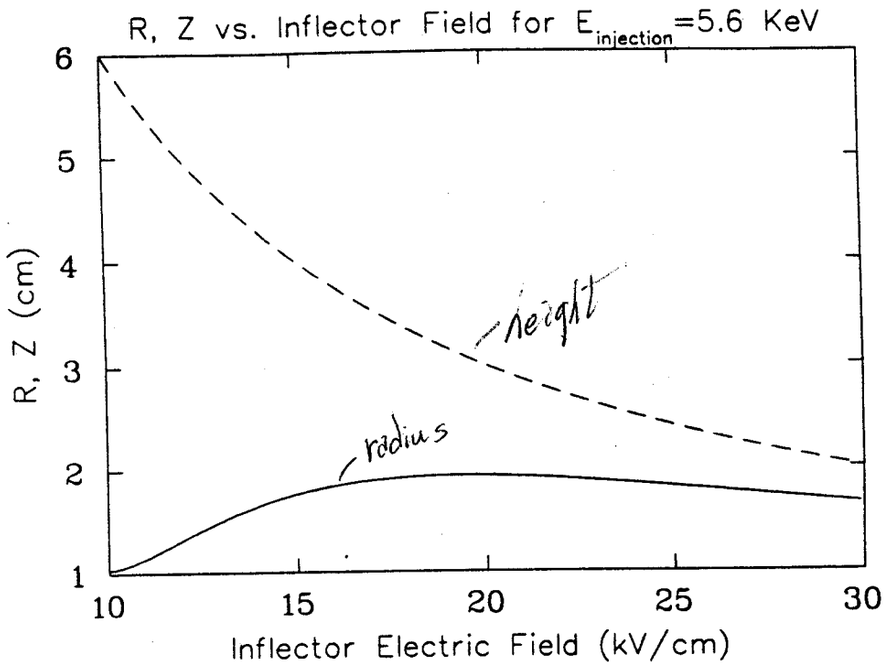

Figure 2.1: The dependence of inflector height (dashed) and exit radius (solid) on inflector electric field. A larger value for the height aids in the construction of the electrodes while a large exit radius is required by the second harmonic central region.

To study the optical properties of the axial injection and spiral inflector system, ions were tracked from 3 m below the cyclotron median plane through the inflector. This was accomplished using two ray-tracing codes MYAXIAL and INFLECTOR [31] which integrate the equations of motion for ions moving up the axis of the cyclotron magnetic field and then between the inflector electrodes.

Traversal of the Fringe and Yoke Fields

The orbit code MYAXIAL is used to track orbits during passage through the K500 fringe and yoke fields. The equations of motion used by MYAXIAL come from considering a particle moving under the influence of electric and magnetic fields with momentum $\mathbf{p}$ encountering a force according to $\mathbf{F} = q\mathbf{E} + q\mathbf{v} \times \mathbf{B}$. Thus, in terms of

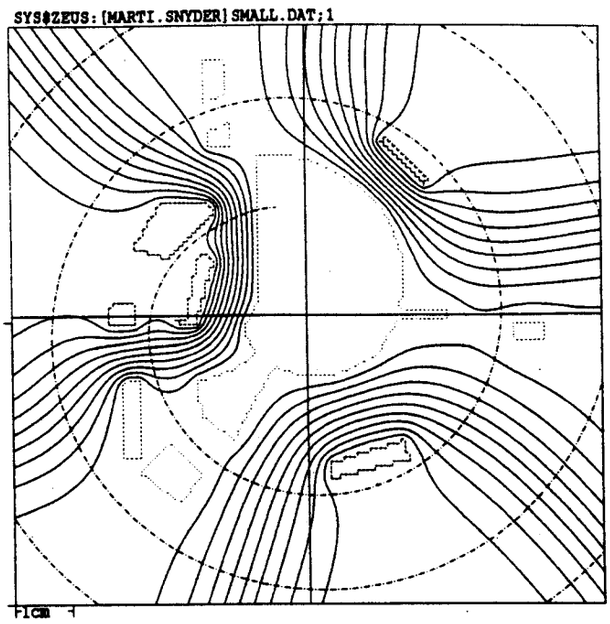

Figure 2.2: The second harmonic central region. The large structure in the center is the inflector housing. Also shown is the central ray reference orbit.

p we have,

$$\frac{d\mathbf{p}}{dt} = q\mathbf{E} + q\mathbf{v} \times \mathbf{B},$$

or with,

$$dz = v_z dt,$$

$$\frac{d\mathbf{p}}{dz} = \frac{q}{v_z}\mathbf{E} + \frac{q\mathbf{v}}{v_z} \times \mathbf{B}.$$

This yields the following equations of motion where $x' = \frac{dx}{dz}$ and so on;

$$\begin{aligned} x'(z) &= \frac{p_x}{p_z},\ y'(z) = \frac{p_y}{p_z},\ t'(z) = \frac{m\gamma}{p_z} \\ &\textit{and} \\ p'_x(z) &= q[\frac{m\gamma}{p_z}E_x + \frac{p_y}{p_z}B_z - B_y] \\ p'_y(z) &= q[\frac{m\gamma}{p_z}E_y + B_x - \frac{p_x}{p_z}B_z] \\ p'_z(z) &= q[\frac{m\gamma}{p_z}E_z + \frac{p_x}{p_z}B_y - \frac{p_y}{p_z}B_x]. \end{aligned} \tag{2.3}$$

(2.4)

Converting these momenta to units of length by dividing by $m\omega_0 = qB_0$ gives us,

$$\begin{aligned} p_x'(z) &= [\frac{\gamma}{\omega_0 B_0 p_z} E_x + \frac{p_y}{p_z}\frac{B_z}{B_0} - \frac{B_y}{B_0}] \\ p_y'(z) &= [\frac{\gamma}{\omega_0 B_0 p_z} E_y + \frac{B_x}{B_0} - \frac{p_x}{p_z}\frac{B_z}{B_0}] \\ p_z'(z) &= [\frac{\gamma}{\omega_0 B_0 p_z} E_z + \frac{p_x}{p_z}\frac{B_y}{B_0} - \frac{p_y}{p_z}\frac{B_x}{B_0}], \end{aligned} \tag{2.5}$$

where again, B_0 is the reference magnetic field which gives rise to an orbital frequency ω_0. These then, are the equations of motion using kinetic coordinates. The code MYAXIAL integrates these equations along the vertical beam line.

The on-axis magnetic fields required by MYAXIAL were provided for a 16.6 MeV/u O^{+3} beam by POISSON [32, 33] using coil currents of 667.77A and 659.47A for the K500 small and large coils, respectively. To calculate the off-axis fields we consider the vector potential for an axially symmetric field in cylindrical coordinates (r,ϕ,z),

$$\begin{aligned} A_\phi &= \frac{1}{r}\int_0^r r B_z dr \\ A_r &= A_z = 0, \\ B_r = -\frac{\partial A_\phi}{\partial z},\ B_z &= \frac{1}{r}\frac{\partial}{\partial r}(rA_\phi),\ \textit{and}\ B_\phi = 0. \end{aligned} \tag{2.6}$$

If we expand A_ϕ in a power series [34] we get,

$$A_\phi = \frac{r}{2}\sum_{n=0}^{\infty}\frac{1}{n!(n+1)!}(-\frac{r^2}{4})^n B^{2n}(z) = \frac{r}{2}B(z) - \frac{r^3}{16}\frac{\partial^2 B(z)}{\partial z^2} + \cdots. \tag{2.7}$$

Then by combining this with equation 2.7 above we arrive at (to third order in r),

$$\begin{aligned} B_z(z,r) &= B(z) - \frac{r^2}{4}\frac{\partial^2 B(z)}{\partial z^2} + O(r^4) \\ &\textit{and} \\ B_r(z,r) &= -\frac{r}{2}(\frac{\partial B(z)}{\partial z} - \frac{r^2}{8}\frac{\partial^3 B(z)}{\partial z^3}) + O(r^5). \end{aligned} \tag{2.8}$$

The code offers a choice of either a linear (in r) or nonlinear (up to O(r^3)) evaluation of the fields. MYAXIAL also includes the effects of additional elements (solenoid, quadrupole, electrostatic deflectors) but only the main field and a single solenoid were used in these calculations.

It should be noted that the equations of motion described above are in kinetic coordinates, that is the momenta are non-canonical. This is of some concern, as Liouville's theorem concerning the conservation of the volume of points in phase space applies only to canonical coordinates. We therefore need a transformation between the kinetic and canonical coordinates.

The transformation between kinetic and canonical variables is given by x,y,z→x,y,z and **p**→**P**-q**A**. For an axially symmetric field we have $\mathbf{A} = A_\phi$ and

$$A_x = -\frac{y}{r}A_\phi,\ A_y = \frac{x}{r}A_\phi,\ A_z = 0.$$

with A_ϕ given by equation 2.7 above. Using this in our coordinate transformation (and using just the linear terms for the fields) results in,

$$P_x = p_x - \frac{qyB}{2},\ P_y = p_y + \frac{qxB}{2},\ and\ P_z = p_z. \tag{2.9}$$

The canonical momentum P_t conjugate to the time t is,

$$P_t = -[(\gamma - 1)mc^2 + q\Phi],$$

where Φ is the scalar potential. Since there are only static fields here, P_t is a constant of the motion and therefore the six-dimensional phase space (x,y,t,P_x,P_y,P_t) reduces to four dimensions (x,y,P_x,P_y). It should be noted that according to this transformation between coordinates, after the beam has been bent into the median plane of the magnetic field, the kinetic and canonical coordinates for the reference ray ($z = 0$ at inflector exit) coincide (the momentum is perpendicular to the vector

potential), as do the coordinates in the non field region at the injection point ($\mathbf{A} = 0$ at $z = -3.0$ m) [23]. Considering the axial symmetry of the field, the choice of cartesian coordinates may seem counter-intuitive. A more natural choice would seem to be to use polar coordinates (r,ϕ), as ϕ is then cyclic and P_ϕ is a constant of the motion. In this case then, the 4D phase space reduces to two dimensions (r ,P_r), and since $A_r = 0$, we have $P_r = p_r$. However, passage through the inflector destroys the axial symmetry of the system and since we intend to study the axial injection system as a whole, cartesian coordinates are used throughout. However, the value of P_ϕ was calculated and used to check the accuracy of the code. As mentioned above, P_ϕ is a constant of the motion and the values returned by MYAXIAL agreed with this to about 0.01%.

The use of cartesian coordinates presents a problem in that in these coordinates there exists a coupling between the two transverse phase spaces (see equation 2.4). This coupling results in an increase in emittance in each of the transverse spaces [23]. This is due to the fact that Liouville's theorem applies to the conservation of the volume in the 4d phase space defined by x, P_x, y, and P_y, not the projection of this volume onto the transverse spaces. However, most of the coupling may be eliminated by changing to a rotating coordinate system. This system (called the Larmor frame) rotates with the beam's traversal of the axial field and makes an angle $\mu(z)$ with the stationary cartesian system defined by

$$\mu(z) = -\frac{1}{2}\int_{z_0}^{z} \frac{qB_z}{p_z} dz. \tag{2.10}$$

By transforming from the stationary system to the Larmor frame, most of the coupling induced by the magnetic field between the transverse phase spaces can be eliminated, thus resulting in near zero emittance growth for transport through the axial magnetic

field for initially uncoupled x and y spaces. The appropriate transformation is then,

$$\begin{aligned} x_{larmor} &= x\cos(\mu) + y\sin(\mu), \\ P_{x_{larmor}} &= P_x\cos(\mu) + P_y\sin(\mu), \\ y_{larmor} &= y\cos(\mu) - x\sin(\mu), \\ \textit{and} & \\ P_{y_{larmor}} &= P_y\cos(\mu) - P_x\sin(\mu). \end{aligned} \tag{2.11}$$

It should be noted that the coordinate transformation shown above decouples only the phase space mixing caused by motion along or close to the magnetic field axis. If the phase spaces are initially coupled, the area of any one space may decrease or increase despite the conservation of the hypervolume [35]. Additionally we should say that this transformation holds only for the beam's traversal of the yoke. Passage through the spiral inflector will further mix the two spaces, and the non-linear nature of the mixing renders the use of a rotating frame analogous to the Larmor frame useless [27]. Thus we can expect a further emittance growth due to passage through the spiral inflector.

To determine the effects of motion up the cyclotron axis, rays were started 3 m below the cyclotron midplane and tracked up to the entrance of the inflector at $z = -32.0$ mm. Initially we consider a set of rays in the x, P_x phase space plane. It is clear from the azimuthal symmetry of the fields between the injection point ($z = -3.0$ m) and the inflector entrance that the behaviors of the x, P_x and y, P_y spaces must also be symmetric in this range. As stated above, the two spaces are coupled. Thus, an initial x, p_x space will evolve a y, p_y space as it progresses along the axis. The symmetry of the coupling, however ensures that the behaviors of the initially uncoupled spaces will still be identical regardless of which we choose. Then, restricting ourselves initially to a set of rays in x, p_x, the arrangement of these rays

is set so as to encircle a phase space area (emittance ϵ_0) equal to 100π mm-mrad, where we have changed from the standard cyclotron units of momenta (mm) used in the above equations of motion, to mrad by $p_{mrad} = p_{mm}/\rho$, where $\rho = \frac{p}{qB_0}$ is the radius of curvature in the reference field. Each of the initial points was given a value of $y = p_y = 0$ and tracked up the axis of the K500, passed through a solenoid field centered at 2.227 m below the median plane and through the K500 magnet yoke field. The mechanical design of the K500 yoke can be seen in figure 2.3. The initial axial hole aperture is 15.9 cm in diameter from $z = -1.1$ m to $z = -0.32$ m where the center plug is located. The aperture then narrows to 5.1 cm in diameter until $z = -8.3$ cm below the median plane. The effect of the yoke on the magnetic field is seen in figure 2.4, which shows the on-axis fields produced by the K500 magnet and axial solenoid. The solenoid field was initially chosen to minimize the radial oscillations of the beam envelope at the end of the axial path. This envelope can be seen for both a tuned and untuned solenoid in figure 2.4.

The results of passage through the solenoid and yoke fields can be seen in figure 2.5. The MYAXIAL code was run in linear mode to initially eliminate higher order effects resulting from the nonlinear terms in the field expansion. The figure shows the x, P_x and y, P_y phase spaces (note the use of canonical coordinates) at the entrance of the inflector. We see that, as expected, the coupling between the x and y spaces has evolved a non zero area in y, P_y. By using the transformation to the Larmor frame (as discussed above), we can eliminate the y, P_y phase space area and regain the emittance in x, P_x.

In standard practice, the above initially uncoupled phase spaces are used to examine injection behavior (see [25] through [29]). However the initial phase spaces provided by the ECR and injection line in the case of the K500 may indeed be coupled [19]. Therefore we next turn to the behavior of a set of initially coupled x, P_x

and y, P_y phase spaces. If we again fill the x, P_x phase space at $z = -3.0$ m with ten rays encircling a 100π mm-mrad space and then fill a corresponding space in y, P_y we have effected two uncoupled spaces. If we then couple the particles such that each point in x, P_x corresponds to a set of ten rays in y, P_y we have a set of fully coupled starting conditions. If we then run this set along the axis we find a resulting space like that shown in figure 2.6. Here we are again using the canonical coordinates at $z = -32$ mm. What we find by examining the resultant space is that each initial point in x, P_x has expanded into a ring of orbits surrounding a central point. This is a rather graphic depiction of the emittance growth caused by the magnetic coupling between transverse spaces. An examination of the starting conditions of the central points of each circle shows them to be rays which started with an initial y,P_y value of zero. Recalling figure 2.5, we see that they coincide with the ellipse shown there. The circles surrounding these are thus shown to be the expansion of phase space induced by coupling into x, P_x by the now non zero initial $y = P_y$ space. We can now take the final positions of the two coupled spaces and again perform a transformation into the Larmor frame. Figure 2.6 (bottom) shows the result of this transformation. Using the appropriate value of μ, we see that by uncoupling the two spaces the smaller circles in figure 2.6 collapse into lines. These lines, and the apparent emittance growth they cause, are associated with the initial coupling of the spaces.

Before leaving the axial transport of the beam, we need to consider one final aspect. Included in MYAXIAL is the ability to add a buncher in the beam path prior to its entrance to the K500 yoke. The details of the temporal effects of the buncher and a more expanded explanation of its effects on the beam will be given later, but for now it is worth mentioning its effect on the beam emittance.

The buncher itself is designed to provide a sinusoidal voltage with a RF frequency which is a first harmonic of the cyclotron RF with an option of adding an additional

second harmonic as well [18]. The device sits 1.6 m below the median plane centered on the beam axis. To approximate the effect of the buncher on the beam we calculate the energy increase which the voltage imparts to each ion. In the small-gap approximation we can write the energy gained by crossing the buncher gap (δE) as

$$\delta E = q \int \mathbf{E}_z dz = \frac{qV}{g} \int_{-\frac{g}{2}}^{+\frac{g}{2}} \sin(\omega t_0 + \frac{\omega z}{v_0}) dz, \tag{2.12}$$

where V is the peak voltage across a gap of width g, and v_0, t_0 are the velocity and time at the center of the gap, and ω is the angular frequency of the RF voltage. Integrating this we obtain

$$\delta E = qV \sin(\omega t_0) T,$$

where T is a transit time factor given by,

$$T = \frac{2v_0}{\omega g} \sin(\frac{\omega g}{2v_0}).$$

The above value for δE is true only for a gap with a first harmonic voltage. For a buncher providing both first and second harmonics this becomes

$$\delta E = qV\Big(\frac{2v_0}{g\omega}[\sin(\frac{\omega g}{2v_0}) \sin(\omega t_0) - V_{1,2}\frac{1}{2} \sin(\frac{\omega g}{v_0}) \sin(2\omega t_0)]\Big), \tag{2.13}$$

where $V_{1,2}$ is the relative amplitude of the in-phase first and second harmonic voltages. To get from the energy impulse given above to a δp_z we note that

$$\delta E = v_0 F_z \delta t = v_0 \delta p_z, \quad or \quad \delta p_z = \frac{\delta E}{v_0}, \tag{2.14}$$

where δE is given by equation 2.13. This effect is then included in MYAXIAL.

To determine the effect of the buncher on the phase space, the set of initially uncoupled conditions was re-run using both first and second harmonic buncher voltages. Ellipses were started over a $\tau_0 = \omega t_{initial}$ range of 250° in steps of 25. The results (at the inflector entrance) of this run can be seen in figure 2.7. Even after changing

to the appropriate Larmor frame there is still an emittance growth as evidenced by the 'spikes' emanating from each phase-centered ray. The source of this growth can be seen by recalling the purpose and effect of the buncher on the time range of the beam. Liouville's theorem combined with a transformation to a Larmor frame assure no growth or mixing of the initially transverse phase spaces, however, the total phase space hypervolume becomes six dimensional when the time-energy space is included. In the case of no buncher, the beam is mono-energetic and this reduces the(E, τ) phase space area to zero resulting in the 4d space considered above. When the buncher is turned on however, it imparts a finite area in the E-τ coordinates. Additionally the energy time correlation is chosen such that the time spread is drastically reduced (a factor of seven) at the entrance of the inflector. Even though the energy remains constant once the buncher has been passed, the buncher does produce an additional coupling in the new 6d space.

Inflector Traversal

A second complementary orbit code is used to track rays through the spiral inflector. For the code INFLECTOR, the equations of motion and field approximations needed are much simpler in form than those given above for traversal of the axial field. Over the vertical and radial range of the inflector (3 cm and 1.5 cm respectively) there is little variation in the magnetic field. Thus the above expansions are discarded in favor of a constant field approximation ($B_z = B_0$ and $B_x = B_y = 0$). Then the equations of motion become

$$\begin{aligned} p_x'(z) &= [\frac{\gamma}{\omega_0 B_0 p_z} E_x + \frac{p_y}{p_z}] \\ p_y'(z) &= [\frac{\gamma}{\omega_0 B_0 p_z} E_y - \frac{p_x}{p_z}] \\ p_z'(z) &= [\frac{\gamma}{\omega_0 B_0 p_z} E_z]. \end{aligned} \tag{2.15}$$

The electric fields produced by the inflector electrodes, and thus required by INFLECTOR, were calculated from an electric potential produced using RELAX3D[36] with an initial grid size of 81 × 121 × 101 (x,y step= 0.051 cm, z step= 0.038 cm). The form of the electrodes was created by starting with a volume of grid points, the outer surface of which matched the outer shape of the entire inflector (as seen from the top, ie. $z = 0$). The location of the reference ray described by equations 2.3 in this volume was calculated at a series of points along its path. At each point, the location of a 0.6 cm diameter cylinder with its axis perpendicular to the reference ray was calculated. All grid points found to be inside this cylinder were removed from the volume. In this manner material was removed from the grid, thus simulating the cutting tool which would be used to create the actual electrodes. The result of this procedure was two separated volumes each of which was assigned a fixed voltage value. The potentials in the new space between these volumes was calculated by RELAX3D. The shape of the volumes (electrodes) thus obtained can be seen in figure 2.8.

After the particles are tracked through the magnet yoke and up to the inflector by MYAXIAL, they are tracked through a thin circular aperture at the entrance to the inflector (centered on the magnet axis and with a diameter equal to the electrode spacing), the inflector electrodes and finally a thin exit aperture centered on the reference ray in the median plane of the cyclotron. The inflector voltage and position were set by requiring the central (axial) ray to emerge with $p_z = z = 0$.

To examine the effects on the beam of passage through the inflector, initial x, p_x and y, p_y phase spaces (unmixed) were started at the entrance of the inflector. Rather than using a single ring of starting conditions as mentioned above, a set of five equally spaced concentric rings enclosing areas between 100π and 4π mm-mrad were started in each of the spaces. Figure 2.9 shows the resultant spaces at the inflector

exit. Both spaces show the phase space mixing caused by both the magnetic field and the field due to the electrodes. The initially x, p_x space is much more distorted than that which starts in y, p_y. This is not surprising considering the fact that the inflector gap is in the x direction at its entrance. Thus the x, p_x space sees a rather non linear electric field as evidenced by the distortions in both its final x and y spaces. The initially pure y, p_y space occupies a physical width of 3 mm at the entrance of the inflector, parallel to the electrode surfaces, in the good-field-region described above. The initially pure y, p_y plots also show the mixing of the phase spaces. The space develops an elongated space in secondary (orthogonal) space at the inflector exit. The space is much less distorted than the corresponding secondary space from the initially pure x, p_x. It is also interesting to note that while the initially pure x, p_x starts its inflector passage distributed across the electrode gap, it exits the inflector with the majority of its emittance in a plane parallel to the electrode surfaces. The initially pure y, p_y space shows a similar behavior. This corresponds to the rotation of the body-centered axes as described by Root [25].

Considering the phase space distortions caused by the spiral inflector, other inflector designs were considered. Most notably the hyperboloid inflector, which provides a more linear transfer of the beam, and the electrostatic mirror were studied.

The Electrostatic Mirror and Hyperboloid Inflector

For simplicity in design, the electrostatic mirror clearly is superior to the spiral inflector. The mirror consists of a grounded mesh parallel to a high voltage electrode. This pair of plates is placed at a 45° angle. The beam then passes through the mesh and encounters a high electric field with components in the vertical and horizontal direction. The axial speed of the beam is slowed while the horizontal speed is increased. Eventually the beam is bent from its vertical path into the median plane passing once

again through the grounded mesh. There are several problems with the electrostatic deflector, which make it a less viable option, associated mainly with beam loss. The beam must make two passes through the grounding mesh, with resultant beam losses each time. Additionally, as the beam enters the deflector it encounters an increasing electric potential as it is in the process of inflection. This corresponds to a large decrease in velocity with all its inherent spacecharge problems. Thus the electrostatic deflector is much less attractive than the spiral inflector. The hyperboloid inflector, on the other hand, is easier to machine and has much more linear beam transport properties than the spiral inflector.

The hyperboloid inflector suggests itself as a solution to ion injection in that it is easy to machine (electrode shapes are surfaces of rotation), and the additional rotational symmetry provided may improve the beam optics. The equations of motion for particles through a hyperboloid inflector, as described by Muller[20], yield the following relations for the path of the reference particle,

$$x_c = \frac{1}{2} r_0(-b\cos(akt) + a\cos(bkt)),$$

$$y_c = \frac{1}{2} r_0(-b\sin(akt) + a\sin(bkt)),$$

and

$$z_c = \frac{1}{2} r_0 \sin(kt),$$

where a and b are geometrical constants and r_0 is the radius of the center of the inflector gap. These equations are much more straightforward than those for the spiral inflector (equations 2.3). The major drawback of this type of inflector is that it provides (in the high field axial injection case) no mechanism with which to move the orbit center for the emerging ion. As with all inflector designs, injection through the cyclotron's yoke requires an on-axis central ray. This, along with the chosen ion injection energy (required by space charge considerations) and the magnetic field, fully

determine the center of curvature for the emerging ions. When the K500 parameters are used, it is found that the center of curvature for the reference orbit is greatly displaced. Figure 2.10 shows the x,y projections of the orbits for the reference ions for the two inflectors and their final orbit centers. The spiral inflector allows us to choose this center regardless of the ion magnetic radius. Thus its placement was chosen such that when it is coupled with the effect of passage through the first electric gap in the cyclotron, the orbit center is near the machine center. This is not possible with the hyperboloid inflector. Once the ρ (radius of curvature) is chosen, the final radius is set. This, coupled with the larger size of the hyperboloid inflector, makes it of little use in this design.

2.1.2 System Acceptance

With the spiral inflector clearly chosen as the bending device, initially uncoupled x, p_x and y, p_y phase spaces were started to determine the acceptance of the axial injection system. Two sets of acceptance calculations were done. The first concerned the acceptance of the inflector entrance hole. The acceptance was determined by running a square grid of initial (uncoupled) conditions through the system and eliminating any rays which did not pass through the entrance aperture. By varying the strength of the solenoid field the shape of this accepted region could be changed. Figure 2.11 shows the shape of the accepted region and its variation with solenoid field. The change in the spiral shape of the regions is best understood by considering the paths the orbits take while traveling through the axial field. Ions starting 3 m below the median plane are trapped about a particular flux line determined by their initial position and transverse velocity. As the orbits are tracked up toward the median plane, these ions orbit around their particular flux line producing a helix-like path. On top of this is superimposed an azimuthal drift associated with the curve of the

flux lines [37]. The center of the helix then precesses about the axis, moving from flux line to flux line. As the ions make their way toward the inflector entrance, the axial field increases. Since the magnetic moment of the current loop of the particle orbit is a constant, the orbital radius shrinks as the field increases [37]. When the aperture is reached, the acceptance is determined by three factors: the position of the pinning flux line, the radius of orbit about that flux line, and the phase of that orbit. For an orbit to pass through, one of the following conditions must be met:

- Either the pinning flux line must pass through the accepting aperture while the orbital radius about that flux line is smaller than the smallest radial distance from the line to the aperture edge,

or

- the flux line passes through the aperture, but the orbit radius is greater than the smallest radial distance to the aperture edge. The ion will then be accepted only if the phase of the orbit places it in the aperture,

or

- the flux line does not pass through the aperture and the orbit radius is larger than the distance from the pinning flux line to the aperture. If this is the case then the phase of the ion must be such as to place it in the aperture.

By changing the solenoid field the phase of the ions arriving at the aperture is changed. This phase then (as described above) determines which rays (and thereby starting conditions) will enter the inflector. Thus, the accepted starting conditions at $z = -3$ m are changed. Additionally, the change in accepted starting conditions results

Table 2.1: Normalized Acceptances

Inflector Gap	$\beta\gamma$	x, p_x emittance (mm-mrad)	y, p_y emittance (mm-mrad)
6 mm	.0035	5.77	7.80
4 mm	.0030	5.42	3.66

in a corresponding change in final x,p_x and y,p_y phase spaces. These changes can be seen in figures 2.12 and 2.13.

The acceptance of the entire transport plus inflector system was calculated by a radial search of the starting conditions. For a given radial line in phase space a search was conducted for the most extreme starting conditions resulting in a path which passed through the inflector system. By scanning the angle of these radial lines an outline of the accepted region was obtained. Figure 2.14 shows the x, p_x and y, p_y phase-space acceptance for the inflector. Figure 2.14 also shows the same phase space acceptances for the smaller 4 mm aperture inflector now in use [17]. The normalized emittances for each of these areas can be seen in Table 2.1.2. Clearly the new 6 mm aperture inflector will have a greater acceptance, as expected. It appears that the x, p_x phase spaces are nearly the same for both designs. However this is misleading since the size of the x, p_x and y, p_y phase spaces relative to one another can be adjusted by changing the solenoid setting. Finally, we note that the new inflector acceptance (figure 2.14) is much more compact than that of the old 4 mm design.

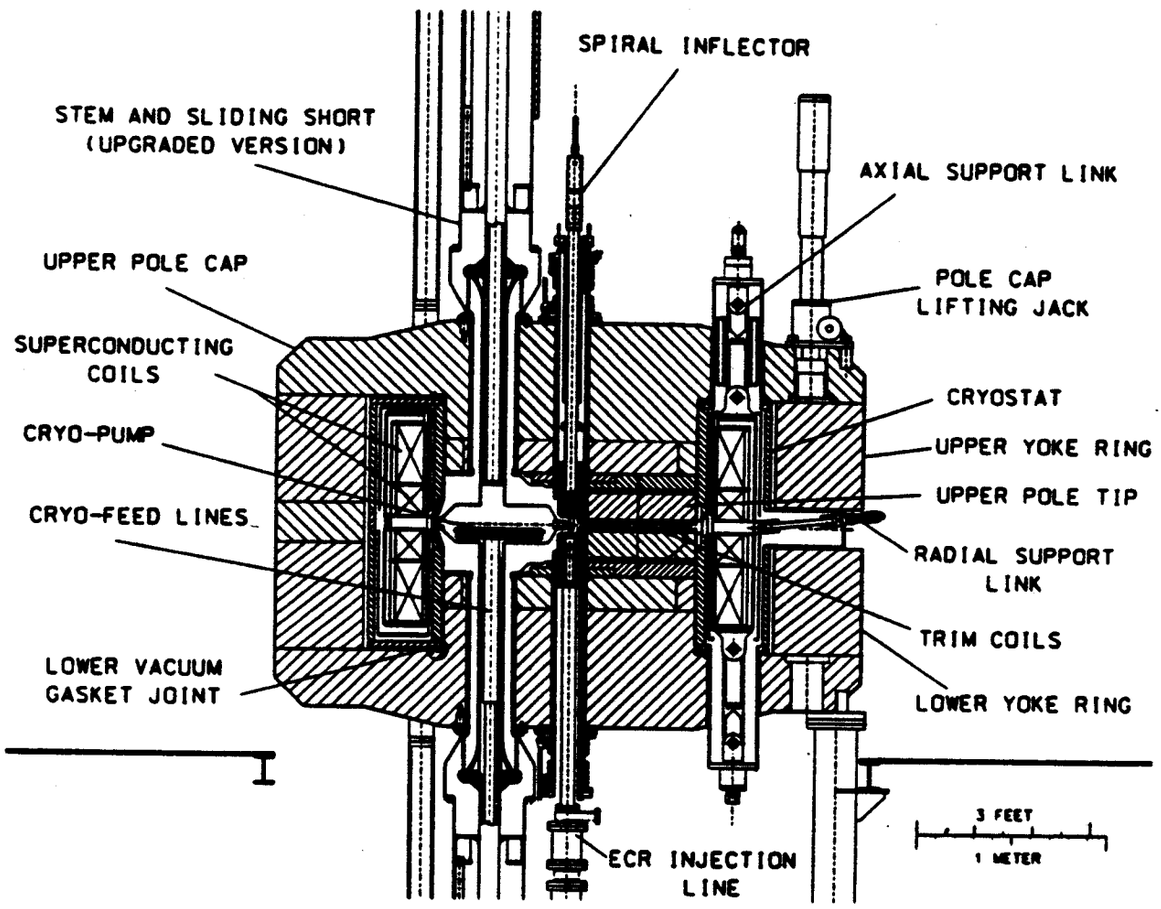

Figure 2.3: A cross section of the K500 axial hole design. The initially 15.9 cm diameter hole is reduced to 5.1 cm as the beam nears the median plane.

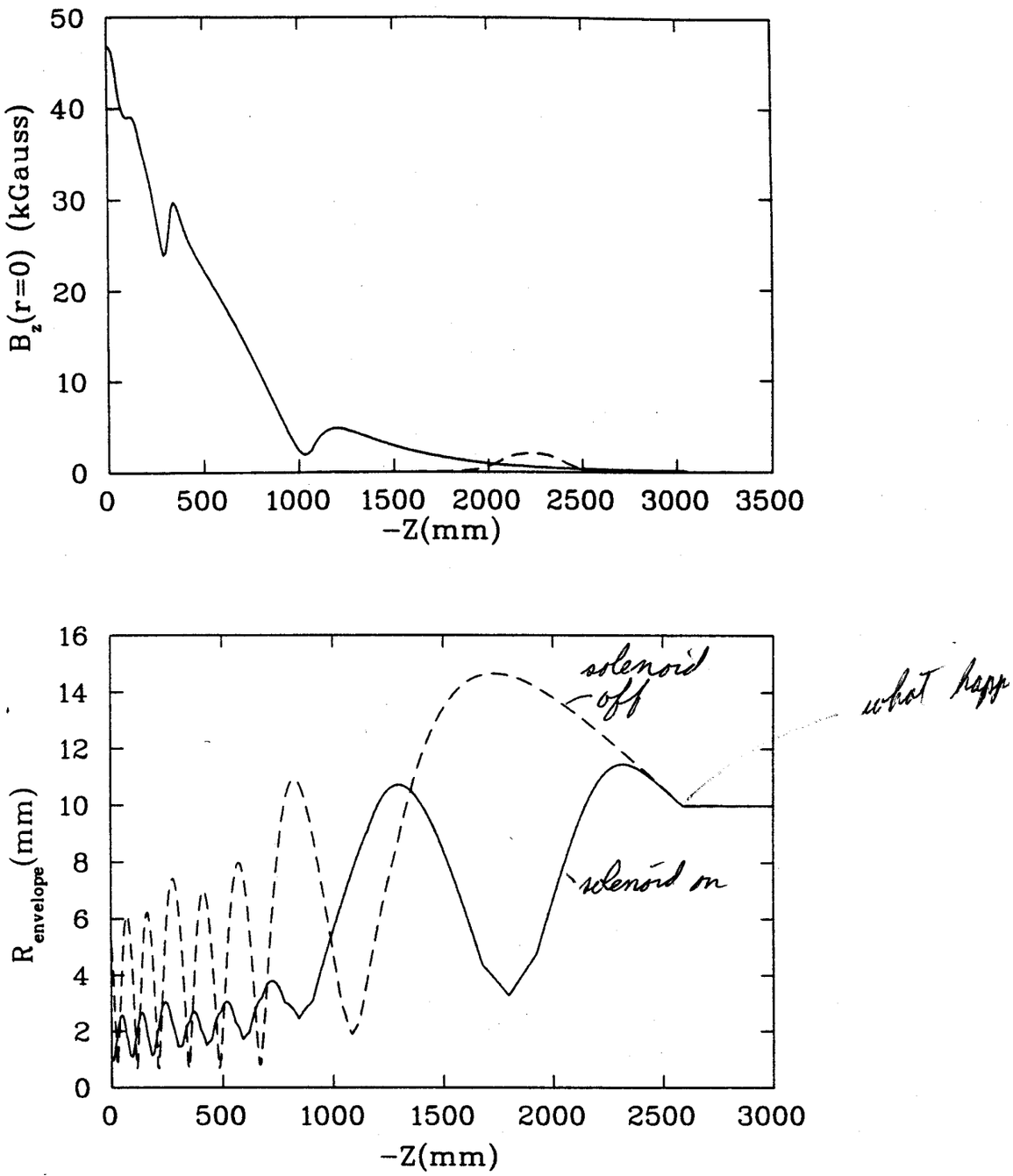

Figure 2.4: Top: The axial magnetic field profile in the K500 calculated using POISSON. Shown are both the main field (solid) and the field produced by the vertical beam line solenoid (dashed). Bottom: The radial beam envelope along the vertical beam line and through the K500 yoke. Envelopes are shown for cases with (solid) and without (dashed) the use of the on-axis solenoid.

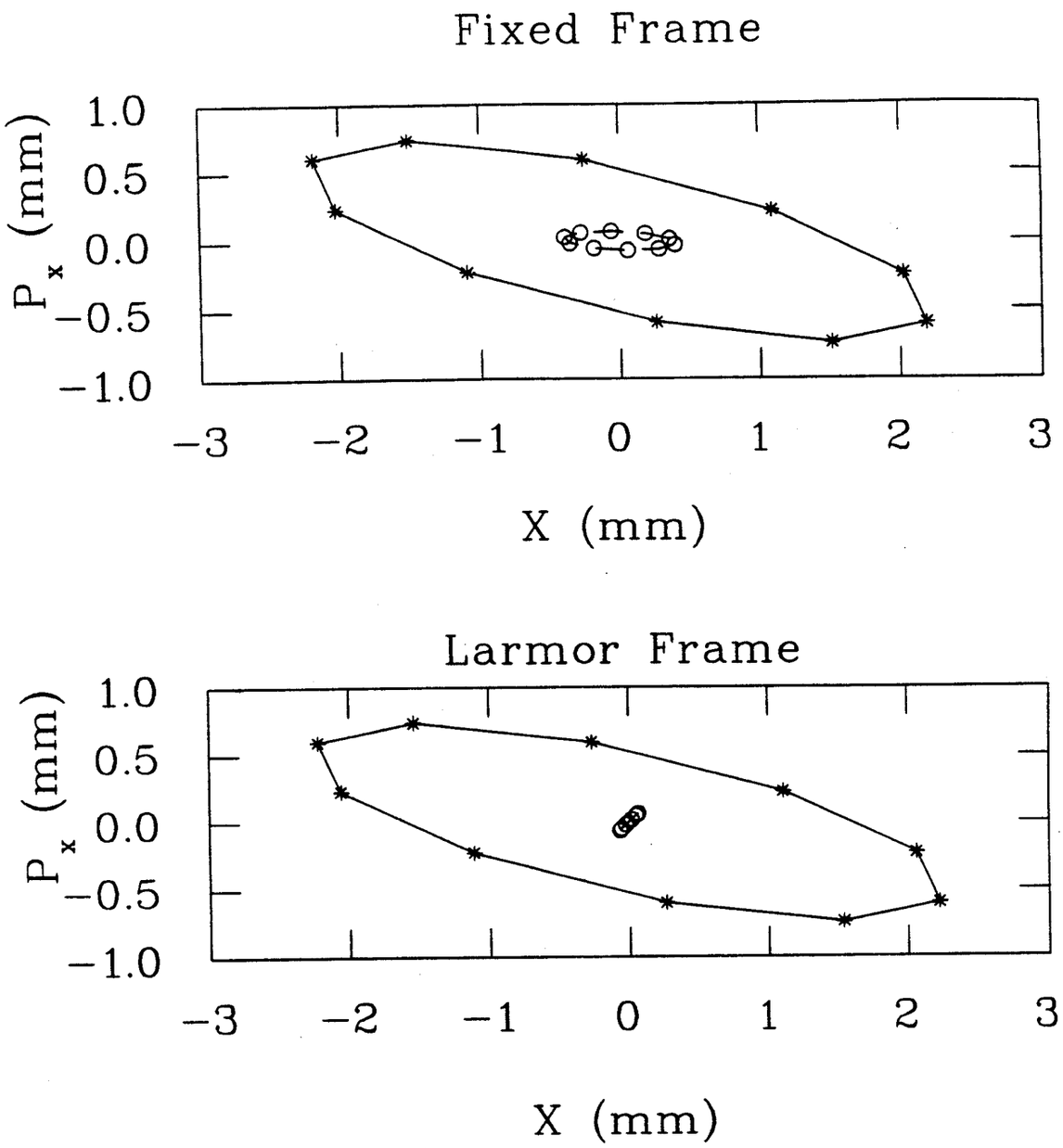

Figure 2.5: The initially uncoupled phase space at the entrance of the inflector both before (top) and after (bottom) transfer to the rotating Larmor frame. The asterisks denote the x, p_x space and the circles the y, p_y. Note that the small phase space that has opened in the y space due to the coupling caused by the magnetic field is removed upon transformation to the larmor frame.

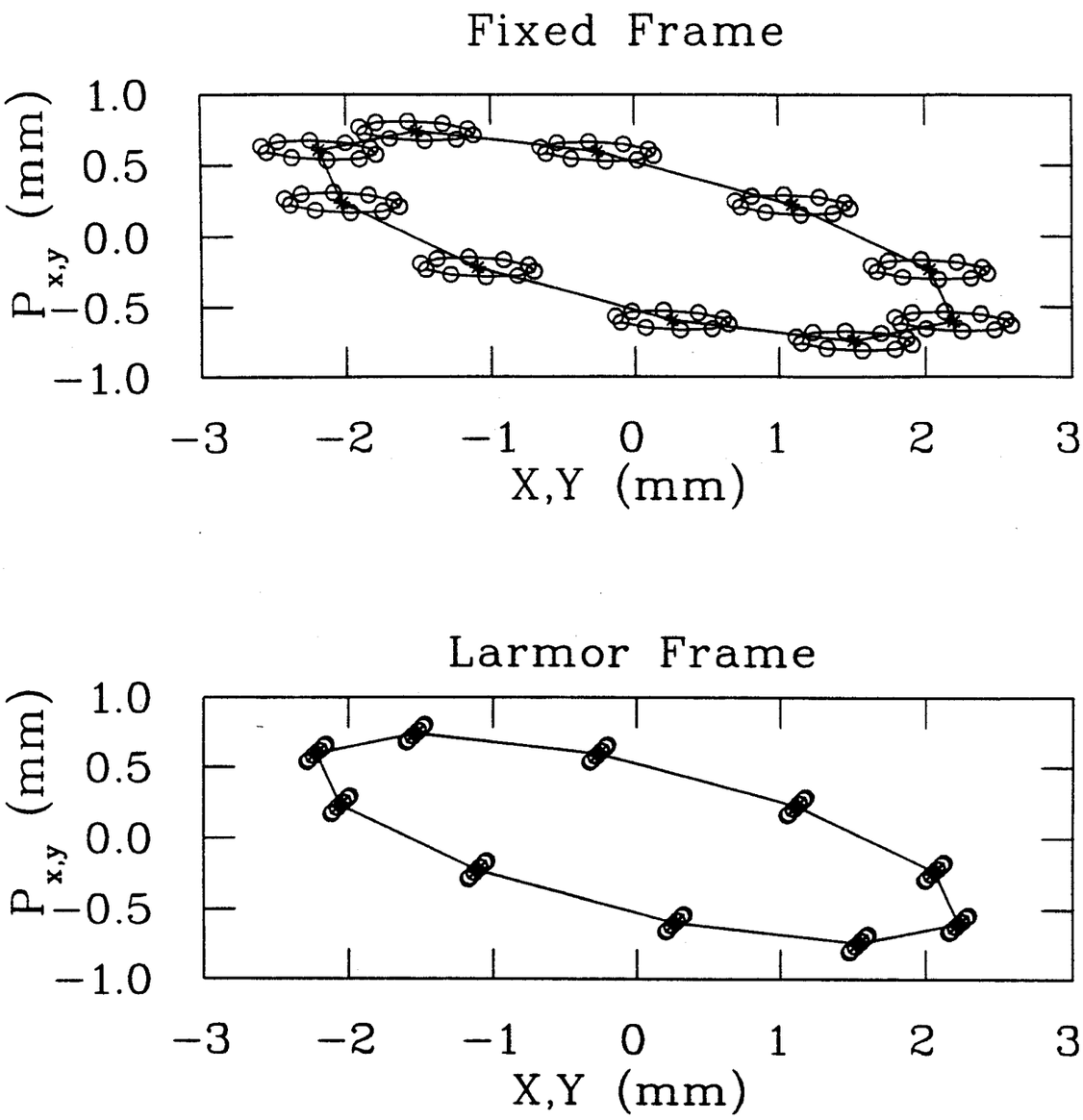

Figure 2.6: The initially coupled phase space at the entrance of the inflector both before (top) and after (bottom) transfer to the rotating Larmor frame. Note that small 'additional' phase spaces have opened around each point in the space. This is the effect of the coupling caused by the magnetic field. The area enclosed in each of these subsidiary spaces is not removed upon transformation to the larmor frame but they reduce to small lines causing a growth in the total area. These are an effect of the initial coupling of the spaces.

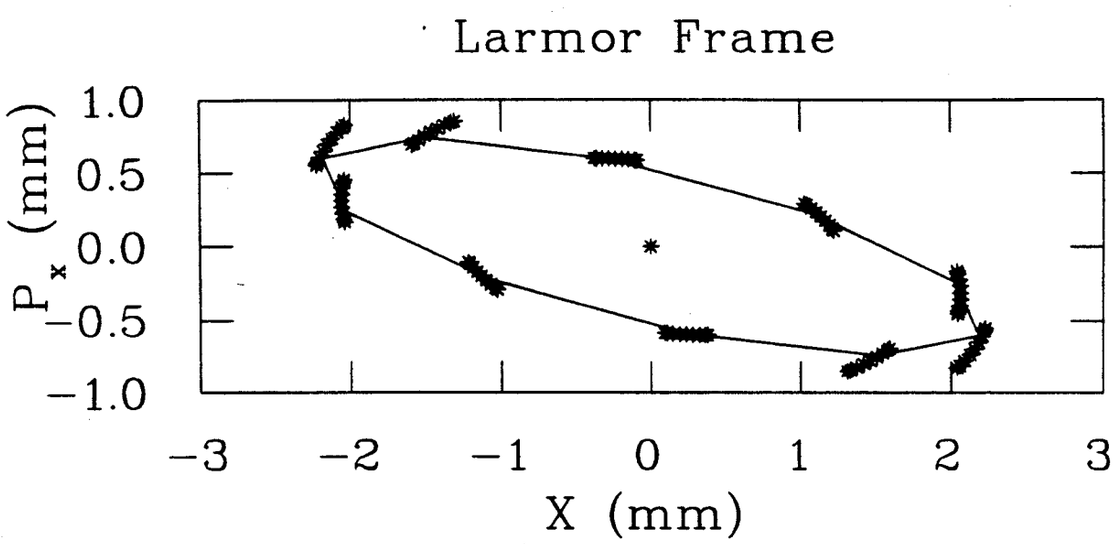

Figure 2.7: The phase space at the entrance of the inflector for an initially 100π mm-mrad beam with the first and second harmonic bunchers on. Even after transform to the Larmor frame there is significant increase in the emittance.

Figure 2.8: The spiral inflector electrodes. This picture was created as input to a RELAX3D run with grid dimensions 81x121x101, $\Delta x = \Delta y = .0254$ cm and $\Delta z = .127$ cm. The darker of the two structures is the inflector anode while the lighter, smaller piece is the low-voltage cathode.

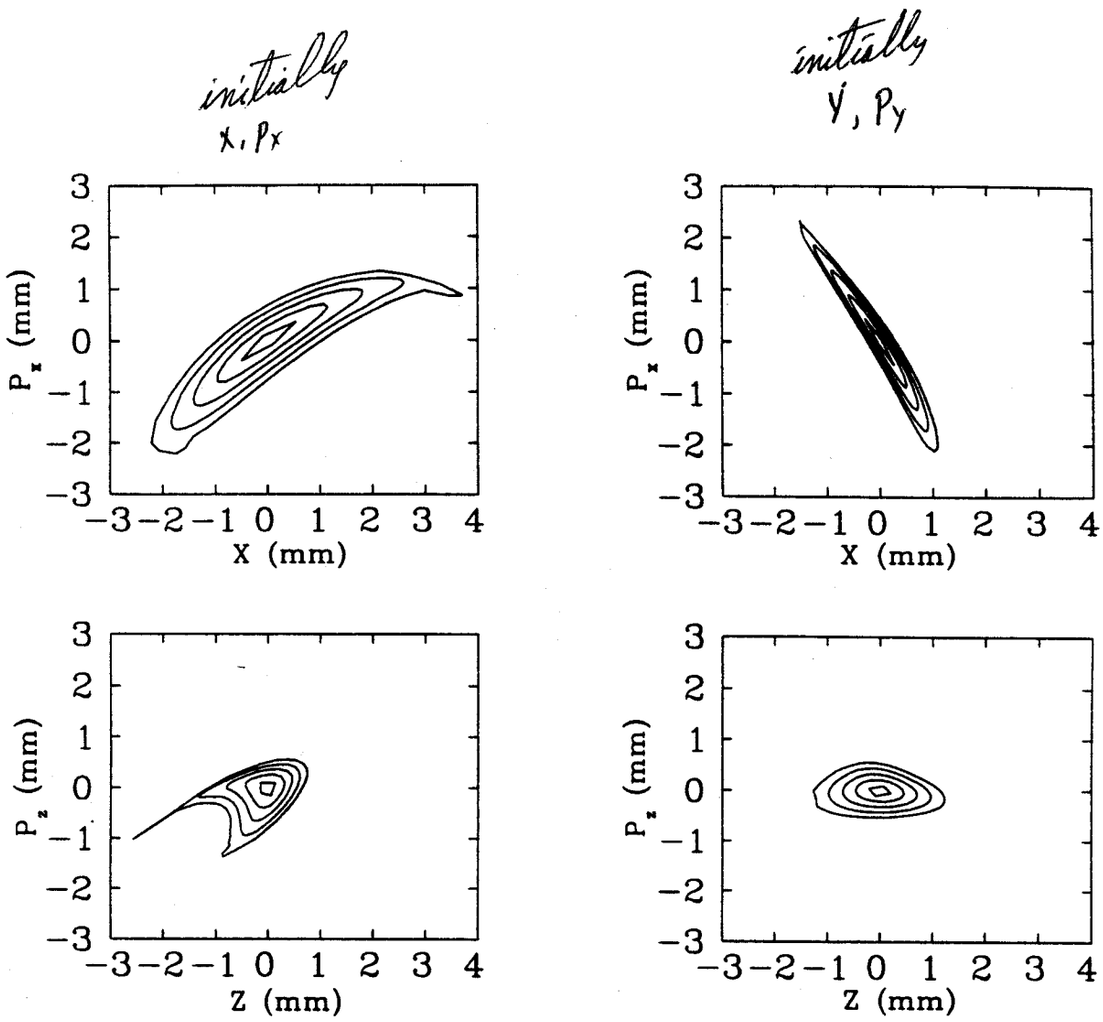

Figure 2.9: The final phase spaces showing the effect of transport through the inflector. The figures on the left show the final x,z phase spaces for a 100π mm-mrad phase space initially in the x,p_x plane while those on the right show the same for a space started in y,p_y.

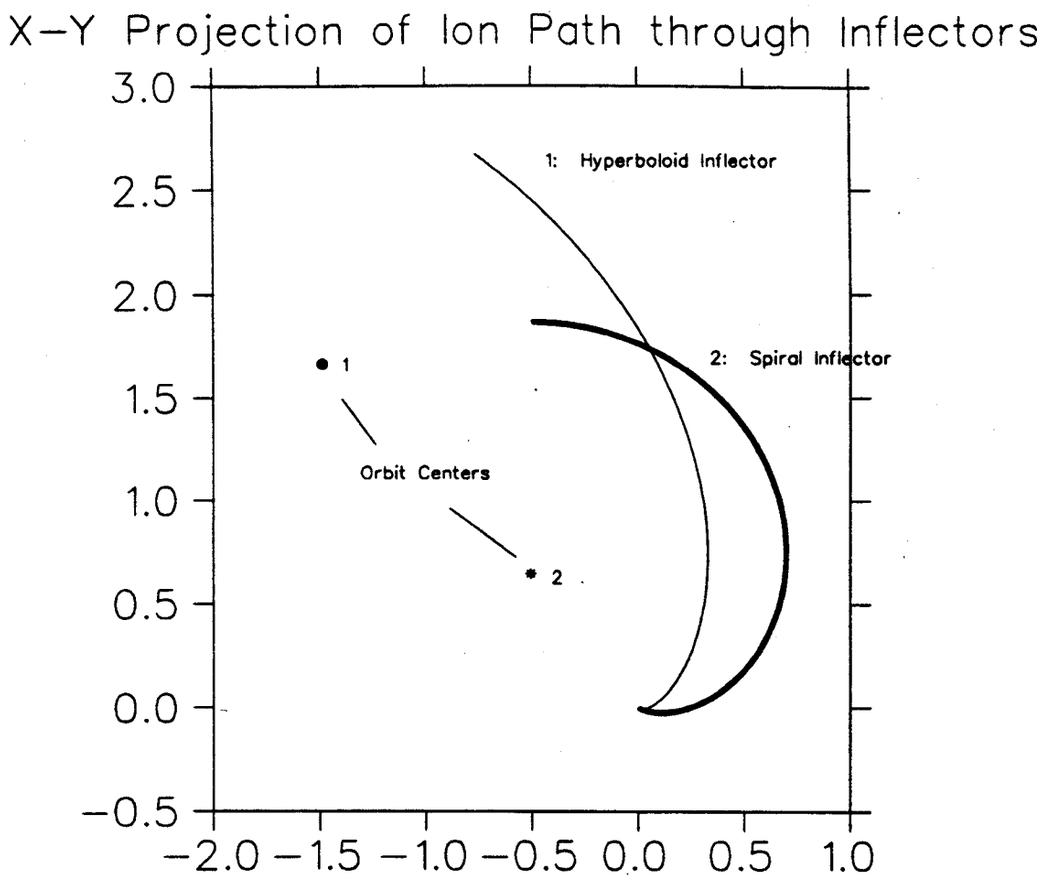

Figure 2.10: x,y projections of the reference orbits for the hyperboloid and spiral inflectors. Also marked are the final centers of curvature. The hyperboloid inflector leaves ions with a much larger, destructive, centering error that cannot be easily corrected.

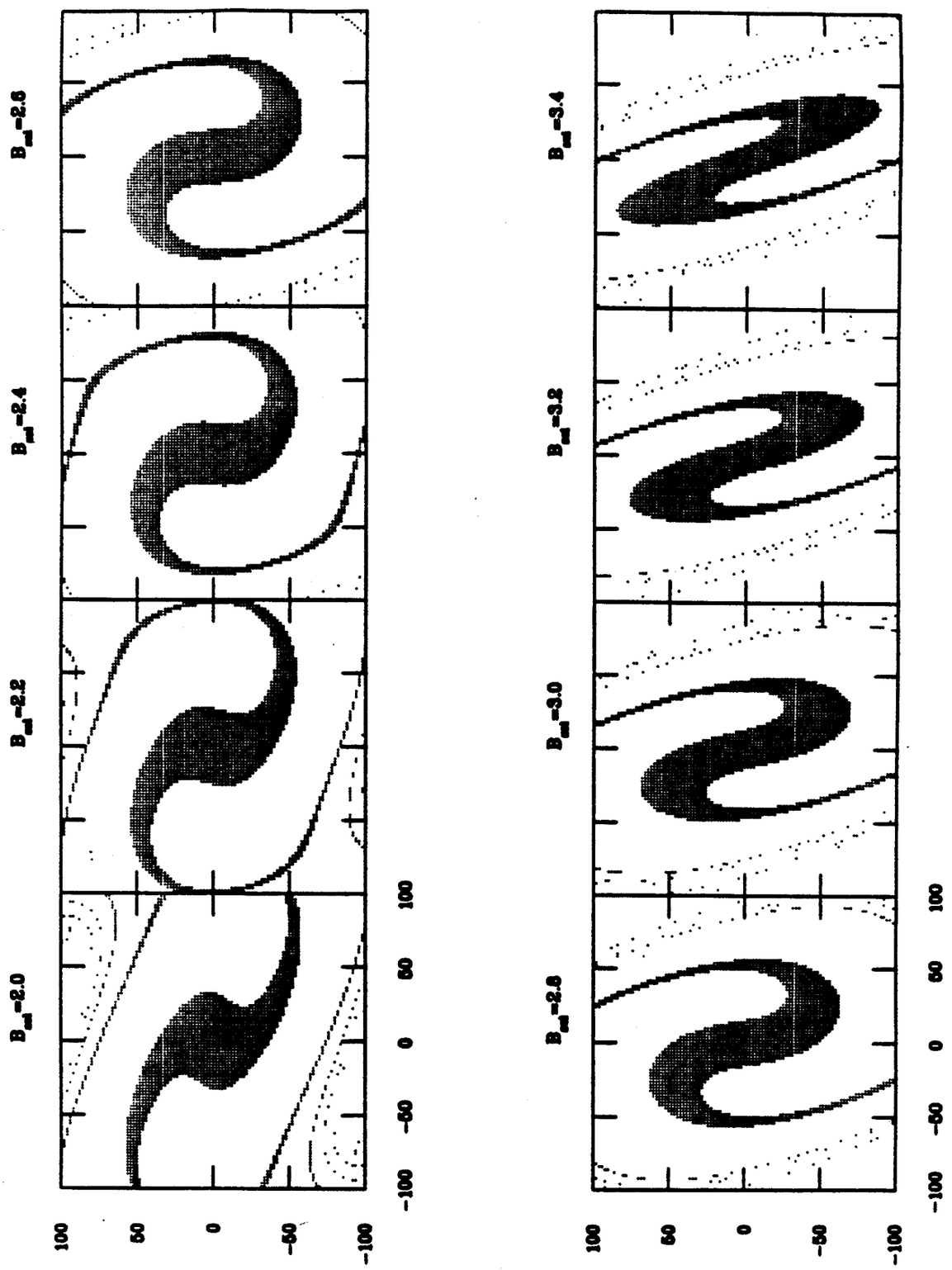

Figure 2.11: Starting conditions (x, p_x) at 3 m below the median plane which result in ion trajectories which pass through the inflector entrance aperture. As the solenoid field is varied the accepted starting conditions change.

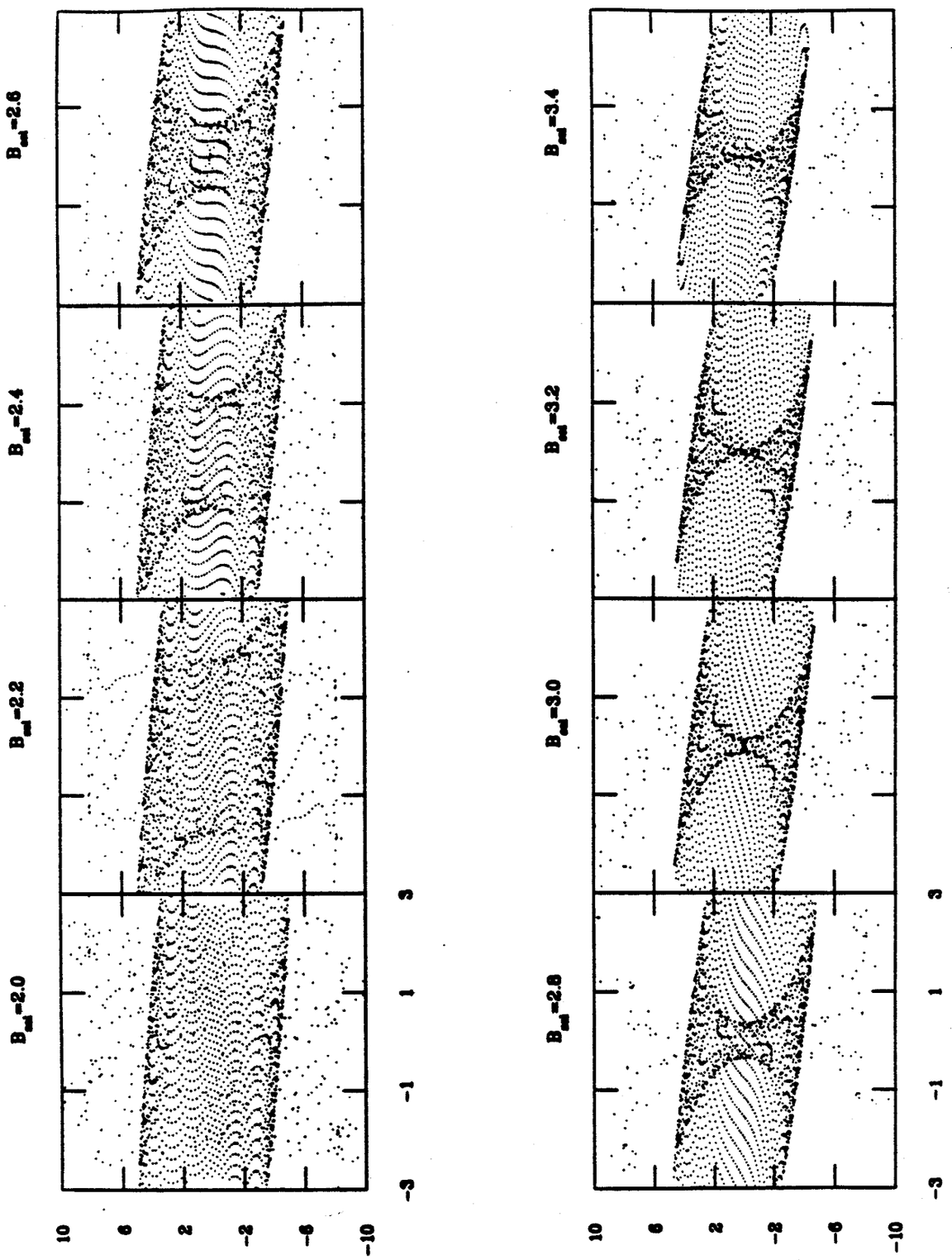

Figure 2.12: x, p_x phase space at the entrance of the inflector for an initially evenly populated x, p_x space at $z = -3$ m for various solenoid settings.

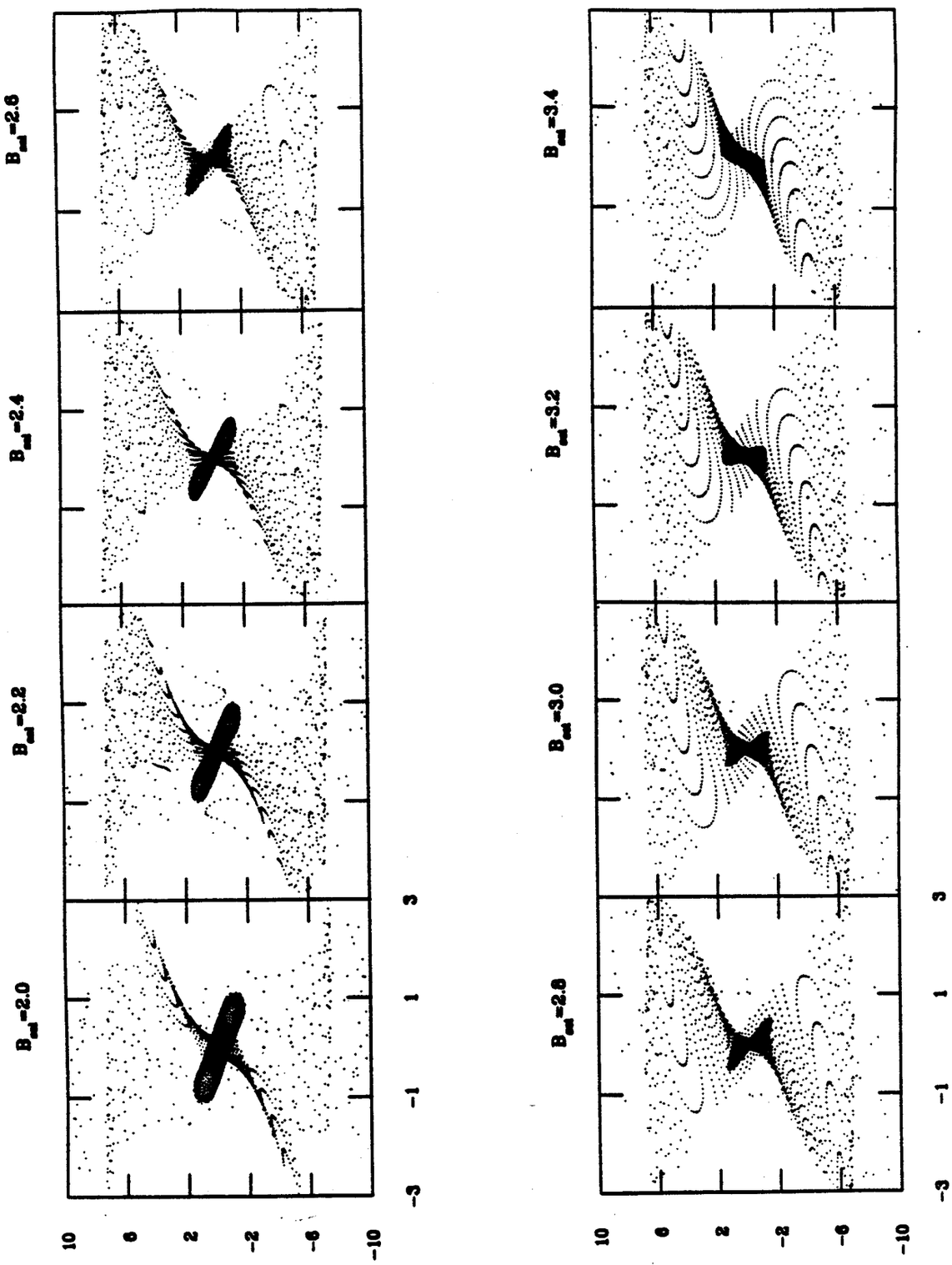

Figure 2.13: y, p_y phase space at the entrance of the inflector for an initially evenly populated x, p_x space at $z = -3$ m for various solenoid settings.

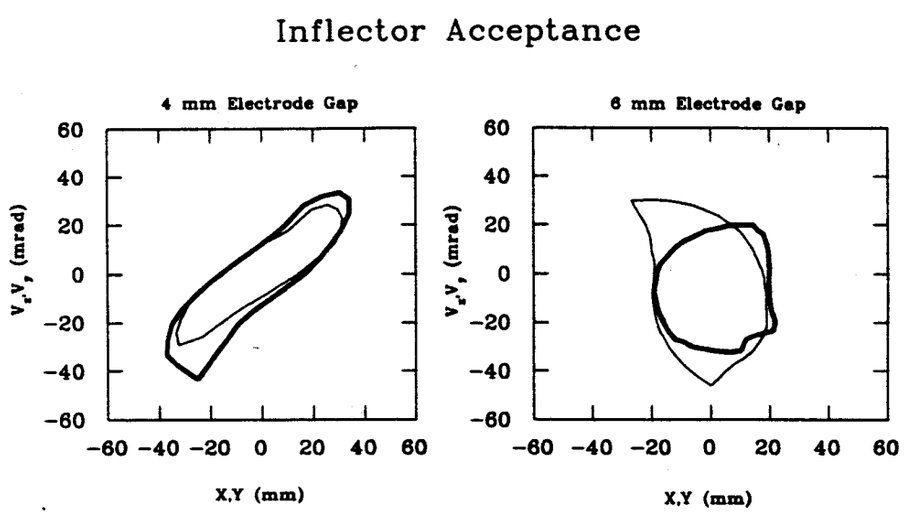

Figure 2.14: Unnormalized acceptance (at $z = -3.0$ m) for both the present 4 mm gap spiral inflector (left) and the planned 6 mm gap (right). Double-thickness lines represent the x, p_x space while the single line represents the y, p_y. In each case the solenoid was set to minimize the radial oscillations of the beam near the inflector entrance.

Chapter 3

Central Region Design

The accelerating structures in the K500 consist of three 53° dees occupying the valley regions of the magnet gap. These dees extend radially from 5.1 cm out to the extraction radius. The space left at the center of the machine (r = 0 to 5 cm) is used for the central region. The central region itself (figure 3.1) consists of a set of specially shaped electrodes attached to the dees which accelerate the particles from the ion source (or injection mechanism for an external source) out to the main, electrode-free dee structures. The central region electrodes consist of posts mounted on the center plug and electrodes mounted on the tips of the dees (and thus called dee tips). The placement and shape of the various posts and electrodes define a range of starting conditions for the ions which can be accelerated out of the region. Further, the electrodes are positioned so as to place the beam as close to its accelerated equilibrium orbit, upon exiting the central region, as possible. These electrodes then limit the amount of beam which the machine can accelerate and dictate the quality of the beam.

Once an inflector shape was determined, a second harmonic ($\omega_{rf} = 2\omega_{orb}$) central region was designed. All electrode shapes and positions had to accommodate the new, larger inflector housing and guide the beam through the central region leaving it

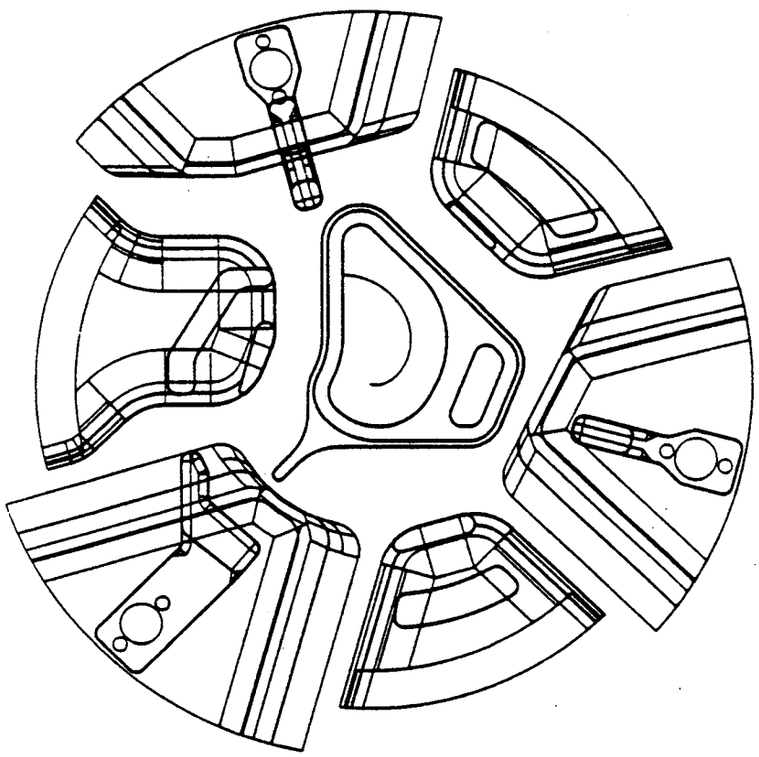

Figure 3.1: The CAD mechanical design drawing for the second harmonic central region. This drawing was used to create the final input for the RELAX3D code.

reasonably well centered. The placement, orientation and shape of the posts, inflector and dee tips need to satisfy four conditions:

- The inflector orientation must provide good vertical focusing for the emerging ions. Since the first few gaps will provide the critical vertical focusing [39], the inflector exit must be placed to assure that the ions will pass through the first few gaps with the proper 'late' phase required for electric focusing.

- Each dee must be isolated, that is, the fields produced by a dee must be restricted to the area immediately surrounding that structure and not allowed to bleed into the fields of neighboring dees. This prohibits cross-talk between the RF amplifiers and prevents the formation of destructive radial fields along the beam path. This can be accomplished by introducing vertical posts on the intervening, grounded, hill tips.

- The size and position of the dee electrodes must provide needed structural support at the dee tips as well as preventing the creation of radial fields in the beam path. By placing posts at the tips of each dee and larger secondary posts at a larger radial distance along the dee, the radial fields are excluded from the ion orbits and the structural strength of the dee is enhanced.

- The beam should be placed upon exiting the central region such that during acceleration through the K500, it is well centered (a beam is well centered if it exhibits no coherent radial oscillations). In this way any small centering errors produced by misplacements in the mechanical construction of the central region should be correctable through the use of the existing K500 first harmonic magnetic field bump. To achieve such beam placement the shape and position of the aforementioned posts are adjusted to misshape the accelerating gaps during the first turn. The distortion of the gap shapes which results can be chosen to correctly place the beam at the end of the first turn.

In order for the central region to be valid for ions with the wide range of charge to mass ratios required, the machine is operated in what is called constant orbit mode [16]. That is, the trajectory of all ions (in a given harmonic mode) will be similar regardless of their $\frac{q}{A}$. This is accomplished (in the case of an internal ion source) by assuring that the Reiser parameter $\chi = \frac{l^2 B^2 \frac{q}{A m_0}}{V_{dee}}$ is constant, where l is the dee to ground distance, B is a reference magnetic field and V_{dee} is the dee voltage. If the radius of the first turn is to be the same for all ions, the dee voltage (V_{dee}) must be set such that $\frac{V_{dee}}{\omega_0 B_0}$ is constant.

Added to all the above conditions, are the constraints that the electric fields be kept as low as possible to limit sparking, and that the transmitted current be as large as possible. According to the scaling rule given above, the 16.6 MeV/u O^{+3} is the

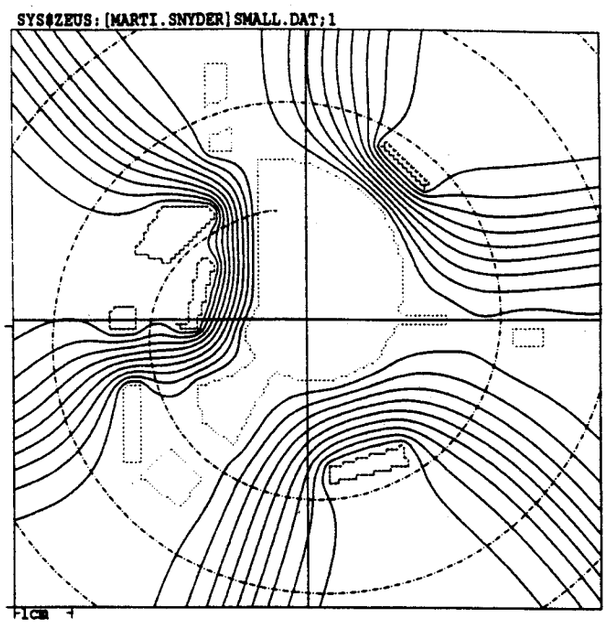

Figure 3.2: The initial central region design. Shown are the median plane electric potentials. Note the potentials shown do not correspond to the $h = 2$ case. Rather they are for a case where all dees are excited with the same applied voltage. Posts are identified by their dotted outlines. The grid dimensions were $201 \times 201 \times 11$, $\Delta x = \Delta y = 0.0762$ cm and $\Delta z = 0.127$ cm. Also shown is the path of the central ray.

particle that will require the highest dee voltage and as such, was chosen as the test particle for design work. Since the dee voltage will be 70 kV for the O^{+3} test case, an electrode separation of 8 mm was chosen, limiting fields to 88 kV/cm. With these considerations in mind a central region was designed that produced a well-centered beam with good vertical focusing properties. Figure 3.2 shows the central region so obtained as well as the path of the central ray. The figure and fields were produced by a RELAX3D run using an initial $201 \times 201 \times 11$ grid ($\Delta x = \Delta y = 0.0762$ cm, $\Delta z = 0.127$ cm).

The large shape in the center of figure 3.2 is the inflector housing. The shape of the housing has been modified by adding extensions which will help to isolate the dees

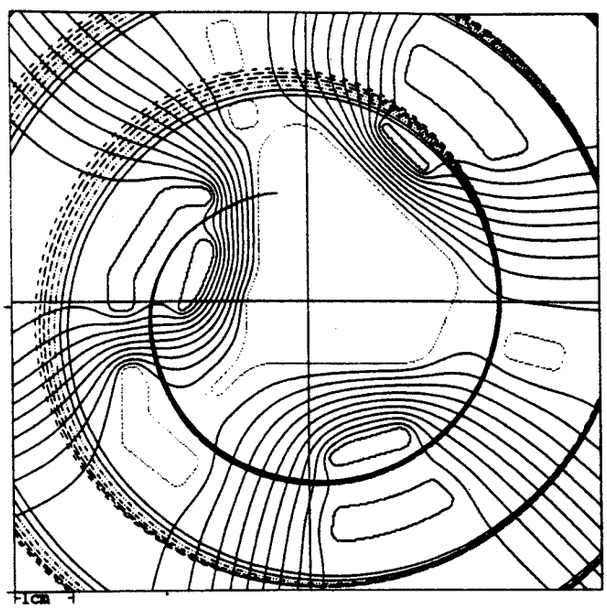

Figure 3.3: The central region design showing central rays with starting times between $\tau = 190°$ and 230° in 5° steps. The radial spread is clearly seen at the $\theta = 110°$ first-turn slit.

(see above). Foreseeing the possible need for a first turn phase selection slit [40, 19], the post located at $\theta = 105°$ was modeled to include such a device. To create a ϕ-dependent radial shift at the first turn window slit, the shapes of the preceding gaps were adjusted. The azimuthal position of the fourth gap is such that the particles pass through the gap when the voltage is rapidly increasing. Thus, rays with different times see significantly different voltages. Figure 3.3 shows the first-turn orbits for central rays with starting times between $\tau = 190°$ and 230° in 5° steps. The radial spread is clearly evident by the time the orbits reach the first turn slit with $\theta = 110°$.

The dee and hill shapes used in this model exist as single planes at the vertical edge of the relaxation field. Additionally, the shapes of the posts and dee tips have not been adjusted by rounding corners or adding a vertical dependence on the dee tips. In short, the design is a simplified model which is to be used as a guide for electrode shape and placement for the production of a more realistic mechanical drawing of the

same region.

A mechanical drawing (including the proper vertical dependence) was produced using the position of the posts and electrode provided by the above design out to 5 cm (see figure 3.1). The design then obtained was transferred back in a digitized format which could be used as input for a RELAX3D run. The shape of the hill liner and the dee structure were then extended out to 30.5 cm.

Previously the size of any RELAX3D grid was limited to 2,000,000 total grid points by considerations of run time and computer memory. Advances in these areas have provided for an increase in these limits. Thus, the mechanical design grid was increased to over 5,000,000 points allowing a much smaller grid spacing to be used. Additionally, to maximize the usable points in any such grid, a grid of the same number of points but over a larger sampling area was first run. The values of the boundary points of the smaller, central region grid were then interpolated from this larger grid. In this way, boundary errors could be reduced and a more realistic field obtained.

The field obtained from this new grid (and the corresponding electrode structure) can be seen in figures 3.4 and 3.5. These figures are from a $401 \times 401 \times 25$ grid ($\Delta x = \Delta y = 0.0254$ cm, $\Delta z = 0.127$ cm) and a comparison with the old, coarser grid reveals the extent to which the model has been improved.

To determine if this design meets the vertical focusing and radial centering requirements (as described above), a reference ray was run in this field using the Z3CYCLONE orbit code (see Chapter 4). Figure 3.5 shows the central ray so produced while figure 3.6 shows the instantaneous center of curvature for the same ray. From this plot we can see the effect of the dee shapes on orbit centering. As expected, each successive gap has less of an effect on the orbit center as its strength (inversely

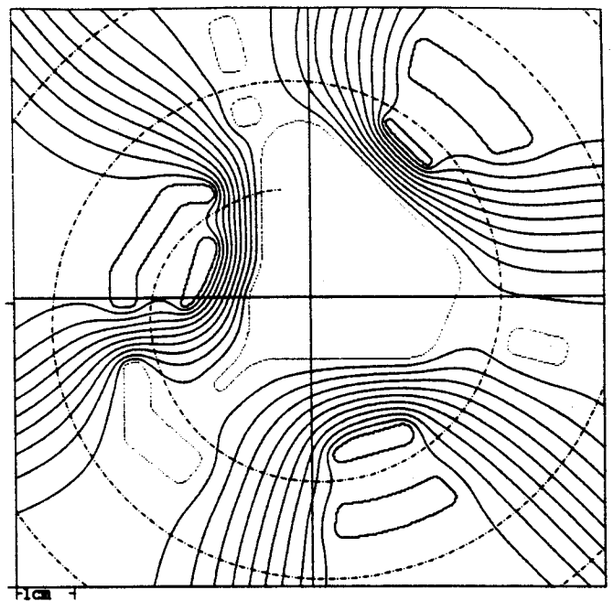

Figure 3.4: The final central region design. Shown are the median plane electric potentials. Again this is the case where all three dees are excited at equal voltages. Posts are identified by their dotted outlines. The grid dimensions were $401 \times 401 \times 25$, $\Delta x = \Delta y = 0.0254$ cm and $\Delta z = 0.127$ cm. Also shown is the path of the central ray.

proportional to the total energy) is reduced by the effect of the preceding gaps. From this central region, with the help of a small (4 gauss) first harmonic bump, a well-centered beam was produced. To determine if this central region provides adequate vertical focusing, two radially centered rays were run, one with an initial z displacement (1 mm) and one with an initial 0.1 mm displacement in p_z. The resulting phase and vertical motion can be seen in figure 3.7. There is limited growth in the z motion for both rays, indicating good vertical focusing. With a central region so designed, studies were made of machine performance and phase acceptance.

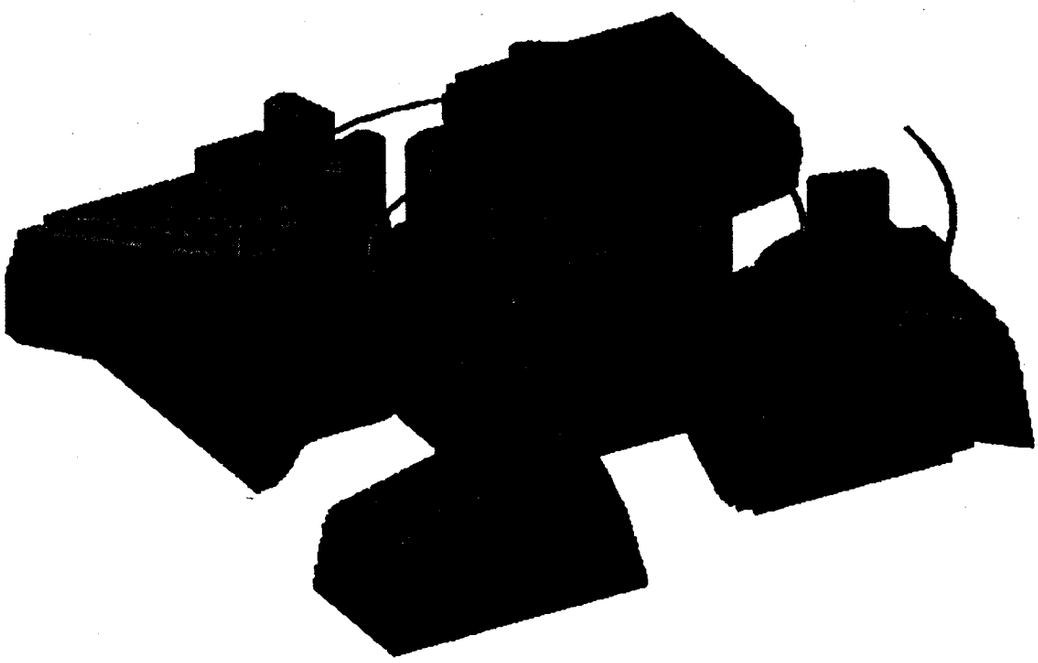

Figure 3.5: The second harmonic central region design. The view shows a cutaway of the central region electrodes below the magnetic median plane. The path of the central ray is shown and the large structure in the center where the beam originates is the inflector housing. The first channeled structure the beam encounters is the puller dee tip. There after the structures alternate between ground potential hills and high voltage dee tips. The first turn phase slit can be seen in the upper left corner. The grid dimensions were $401 \times 401 \times 25$, $\Delta x = \Delta y = 0.0254$ cm and $\Delta z = 0.127$ cm.

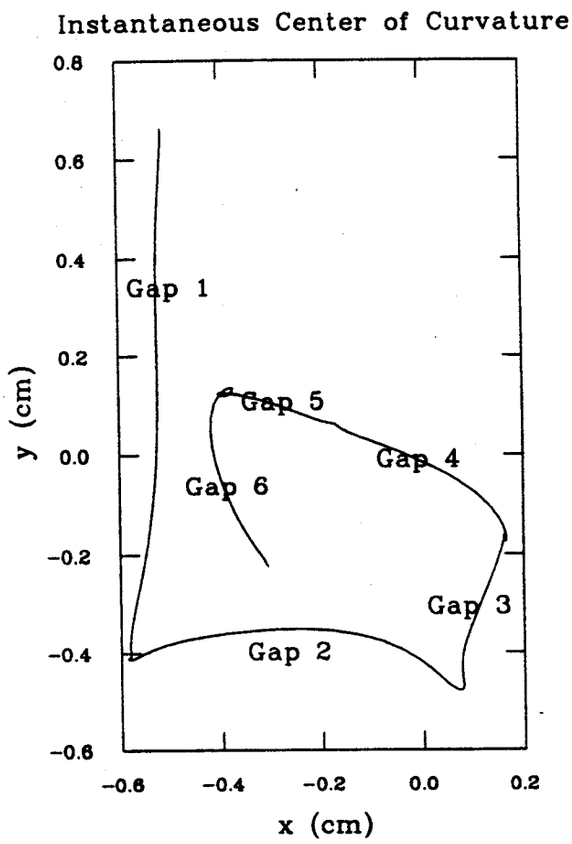

Figure 3.6: The instantaneous center of curvature for the reference ray in the new second harmonic central region. Labeled are the effects of each gap (numbered from the puller gap (1)) as seen in figure 3.4

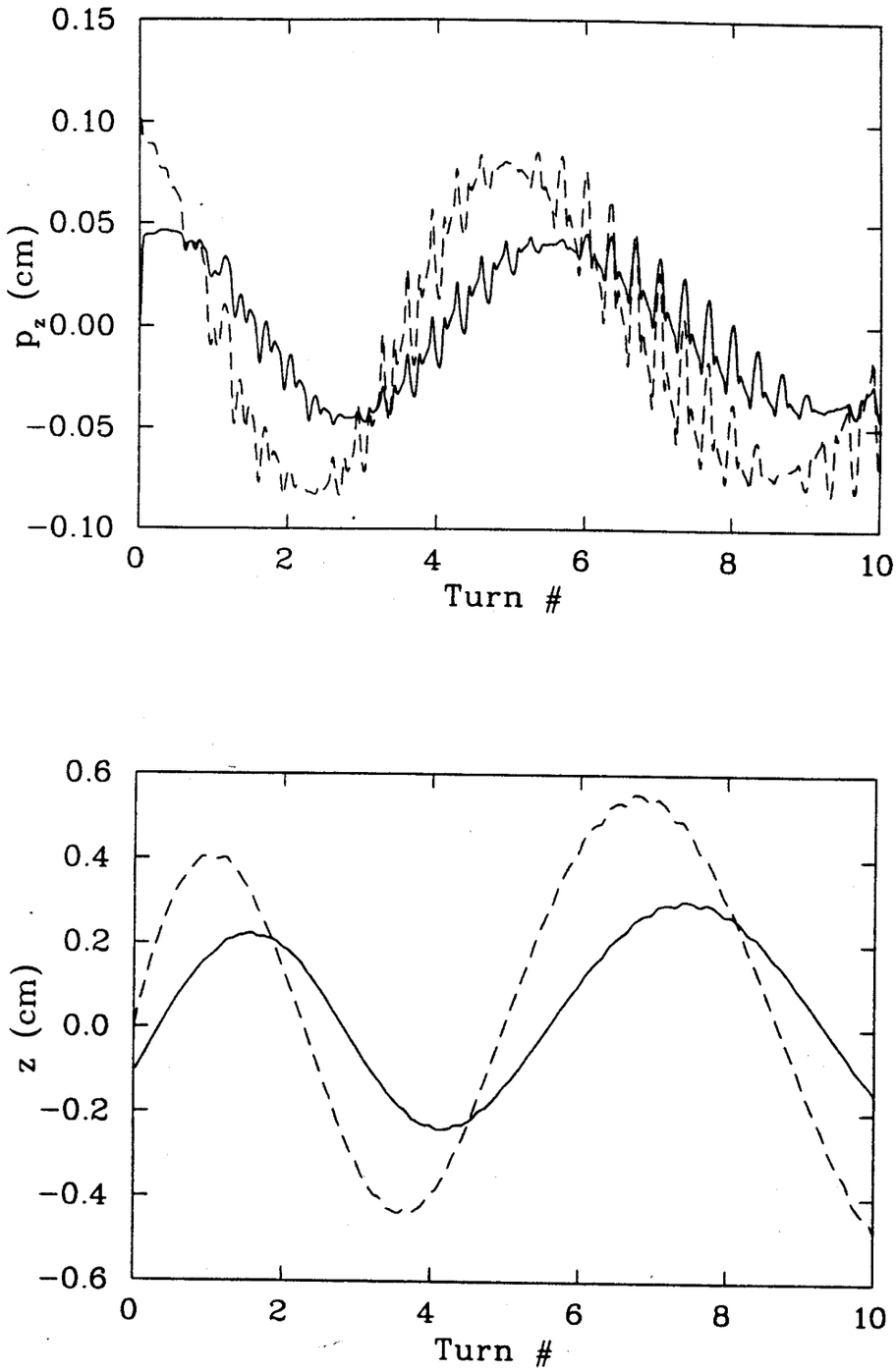

Figure 3.7: The vertical motion (p_z vs. turn (top), z vs. turn (bottom)) for the final $401 \times 401 \times 25$ central-region grid. The vertical motion shown is for particles with initial values of $z = 1.0$ mm, $p_z = 0.0$ (solid) and $p_z = 0.1$ mm, $z = 0$ (dashed).

Chapter 4

Orbit Dynamics and Phase Selection

In order to study the behavior and acceptance of the new second harmonic central region and inflector system, ions were first tracked from 3.0 m below the median plane of the K500, up the magnet axis, through a buncher, the spiral inflector and into the median plane. This was accomplished using an axial injection code which integrates the exact equations of motion for a charged particle moving in stipulated electric and magnetic fields. The on-axis magnetic field was generated using POISSON, and off-axis values were determined by an expansion in powers of radial position (see Chapter 2). The ions are first tracked through the magnetic field up to the buncher at $z = -1.6$ m. At this point the ions are given a starting time, passed through the buncher and then up to, and through, the spiral inflector. The inflector field was determined by RELAX3D runs. Upon exiting the inflector, the ion's coordinate values are stored to be used as starting conditions for a central region orbit tracking procedure.

4.1 Z3CYCLONE

Once a set of starting values is obtained at the exit of the inflector, these ions were run through the central region out to a radius of 20.0 cm, corresponding to passage through the phase selection slits, using a modified version of the Z3CYCLONE orbit code. This code integrates the equations of motion through the cyclotron's magnetic field (produced by the orbit code MONSTER [41]) and three electric fields representing the central region electrode structures (calculated using RELAX3D). The program is broken into three sections having different treatments of the electric fields.

Part I

Part I deals with motion of the particles between the source and puller and uses time as the independent variable. As with all the codes, cyclotron units (momenta in units of length) are used. The equations of motion for Part I are given in cartesian coordinates since the region of interest is small. This defines the position of, and force on, a particle as

$$\vec{R} = x\hat{i} + y\hat{j} + z\hat{k} \;\; and \;\; \frac{d\vec{p}}{dt} = q(\vec{E} + \vec{v} \times \vec{B}).$$

Rather than using t as the integration variable we switch to $\tau = \omega_{rf}t$, the RF time. Then explicitly writing the cross product above and changing to cyclotron units we have

$$\begin{aligned} \frac{d\tilde{p_x}}{d\tau} &= C_1E_x + C_2\tilde{p_y}B_z - C_2\tilde{p_z}B_y \\ \frac{d\tilde{p_y}}{d\tau} &= C_1E_y + C_2\tilde{p_z}B_x - C_2\tilde{p_x}B_z \\ \frac{d\tilde{p_z}}{d\tau} &= C_1E_z + C_2\tilde{p_x}B_y - C_2\tilde{p_y}B_x. \end{aligned} \tag{4.1}$$

Here, $C_1 = \frac{q}{hm\omega_0^2} = \frac{qa^2}{hmc^2}$ where $a = \frac{c}{\omega_0}$, and $C_2 = \frac{1}{hB_0}$.

Part II

Part II tracks the particles through the remaining electric fields and explicitly calculates the effects of crossing the gaps from the exit of the puller out to 20 to 25 cm. The fields used in Part II extend from the machine center and thus cylindrical coordinates are used with θ as the independent variable. Relativistically then, a particle's position and momenta are given by

$$\vec{R} = re^{i\theta}\hat{u} + z\hat{k},$$

and

$$\vec{p} = p_r e^{i\theta}\hat{u} + p_\theta e^{i\theta} i\hat{u} + p_z \hat{k}$$

with

$$p_r = \dot{r}m\gamma,\ p_\theta = r\dot{\theta}m\gamma,\ and\ p_z = \dot{z}m\gamma.$$

From these equations we can derive the following equations of motion,

$$\begin{aligned}
\frac{d\tilde{p}_r}{d\theta} &= \frac{\gamma a^2 q r E_r}{mc^2\tilde{p}_\theta} - \frac{rB_\theta\tilde{p}_z}{B_0\tilde{p}_\theta} + \frac{rB_z}{B_0} + \tilde{p}_\theta, \\
\frac{d\tilde{p}_z}{d\theta} &= \frac{\gamma a^2 q r E_z}{mc^2\tilde{p}_\theta} + \frac{rB_\theta\tilde{p}_r}{B_0\tilde{p}_\theta} - \frac{rB_z}{B_0}, \\
\frac{d\tilde{p}_\theta}{d\theta} &= \frac{\gamma a^2 q r E_\theta}{mc^2\tilde{p}_\theta} + \frac{rB_r\tilde{p}_z}{B_0\tilde{p}_\theta} - \tilde{p}_r,
\end{aligned} \tag{4.2}$$

and

$$\frac{d\tau}{d\theta} = h\gamma\frac{r}{\tilde{p}_\theta}.$$

The electric potential values are provided by interpolation in a grid calculated by the relaxation code RELAX3D.

Part III

Part III tracks the particles from the exit of Part II out through the rest of the machine. The equations of motion are the same as for Part II except that the electric

field terms are identically zero. The effect of the accelerating gaps is approximated by an impulse given by,

$$\delta E_{i,j} = (-1)^j q V_{di} \sin(\omega_{rf} t_{ij} - k_i), \tag{4.3}$$

$$\delta p_r = -\frac{\delta p^2 \ tan(\alpha)}{(p_\theta - p_r \tan(\alpha)) + \sqrt{(p_\theta - p_r \tan(\alpha))^2 + \delta p^2(1 + \tan^2(\alpha))}} \tag{4.4}$$

where $\delta p = sqrt(2\gamma + \frac{\delta E}{mc^2})(\frac{\delta E}{mc^2})(mc)$ is the total impulse caused by δE, α is the angle between the $\hat{\theta}$ direction and a line perpendicular to the gap, $i = 1, 2, 3$ is the dee number, $j = 1, 2$ is the entrance or exit of a given dee, $V_{d,i}$ is the voltage of the i^{th} dee, and (ω_{rf}t$_{ij}$-k$_i$) is the phase for the i,j gap crossing.

Code Outputs

The modified version used for these studies extends the number of electric fields used from two to three, and removes ions whose paths intersect electrode or dee structures. If at anytime during the calculation an ion's path takes it through an electrode, into a dee, turns back towards the machine center or becomes destructively off centered, the ion is removed from calculation. Ions which were successfully run out to extraction had their r and ϕ values saved at strategic positions en route. At the extraction radius all pertinent ion values are saved. The 'relevant positions' for recording r,ϕ values correspond to phase slit positions. During design of the central-region electrode structures, it was determined that the optimal place for a first-turn phase slit was centered at $r = 3.9$ cm and $\theta = 112°$. This location, along with the present phase selection slit locations (on the three hill centers at $r = 17.88$ cm), made up the four r,ϕ data retention positions. Once a full set of starting conditions was tracked through the entire path (from $z = -3.0$ m out to $r = 68.0$ cm in the K500), this final data set was used to analyze the beam properties and timing spectra for the set as well as the effect of the phase slits.

4.2 Starting Conditions

In order to calculate the percentage of the input DC beam in the final 3° bandwidth, as well as the beam properties, a range of emittances was tracked up the machine axis, through the spiral inflector and central region, and out past the phase selecting slits. Each set of starting conditions consisted of a uniform circular distribution of points (one point per π mm-mrad) spanning the emittance area in x,p_x and y,p_y. Each point in x,p_x space corresponded to a set in y,p_y which spanned the entire emittance area. In this way, a spatially coupled set of 5625 starting conditions was obtained. This coupled set of points could then be tracked from 3 m below the median plane out through the K500.

In order to simulate the time structure of the incoming beam, coupled x,p_x/y,p_y sets were started each separated by 2° RF. This now complete set of starting conditions was then passed through the buncher (located 1.6 m below the median plane) before entering the inflector. To limit the number of points necessary to cover the relevant starting conditions, limits were placed on the range of starting times allowed. Realizing that the acceptance of the puller gap is limited to a τ range of 180°, the starting time values were limited to include only those times (at $z = -1.6$ m) that arrive at $z = 0.0$ m in the allotted interval. The major factor in determining the overall range of starting times that need to be run is then, the buncher.

4.3 The Buncher

The present K500 RF buncher [18] is designed to be run in one of two modes. It can provide either a single first harmonic of the RF voltage or a second mode, providing a voltage containing both first and second harmonic. The purpose of adding the second harmonic is to more accurately reproduce the desired saw-tooth bunching voltage.

The net voltage provided by the buncher is given by

$$V_{buncher} = V_{gap}[\sin(\tau - \tau_0) - V_{1,2}\sin(2(\tau - \tau_0))]$$

where τ_0 is the time about which beam is bunched, V_{gap} is the buncher gap voltage and $V_{1,2}$ is the relative voltage contributions of the first and second harmonic excitations. The effect of the buncher is included in MYAXIAL as a δp_z impulse to the ion's axial momentum, and is given (in the small gap approximation) by equations 2.14 and 2.13. Figure 4.1 shows $V_{buncher}$ vs time for both the single and double harmonic modes as well as the corresponding timing spectra at the exit of the inflector for an initial 50π mm-mrad emittance. In the first plus second harmonic mode a value of $V_{1,2} = 0.30$ was found to best fit the ideal saw-tooth curve. In order to determine the value of constructing the second harmonic systems, orbits were run using both the first and first plus second harmonic modes. Since the first plus second mode is more effective, the number of starting times needed to cover the accepted τ space increased from 70 (for the first harmonic mode and corresponding to 140° RF) to 130 (260° RF) thereby increasing the computer run time.

4.4 Injected Beam Dynamics

4.4.1 Yoke and Spiral Inflector

The initial coupled 75π mm-mrad phase space begins its trek through the cyclotron from 3 m below the median plane. The beam must pass through the magnet fringe field and yoke before entering the inflector. MYAXIAL uses the kinetic equations of motion so, before any examination of phase space conservation can be undertaken, the coordinates must be transformed into their canonical counterparts as discussed in Chapter 2. Figure 4.2 shows the resultant phase spaces at the entrance to the inflector. If one compares the initial and final emittances of the beam on transport

Table 4.1: Calculated emittance along beam path. Shown are the calculated values and the same values normalized to $r = 68.0$ cm.

Location	Radial Space (mm-mrad)		Axial Space (mm-mrad)	
	Total	Normalized	Total	Normalized
z=-3.0 m	75.0π		75.0π	
Inflector Entrance	125.0π		125.0π	
Inflector Exit	127.0π	2.3π	108π	1.95π
r=20.0 cm	7.5π	2.21π	6.3π	1.9π
r=68.0 cm	2.1π	-	1.9π	-

through the yoke, (Table 4.1) we see a large increase in emittance (from 75π mm-mrad to 125π mm-mrad). Since the symmetric nature of the beam and use of canonical momenta would seem to prohibit this, some other cause must be found. The two sources of this growth have been discussed in Chapter 2. The first is the effect of the buncher on the beam. In the approximation used, the buncher adds a time-dependent delta function kick to the energy of the ions. It also adds a time dependence to the propagation of the phase space of the beam. The emittances at the various times will now smear out when graphed at a single location. The second source of emittance growth is the initial coupling of the starting conditions. This coupling is not removed by transformation to the Larmor frame and results in an additional emittance growth.

Upon traversal of the inflector, the phase spaces are further mixed and distorted. The inflector's effect on the beam can be seen in figure 4.2. The inflector breaks the symmetry of the phase spaces and it is particularly interesting to note that the beam is not symmetric in z.

In addition to the spatial distortion caused by the inflector, there is an additiona time spread which cannot be compensated for by the buncher. The buncher voltage is set to compress the time spread of rays which travel along the machine axis. Fo off-axis rays there will be an additional time spread caused by their differing pat

lengths through the remainder of the yoke and the spiral inflector. By looking at the calculated arrival times at both the inflector entrance and exit the resultant spread caused by this can be clearly seen. Figure 4.1 shows the time spread at both of these positions. Clearly a large portion of the final spread is caused by traversal through the spiral inflector. This is not surprising considering the non linear nature of the full range of the inflector aperture covered by the beam.

4.4.2 Machine Acceptance

Of the portion of the injected beam that reaches the inflector exit, only a fraction will be accelerated to extraction. Losses due to vertical focusing limitations, collision with central region structures, and centering errors will constrain which starting conditions will be successfully accelerated. Additionally, only a small fraction of the beam will be transmitted into the acceptable 3° FWHM phase width. By combining the effects of all these factors we can determine a phase-space acceptance (at the inflector exit) for the beam. Figure 4.3 shows the portion of the 75π radial phase space that survives to the exit of the inflector, the portion that is accelerated to extraction and the fraction of this which is successfully accelerated into the tolerated 3° phase peak.

It should be possible to use this accepted phase space to determine the final emittance of the beam at extraction. If we use an adiabatic approximation for the change in emittance between the injection point and extraction ($\epsilon_{ext} \cong \epsilon_{inj}\ p_{0_{inj}}/p_{0_{ext}}$) a final emittance can be calculated. Using this, a value of $\epsilon_{ext} = 2.23\pi$ mm-mrad is obtained. This should agree with the final value obtained by running these orbits to extraction if there are no significant higher order effects and the coupling between the radial and E-ϕ spaces is minimal. We can determine an upper bound on the emittance growth which would be caused if such effects were prevalent by examining the eigenellipse at the inflector exit.

The K500 acceleration process defines a region of phase space for which particles will be successfully transported through the machine. This space is defined by an eigenellipse around the accelerated equilibrium orbit [42]. Any phase space injected into the machine will precess within the eigenellipse which encloses it. Thus, a properly injected beam will enter the cyclotron with the correct phase-space shape and orientation so as to match the eigenellipse. Such a beam should see no distortions to the radial phase space. If the injected space does not match the eigenellipse and there are significant higher order effects, the space will distort itself so as to fill the eigenellipse and thus show an emittance increase. Figure 4.4 shows the eigenellipse at injection superimposed on the accepted phase space. If we use instead the emittance defined by this eigenellipse we find a value for the emittance at extraction of 4.1π mm-mrad which is then an upper bound on the emittance growth. An examination of the emittance at extraction (see below) however shows a value of 2.1π mm-mrad.

The vertical acceptance of the machine will be limited by the amount of vertical focusing available in the first few turns. This in turn will set a limit on the z, p_z, τ_0 starting values that will be accelerated. Figure 4.5 shows the accepted vertical space (for the total beam and the phase reduced beam) at the inflector exit. The losses between what arrives at the inflector and the accepted space are not dominated by vertical losses. The calculations show a vertical loss of only 0.5% over the entire range of the machine, indicating adequate vertical focusing. The reduction in size comes from the phase selection process, indicating a r-z correlation at the inflector exit.

4.5 Phase Selection

Once the beam has entered the cyclotron the only method available to remove the unwanted phases is to introduce an element which intercepts these particles. In order to do that and retain the central phases, a r-ϕ correlation is introduced into the beam at the locations of the intercepting elements.

As discussed in Chapter 3, the electrode positions in the central region are set so that a ϕ-dependent radial shift is created at the first-turn window slit. Thus, by centering the window slit on the central ($\tau_0 = 210°$) ray and adjusting its width, we can intercept and remove the central rays for the surrounding times. It should be noted that to accurately assess the extent of the phase cutting that this slit produces, these central rays must be surrounded by an appropriate phase space. For certain starting times (even those whose central rays are excluded by the slit) elements of their phase space may then extend into the aperture of the first turn slit and therefore survive. This limits the effect of this slit and it is therefore used only as a coarse phase selection.

The fine phase selection is done through the use of the $r = 18$ cm phase pins. This location is some 20 turns after the first turn slit. By this time the beam has developed a phase-dependent radial spread due to the differing energy gained by each starting time. As was discussed in Chapter 1, we can adjust the magnetic field so as to increase the r-ϕ correlation in the beam. We must then re-adjust the field so that after the slits the field is in such a state that the average field over the entire acceleration (injection to extraction) is again isochronous.

Once we have created the required radial spread at the phase pin location we can insert these pins and remove the unwanted times. Figure 4.6 shows the r-ϕ correlation at the pin locations and the position of the two phase pins. From the

picture we can see that pins are placed to intercept rays over several turns. The pins are also positioned such that one pin does the majority of the cutting while the other is used to clean up what the first pin (and first turn slit) miss.

4.5.1 Phase Selection Computer Program

Extraction requirements restrict the timing spectra coming out of the central region to 3° FWHM. Presently, the K500 is equipped with two phase slits located on the 0° and 120° hills at a radius of 17.88 cm. These slits consist of two movable tungsten blades that are used to intersect the beam [10]. There is the capability to add a third slit at an identical radius on the third, 240° hill. In the design of the central region the position of a fourth possible slit, consisting of a fixed aperture window was identified. Thus there are four slits which may be used in phase selection.

To model the effect of these slits a program was used which simulates the effect of various slit combinations. This program accepts r,ϕ orbit data at specified slit positions and a second set of ϕ data at the final beam position, all provided by Z3CYCLONE. At each slit position a separate pin (labeled A,B, and C) can be inserted. The position of each pin can be adjusted, it can be inserted or removed, and the width of the pin can be set. In this way any combination of pins, pin positions and pin width can be achieved. The program then identifies which ion orbits (if any) intersect with each pin and removes these from consideration. The final collection of surviving ions is then binned according to final phase and a beam timing spectrum is produced. Additionally, a variable width, first turn, window slit can be inserted to further reduce the final timing spectra. By using the r,ϕ output of the central region orbit code a measure of the acceptance of the cyclotron into a 3° FWHM timing region which can be expressed as a percentage of the input DC beam (at $z = -3.0$ m) surviving for various starting emittances and buncher modes.

4.5.2 Phase Acceptance Results

A variety of starting emittances was calculated in order to determine the performance of the injection plus central region design. Starting emittances of 25, 50 and 75π mm-mrad in each of the coupled x,p_x/y,p_y phase spaces were tracked through the phase selection process. Additionally, in order to determine the relative gain of constructing the first-plus-second-harmonic buncher system, these starting emittances were run in both buncher modes and the various parameters of the phase selecting slit system were adjusted to give a 3° FWHM peak containing the maximum number of surviving ions. Figures 4.7, 4.8 and 4.9 show the timing spectra before the first turn slit, just after this fixed window, and then the final 3° peak obtained by using the outer phase pins for the various emittance/buncher mode combinations. Table 4.2 shows the slit parameter settings for these plots as well as the percentage of the injected DC beam which survives in the appropriate bandwidth. As can be seen, using the first plus second harmonic buncher mode provides a 50 to 60 percent increase in the surviving current. Additionally there is the expected fall-off in acceptance with initial emittance growth.

It should be noted that the timing spectra just prior to the first turn slit already show signs of phases being trimmed. The tail found on the spectrum at the exit of the inflector is missing or is markedly reduced. This is due to a convenient pre-slit phase selection performed by the 300° and 60° dee posts. Rays with more extreme timing errors in either the early or late direction are trimmed by passage near these structures.

Table 4.2: Parameter Values Resulting in 3° FWHM Peak for an ECR voltage of 30 kV.

Emittance	R Position(cm)/Thickness(cm)			
	Slit A	Slit B	Slit C	1^{st} Turn Slit
1^{st} Harm. Mode	$V_{buncher}$ =(24 kV)sin(τ-210.)			
25π	17.673/0.233	17.646/0.233	Not Used	Not Used
50π	Not Used	17.282/0.231	17.503/0.231	4.000/0.127
75π	17.648/0.244	17.292/0.244	17.546/0.244	3.937/0.127
1^{st}+2^{nd} Harm. Mode	$V_{buncher}$=(36 kV)[sin(τ-210.)-(0.15)sin(2(τ-210.))]			
25π	17.672/0.239	17.648/0.239	17.496/0.239	Not Used
50π	Not Used	17.240/0.404	Not Used	Not Used
75π	17.615/0.241	17.309/0.241	17.546/0.241	1.775/0.450

Table 4.3: Percentage of DC Beam in 3° FWHM Peak

Buncher Harmonics	Initial Emittance		
	25π mm-mrad	50π mm-mrad	75π mm-mrad
1^{st} Harmonic Only	11.0%	5.8%	2.9%
1^{st} and 2^{nd} Harmonics	16.7%	9.5%	5.5%

4.6 Accelerated Beam

Once the beam has been reduced to the 3° FWHM phase width all that remains is to examine its properties at the extraction radius. Considering the phase-dependent centering error introduced in the beam for the purposes of phase selection (see Chapter 3) there will be phases with a large range of off- centering values. To see why this is a concern in reference to beam quality, we note that the shape of the average field at a particular radius determines a range of centering errors with which the beam will exhibit stable coherent oscillations [11] [12]. This range defines a stable region in the radial phase space. The size of this space changes with the field profile, so while a beam with a particular centering may be in the stable region at one radius, it may exist outside of the region at another. The size of the centering error becomes most critical as the value of ν_r (the number of coherent oscillations per turn) reaches 1.0. At this point the stable region vanishes [13] [14] [15]. This can be seen in figure 4.10 which depicts the size of the stability region both before and after the $\nu_r = 1$ resonance.

To determine the effect of such a displacement on beam quality, a set of eigenellipses were run from the phase pin radius out to 68.0 cm. The ellipses were initially 8π mm-mrad in emittance and were run with initial centering errors (coherent radial oscillation amplitudes) of 0, 0.65, and 1.3 mm. The results of these runs can be seen in figure 4.11 which shows the ellipse both before and after crossing the final $\nu_r = 1$ resonance. There does not appear to be any significant deformation of the phase spaces prior to resonance crossing. Even after the focusing resonance there is little distortion in the initially 0.65 mm offset phase space, and the 1.3 mm offset space shows a change in shape but no large increase in emittance. This provides a level of confidence that the induced centering error will not significantly harm the behavior

of the accelerated beam.

Having established this, the full, phase reduced space was then run out to extraction. The beam which successfully navigates the central region and phase selection pins was traced out to a radius of r≈ 68.0 cm. Figures 4.12 and 4.13 show the radial and axial phase spaces (respectively) at this radius for the last two turns in the machine. The 0.4 cm radial and vertical size of the beam is reasonable for extraction purposes, however the turns are not separated. In order to separate the turns, the orbits were rerun using a 10 gauss first harmonic bump to drive the $\nu_r = 1$ focusing resonance located at $r = 62.0$ cm. As described in numerous papers [13] [14] [15], a first harmonic perturbation to the field can be used in conjunction with the $\nu_r = 1$ crossing to induce a radial oscillation in an initially centered beam. This can be used to create additional turn separation needed for extraction [6].

By properly placing the azimuthal position and adjusting the strength of the extraction bump, good turn separation at extraction was achieved. Figures 4.12 and 4.13 show the radial and vertical phase spaces at extraction after the beam was run using the extraction bump. Now there is good turn separation (≈ 2 mm) between the first extracted and last interior turns. The distortions caused by passing through the $\nu_r = 1$ resonance off center, are minimal. The radial and vertical size of the beam has not been appreciably affected and the turn separation is increased. An examination of the energy spread of the final turn shows a relative spread of 0.1%.

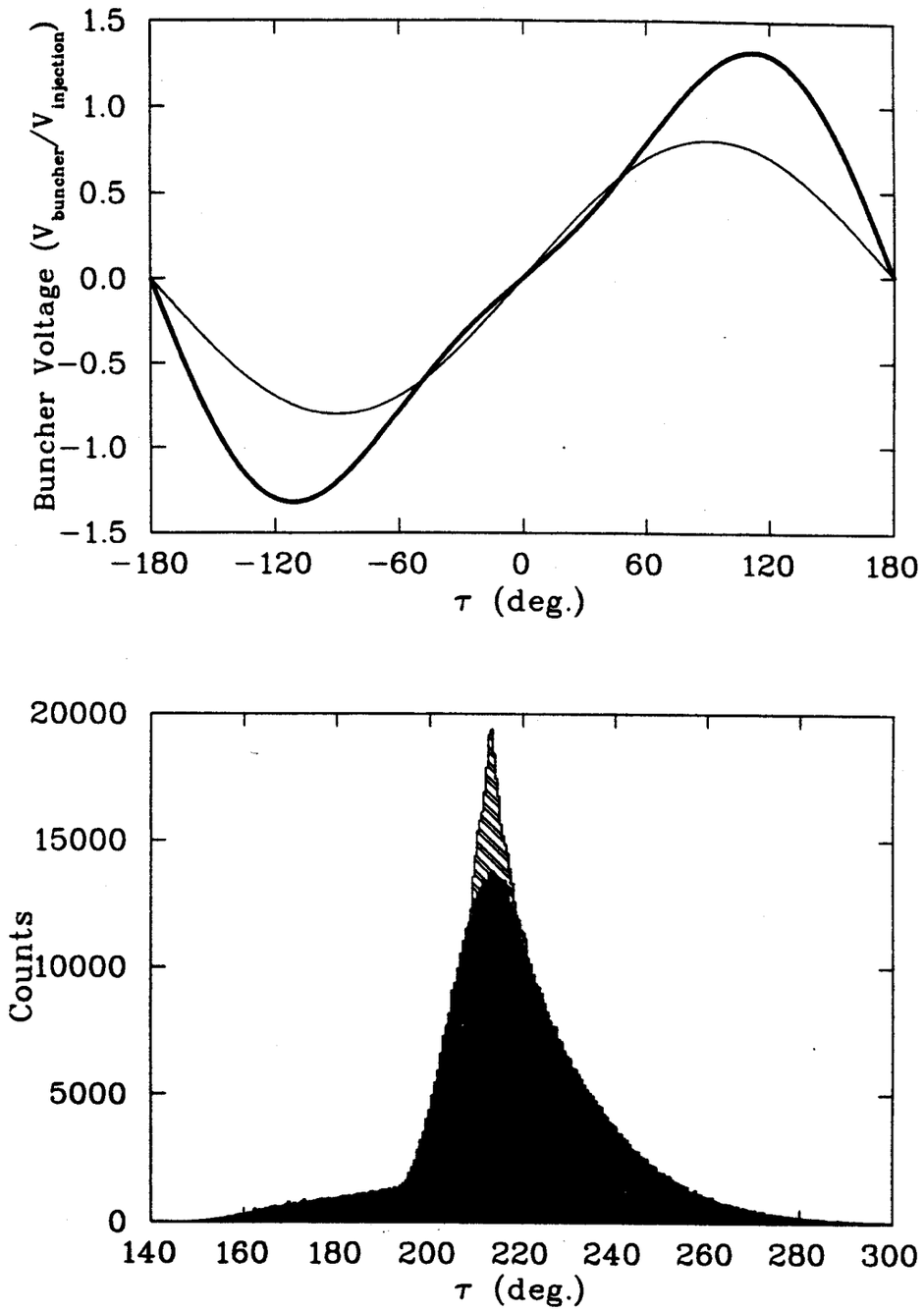

Figure 4.1: Top: Buncher voltage expressed as a percentage of the injection voltage. Both the first and first plus second harmonic modes are shown. Use of the first plus second mode extends the effective region by 40%. Note that the value of the first harmonic voltage is different in the two cases. Bottom: The final timing spectra at the exit of the inflector for both buncher modes.

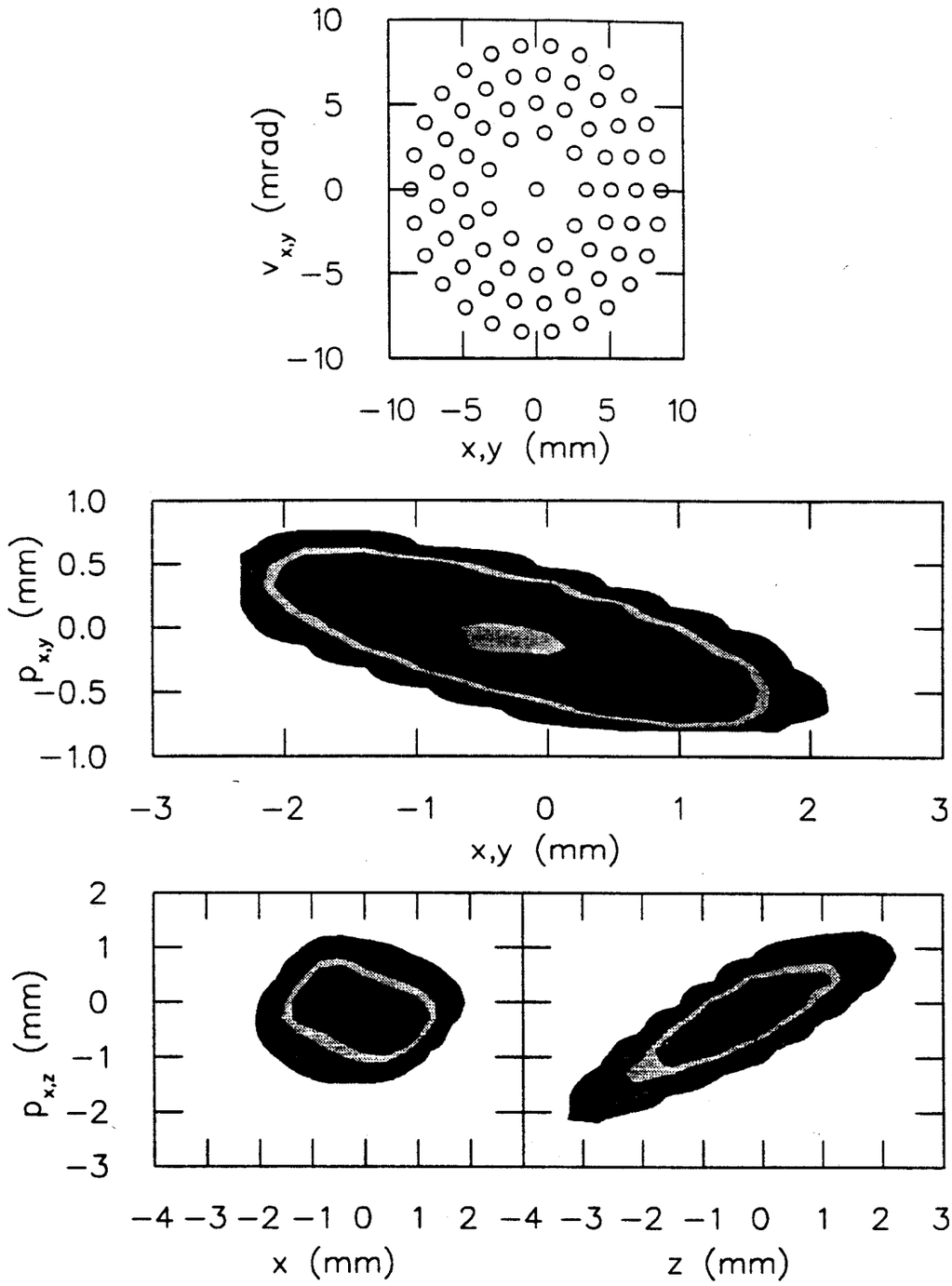

Figure 4.2: The evolution of a 75π mm-mrad coupled phase space. The top figure shows the space at $z = -3$ m. The middle plot shows the same space after passing through the K500 axial fields, the focusing solenoid, and the buncher. While the final graphs are the phase space at the exit of the inflector, before entering the K500 central region. The graphs represent coupled phase spaces with an initial $\Delta\tau = 260°$.

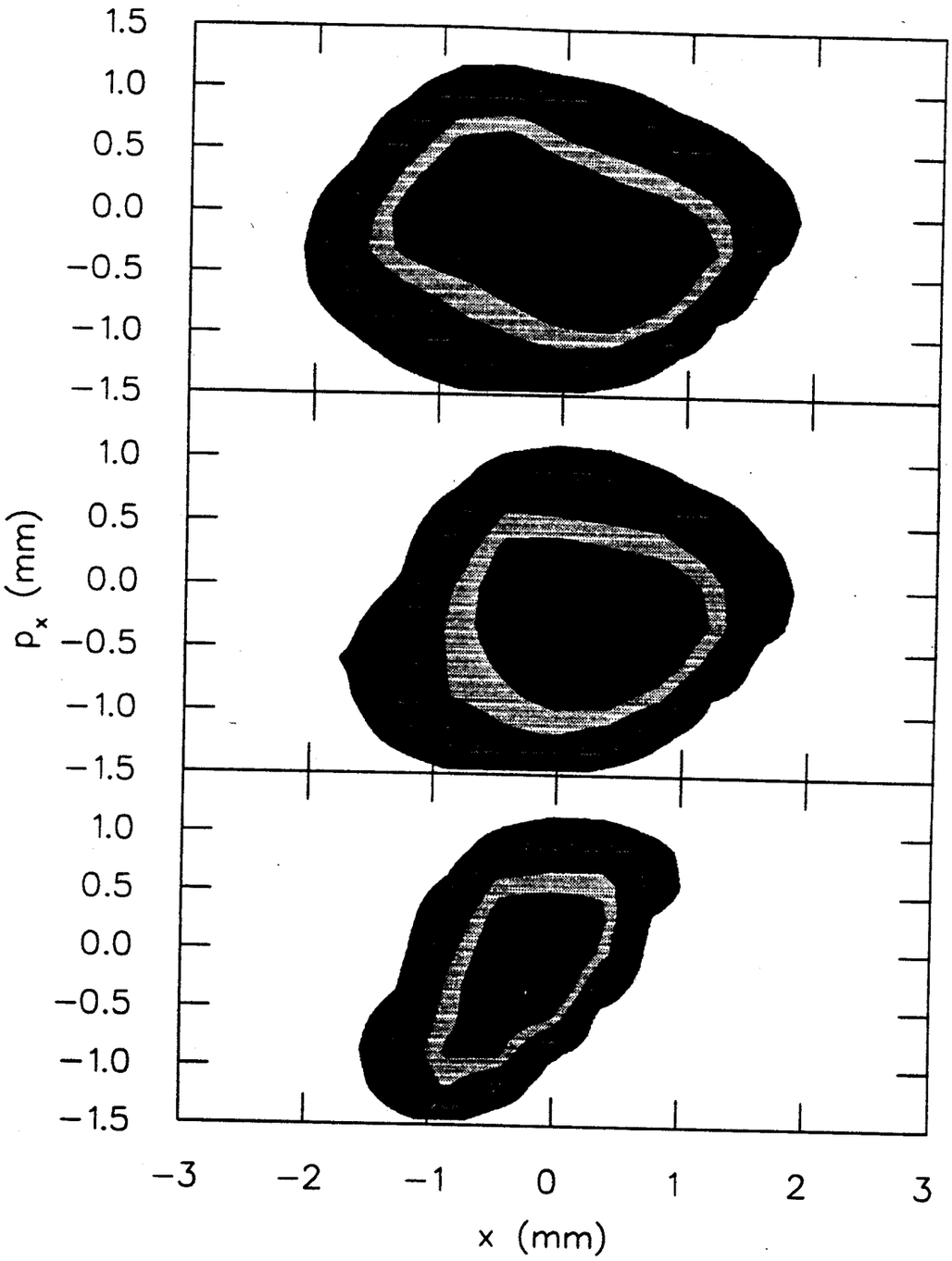

Figure 4.3: The radial phase space acceptance at the exit of the inflector. The figures represent the radial space accepted by the inflector, the K500 and the K500 with phase selecting mechanisms in place. The graphs represent coupled phase spaces with an initial $\Delta\tau = 260°$ and an initial emittance of 75π mm-mrad.

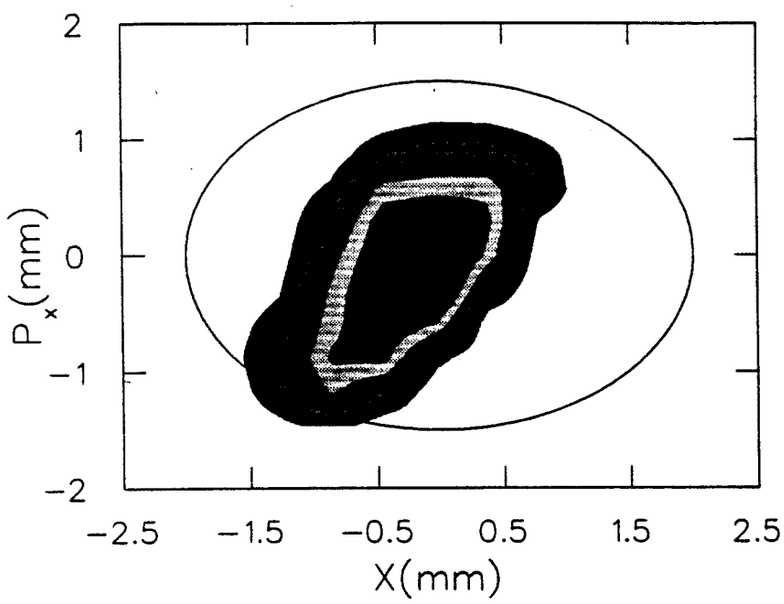

Figure 4.4: The eigenellipse at the exit of the inflector which completely encloses the accepted radial phase space (3° FWHM). If there are significant higher order effects the accepted area can grow so much as to fill a phase space area equal to that of the eigenellipse.

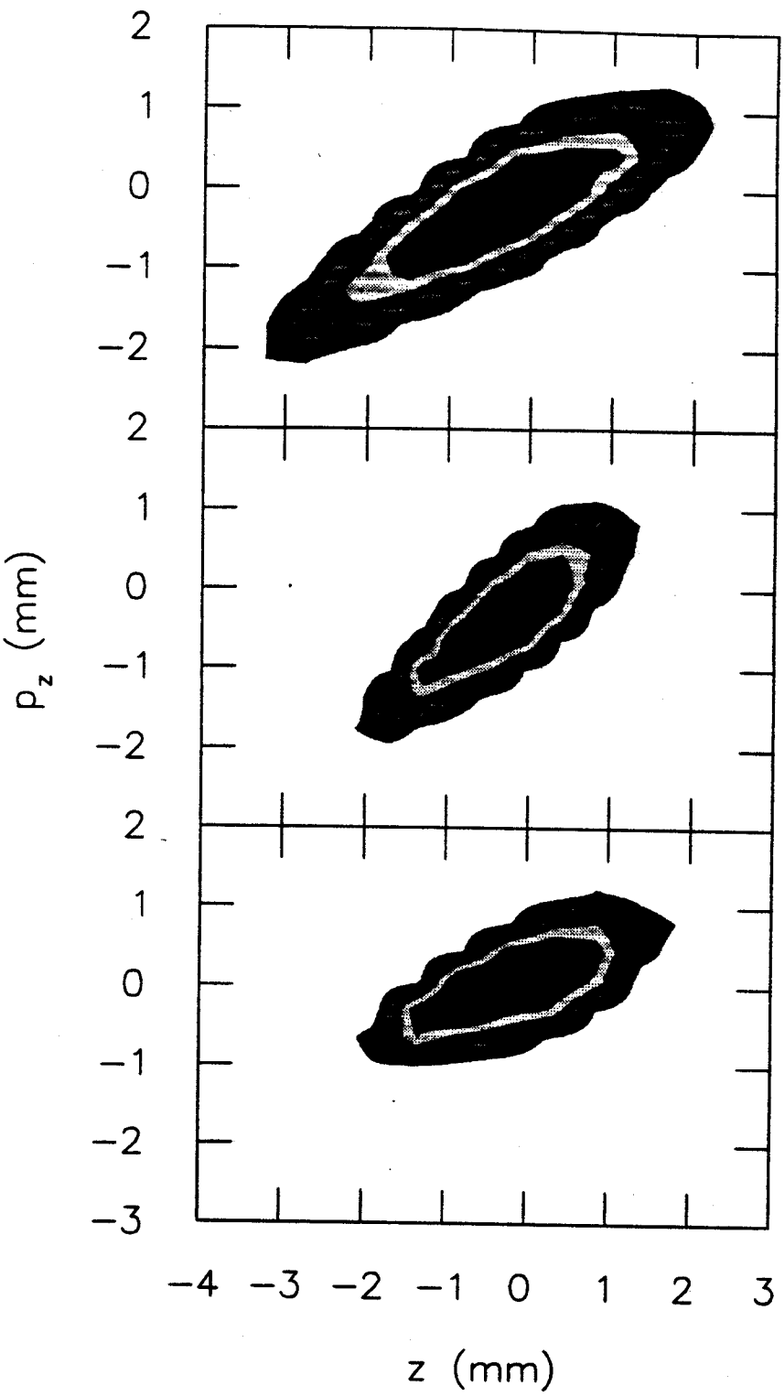

Figure 4.5: The axial phase space acceptance at the exit of the inflector. The figures represent the phase space after transport through the inflector, the portion of this space that is accepted by the K500 central region and the portion accepted by the K500 with phase selecting mechanisms in place.

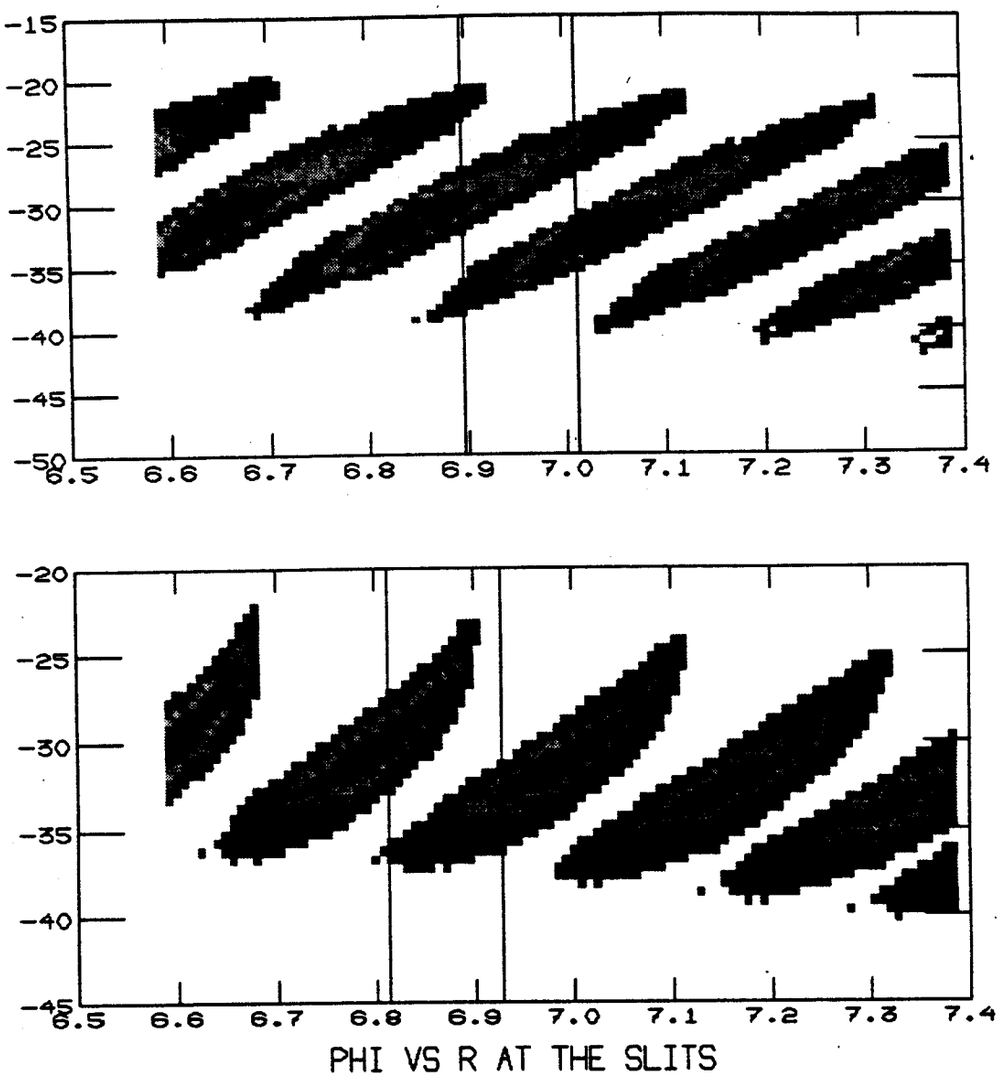

Figure 4.6: The r vs. ϕ plot at the location of the two phase pins presently in place. Portions of five different turns can be seen. Also shown is the locations of the two pins. Rays which intersect these pins are removed.

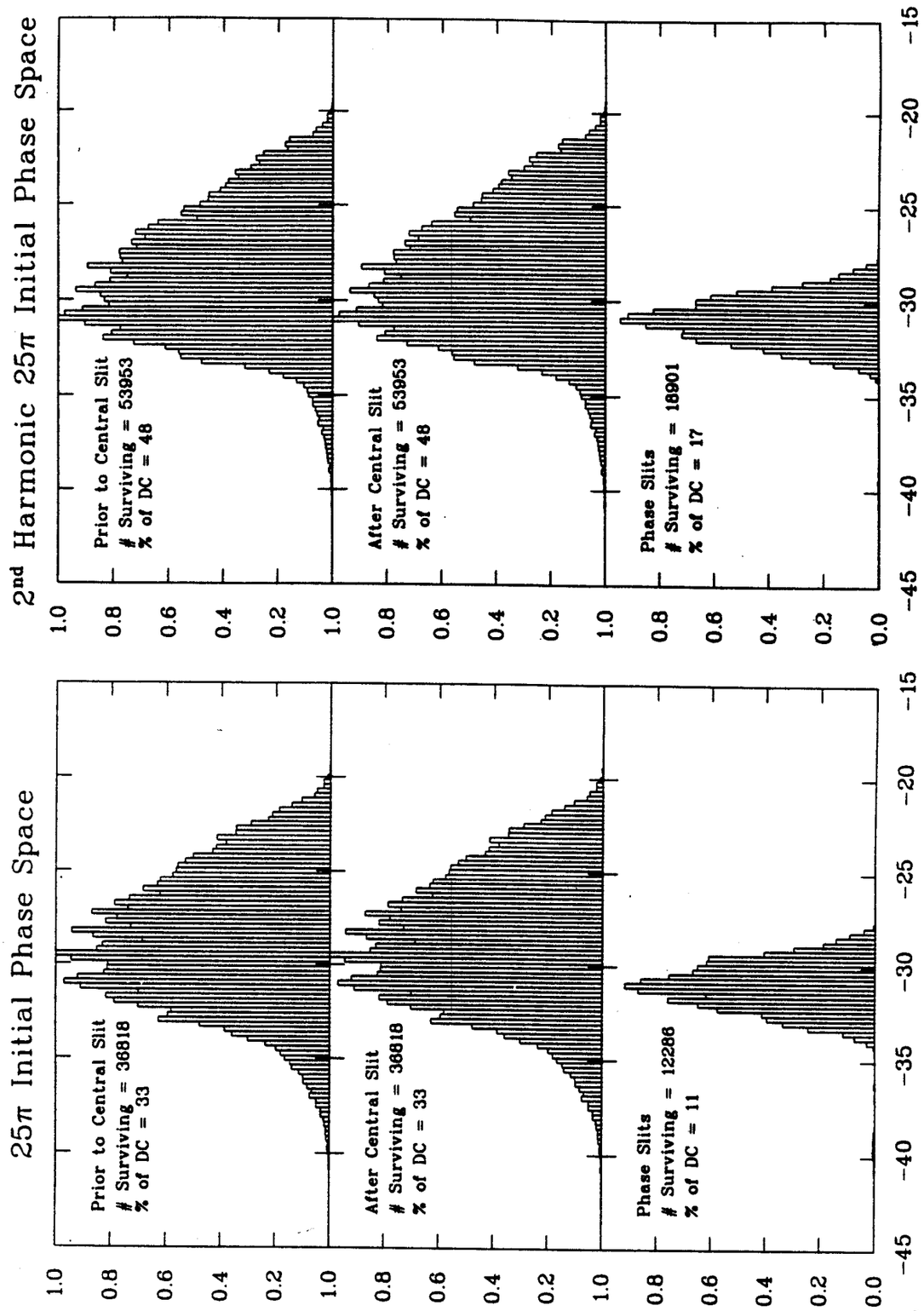

Figure 4.7: The calculated timing spectra for an initially 25π mm-mrad space. Shown are the spectra just before the first turn slit, just before phase pins and after both phase selection devices.

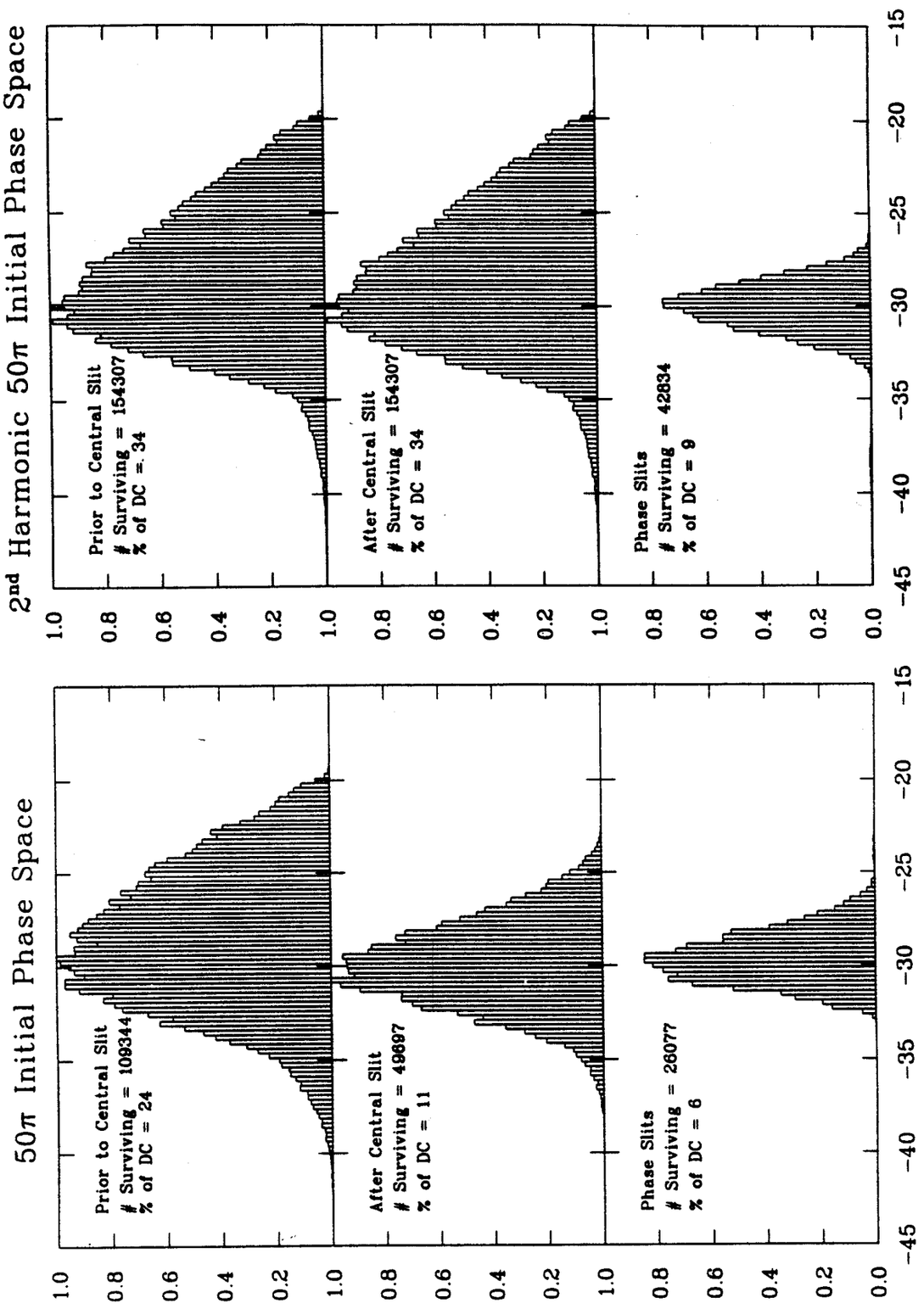

Figure 4.8: The calculated timing spectra for an initially 50π mm-mrad space. Shown are the spectra just before the first turn slit, just before phase pins and after both phase selection devices.

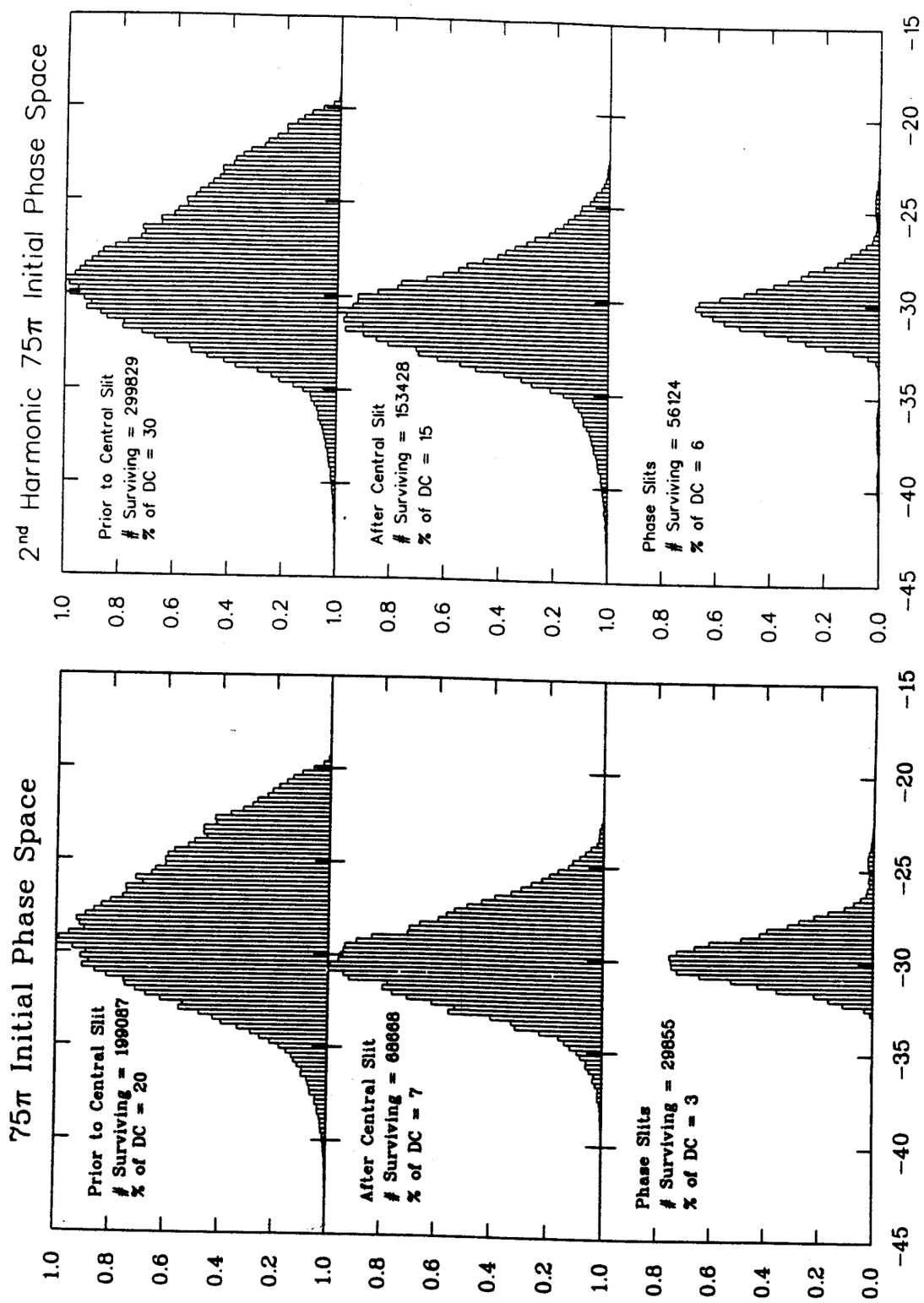

Figure 4.9: The calculated timing spectra for an initially 75π mm-mrad space. Shown are the spectra just before the first turn slit, just before phase pins and after both phase selection devices.

120° fields

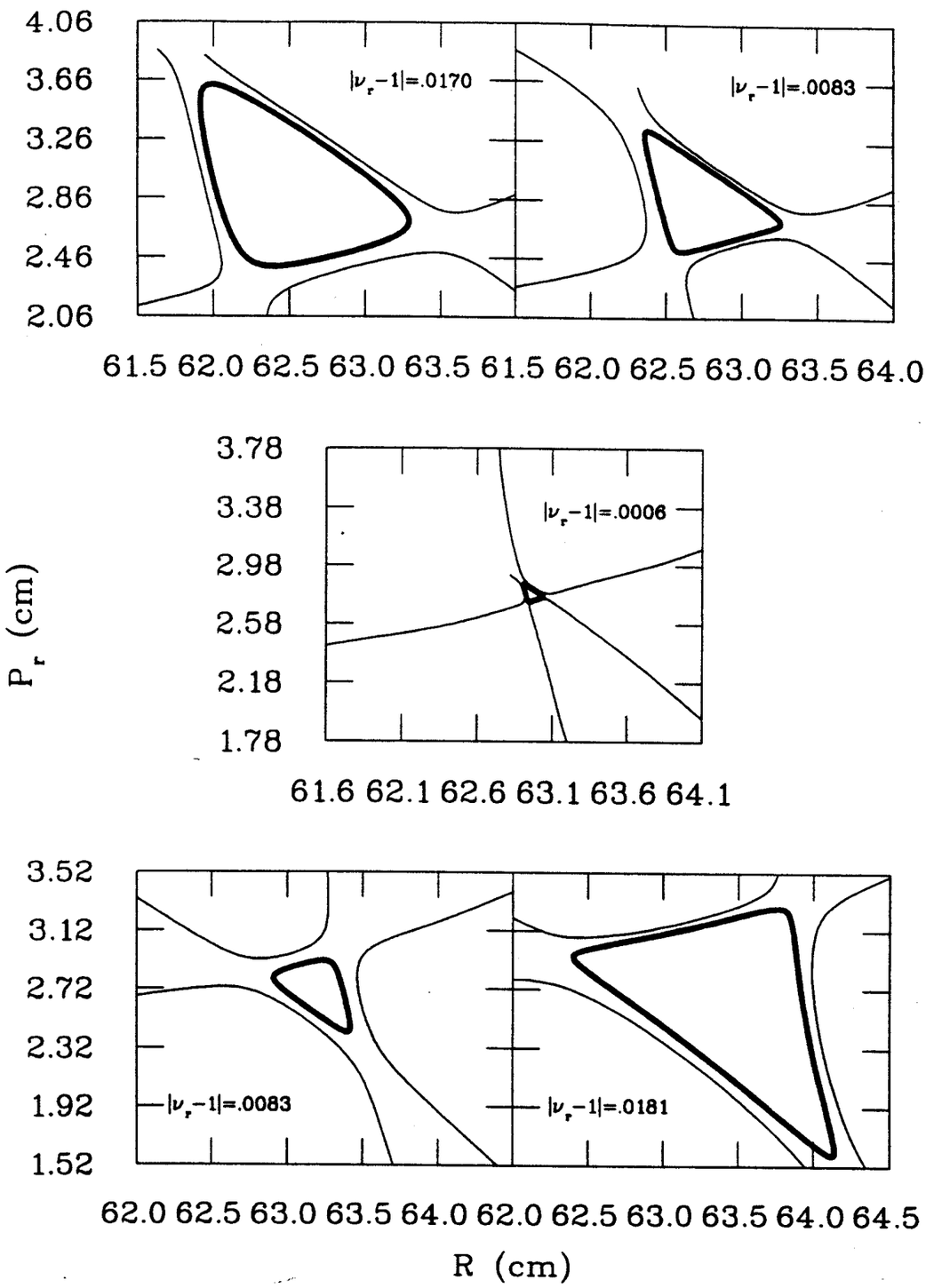

Figure 4.10: The size of the radial stability region near $\nu_r = 1$. The five pictures correspond to energies equally sapced between 14.0 and 14.6 MeV/u. The double thickness lines are the approximate boundaries to the stable region at each energy. As the $\nu_r = 1$ resonance is approached the stable region quickly shrinks and then reappears as the resonance is crossed.

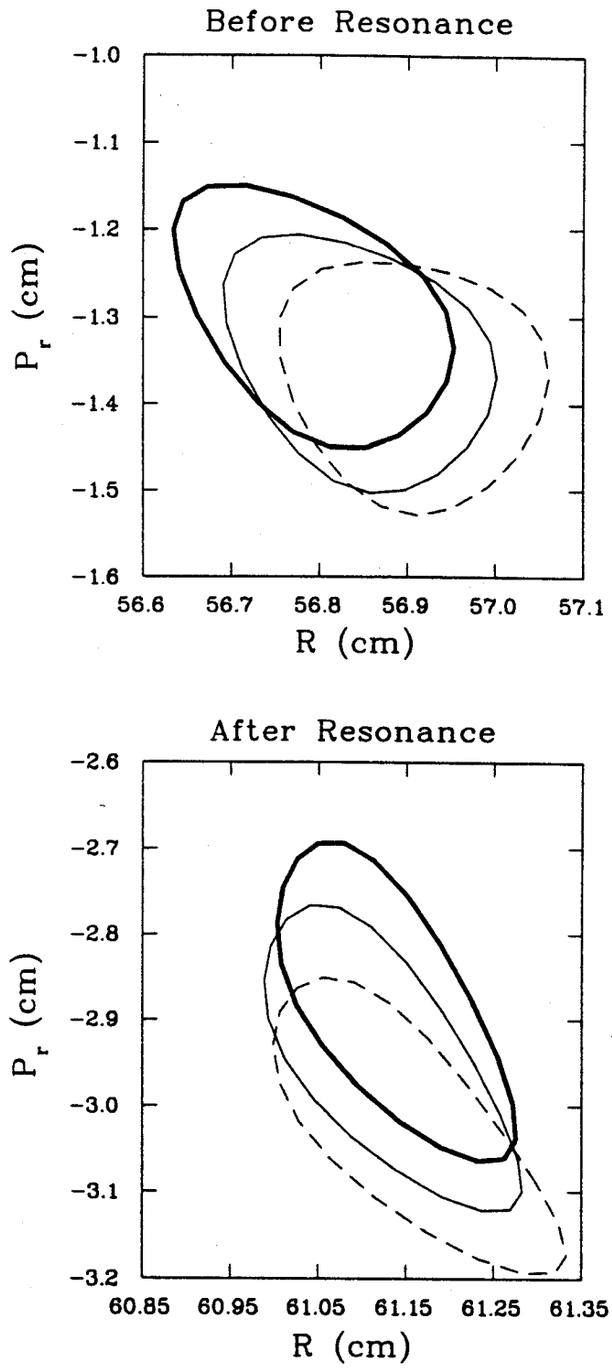

Figure 4.11: Top: The phase space areas just prior to crossing the $\nu_r = 1$ resonance. The spaces were started with 0. (thick), 0.65 (thin), and 1.3 mm (dashed) initial centering errors. There is no apparent distortions caused by precessional mixing. Bottom: The same spaces after crossing the focusing resonance. There is an apparent shape distortion in the 1.3 mm offset space.

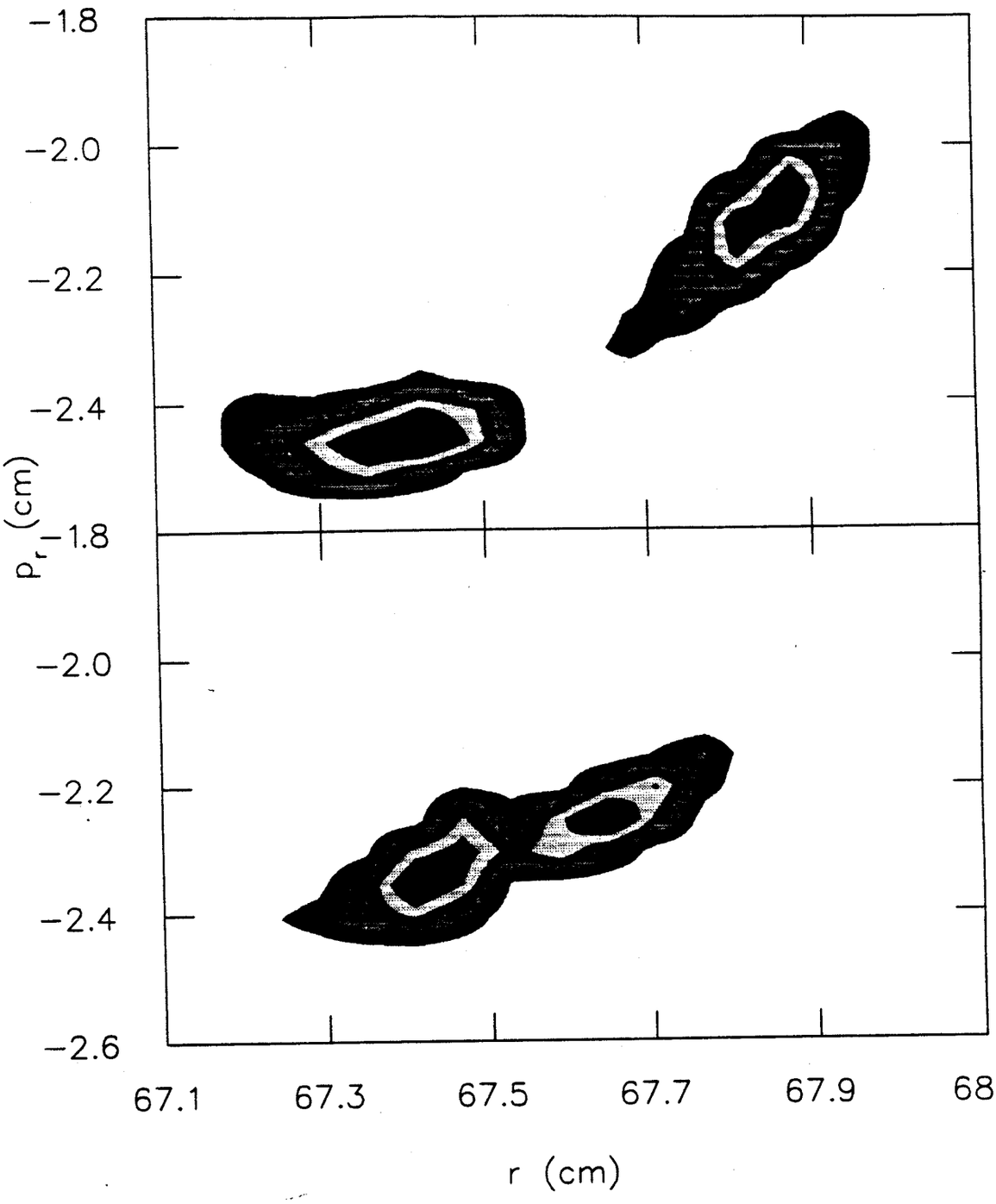

Figure 4.12: The radial phase spaces for the final two turns in the K500. The top are turns run with an extraction bump of 10 gauss while the lower plot is run without. While the size of the two phase spaces are well behaved in both cases, the turn separation is insufficient for optimal extraction without the bump.

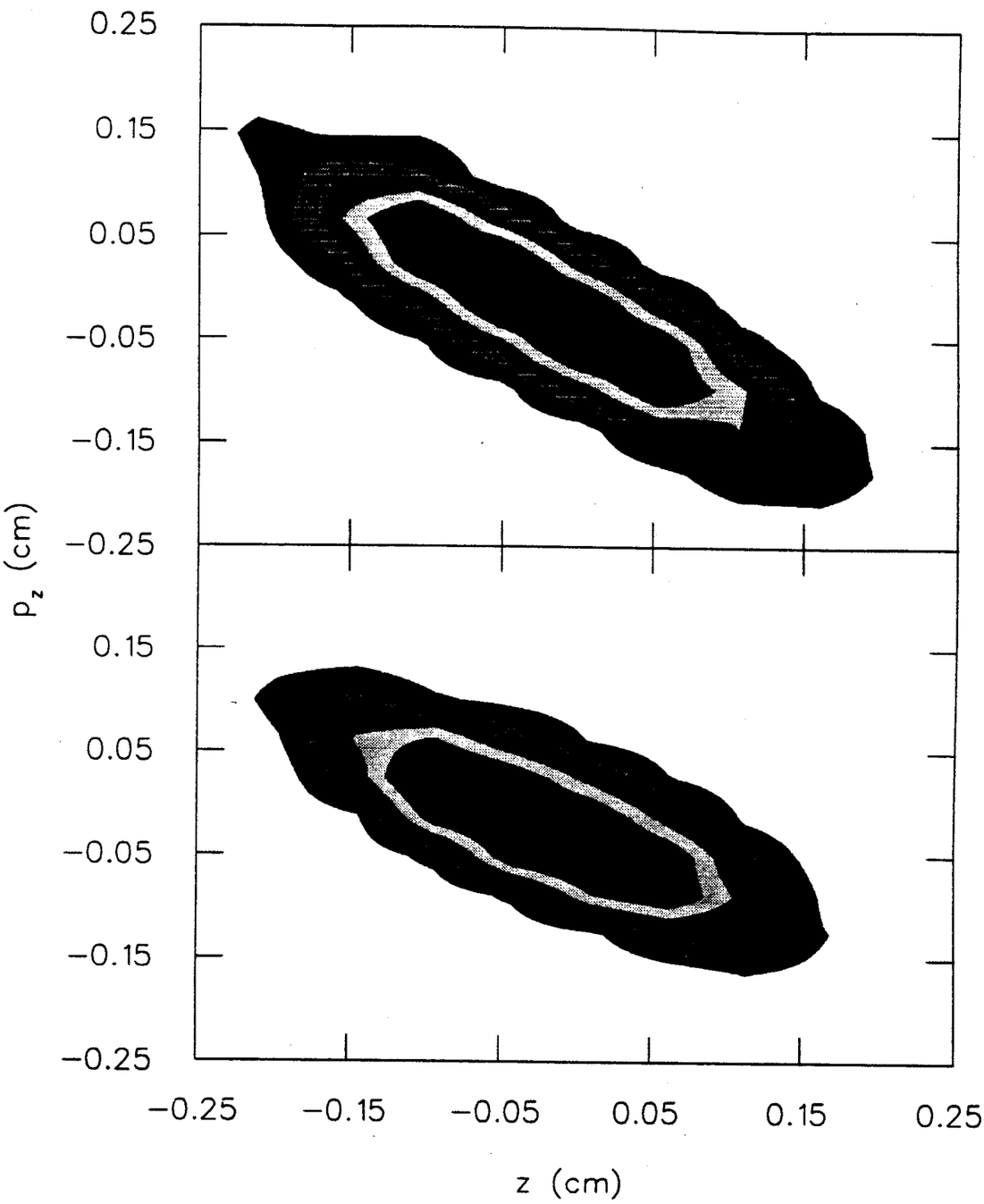

Figure 4.13: The axial phase spaces for the final two turns in the K500 after passing through the final $\nu_r = 1$ focusing resonance in the presence of a first harmonic bump (top) and without (bottom). The two turns in each graph are so similar as to overlap axially (but are, of course, radially separated). Note the small increase in vertical phase space caused by the off-centered passage through $\nu_r = 1$.

Chapter 5

Hardware Construction and Commissioning

With a workable central region design in hand, the new second harmonic central region and inflector were constructed. This new equipment was then installed in the K500 and tested.

Figure 5.1 shows the mechanical design for the new inflector assembly. In the old design the inflector was made small enough to allow both it and its housing to fit through the 4 cm hole in the center plug. This allowed the inflector to be inserted and removed from outside the cyclotron. That design had the added advantage that the vertical position of the inflector electrodes could be adjusted by partially 'removing' the assembly. The disadvantages to such a small inflector are the size of the electrodes (which poses a problem in their fabrication), the limited gap size (which limits the acceptance) and the size of the supports necessary to hold the electrodes in place. The supports in the old design, which fix the electrodes relative to one another and serve as the electrical leads, were structurally weak and thus presented problems in the alignment of the electrodes, both relative to each other and the inflector housing exit. Thus, for the new design, it was decided to enlarge the entire assembly, giving up the ability to remove the inflector from outside the machine. The design now calls for the

inflector and housing to be fixed in the central region, with the voltage leads inserted from outside the machine. This resulted in larger, easier-to-machine electrodes and stronger supporting leads, and a fixed orientation (relative to the central region) of the electrodes and housing.

The proper shapes for the electrode surfaces for calculation purposes were determined from the inflector equations 2.3 of Belmont and Pabot [21]. In order to physically construct these shapes, a similar procedure was used. Analogous to the procedure described in Chapter 2 for creating the RELAX3D input, the shape of the entire inflector surface was created. This time two identical forms were made, each of which would become one of the two final electrodes. Each piece was then fixed to a turntable with the axis of rotation parallel to the vertical axis of the inflector. This axis was then set horizontally and fixed to a milling machine, whose bit comes down from above. Recalling equations 2.3, we can see that the position of the reference particle is fully determined by the dimensionless parameter $0 \leq b \leq \frac{\pi}{2}$, which in turn can be related to a rotation about the inflector's vertical axis by the same angle. This parameter uniquely determines the location and direction of motion of the reference ray. The electrode surfaces, then, must be everywhere parallel to the direction of motion of the reference ray at any particular point. In terms of our now horizontal inflector form, this means that for any position along the axis there exists a turntable rotation which makes the electrode surface perpendicular to both the inflector axis and the machining bit. Given the proper rotation about the turntable axis, the depth of the surface can be calculated. Then, given a series of turntable rotations, a correlated series of depths and axis locations can be calculated, determining the shape of either inflector surface. A short program was written to do just that, and for a sequence of rotations the depth of the inflector surface was calculated. A 6 mm diameter ball-end mill was then brought down in vertical steps of 0.06 cm removing material until the

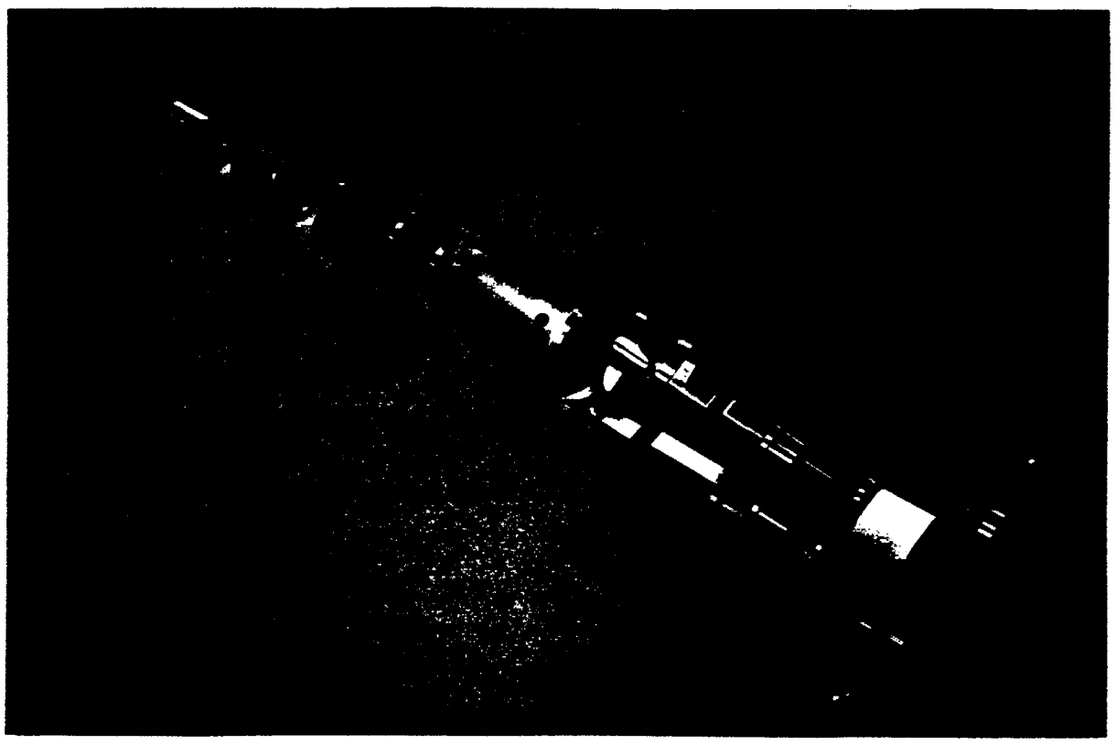

Figure 5.1: The K500 spiral inflector assembly. The electrodes can be seen in the center of the photo. The entire assembled structure is $\sim$ 20 cm in length.

final depth was reached. The bit was then retracted, the turntable rotated by hand and the process repeated for the next depth. The entire angular range was repeated twice, once with 4° steps and then again with a rotation step of 2°. Each inflector electrode was thus carved out of the two identical forms.

The electrodes were initially to be made from stainless steel. However, the material proved difficult to machine and was replaced by aluminum. The support leads for the inflector electrodes were of copper as was the inflector housing. The picture in figure 5.1 shows the entire inflector assembly.

The final mechanical design for the central region dee tips is shown in figure 5.2. Two of the tips were each made from a solid block of copper while the interior channel of the puller tip was first milled, and then the outer wall soldered into place. Figure 5.3

shows the central region dee tips and hill posts as they will be in the cyclotron.

Once constructed, the new inflector and central region were installed. The positioning of the inflector assembly is accomplished by use of a jig which is fixed to the hill tips of the center plug and properly aligns the inflector. The new central region was then conditioned and to date holds voltages up to 60 kV. The full 70 kV needed for full operation has not yet been tested. Initially the inflector would not hold full voltage. After fixing a problem in the voltage leads which caused sparking, it was determined that an additional ceramic insulator was needed at the connection between the voltage leads and the inflector assembly. Once this additional insulation was added, the inflector held voltage up to the full 12 kV necessary.

The first turn slit is designed to slide over a 3 mm range and to be secured in position. To properly position the slit the cyclotron was run with the slit removed and a differential probe trace was taken across the first 18 cm. This trace was then used to determine the computer model dee voltages necessary to match the machine performance (see Chapter 6). The computer model was then used to determine the position of the slit.

Since all of the positioning of the central region dee tips was done with the K500 cap raised, there was some concern about motion of the dees when the cap was closed and the dee stem seals tightened. To determine the amount (if any) of motion caused by the machine closing process, a CCD TV camera was used to watch and record any such motion. The camera was placed atop the K500 cap looking down the magnet axis through the center yoke hole where the inflector electrode leads would normally sit. The dee tips were replaced by a set of labeled dummy tips each of which had a set of two reference holes drilled in them. The inflector was removed and in its place was set a jig with posts identifying the machine center and three additional posts

at known distances representing the center of each hill. The hill and center posts provided fixed reference points while the dee tip replacements were free to move. The image from the CCD was directed to a frame grabber and a set of images stored. These conditions were with the cap raised, with the cap lowered and then with the cap lowered and the dee stems secured. The digitized images were then analyzed by a separate program which graphically displays the pixel information and allows the user to interactively find the pixel values of any point. By using the distances between the fixed center and hill posts to set the scale the cartesian coordinates of each of the replacement dee holes could be obtained. Figure 5.4 shows the initial and final cartesian coordinates of the various reference posts and dee holes obtained from the digitized CCD image. There is little movement of dees B and C after the dee stem collars are tightened. The A dee however, shows a 2 mm shift in position once the collars are in place. This is in addition to any further motion caused by the RF heating of the dees while the machine is running. This motion may cause some problems in matching the tuning of the machine to the parameters suggested by the computer runs, and should be corrected during the future redesign of the dee stems.

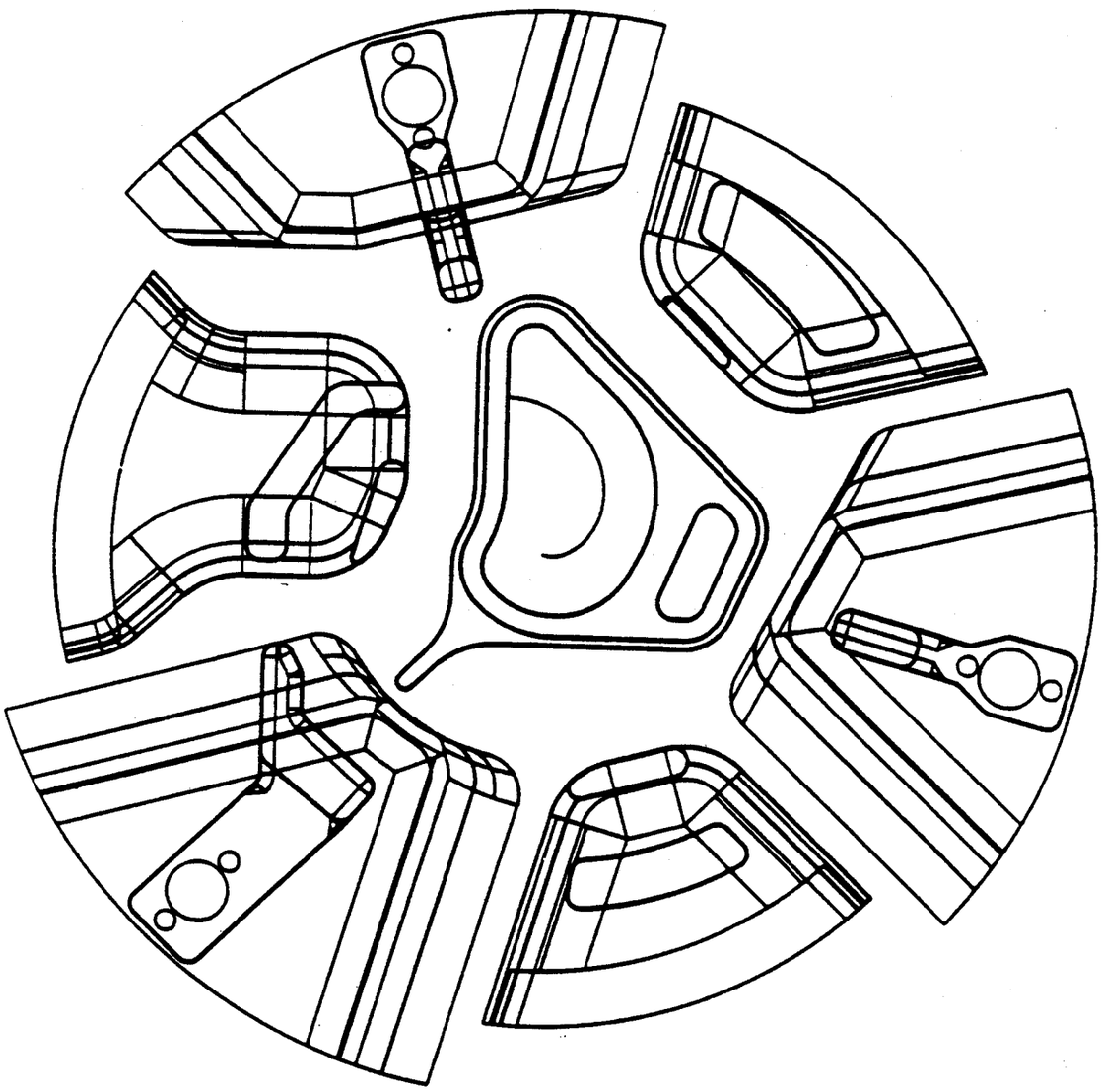

Figure 5.2: The mechanical design for the 2^{nd} harmonic central region. Shown are the dee tips, hill posts, inflector housing and first turn slit.

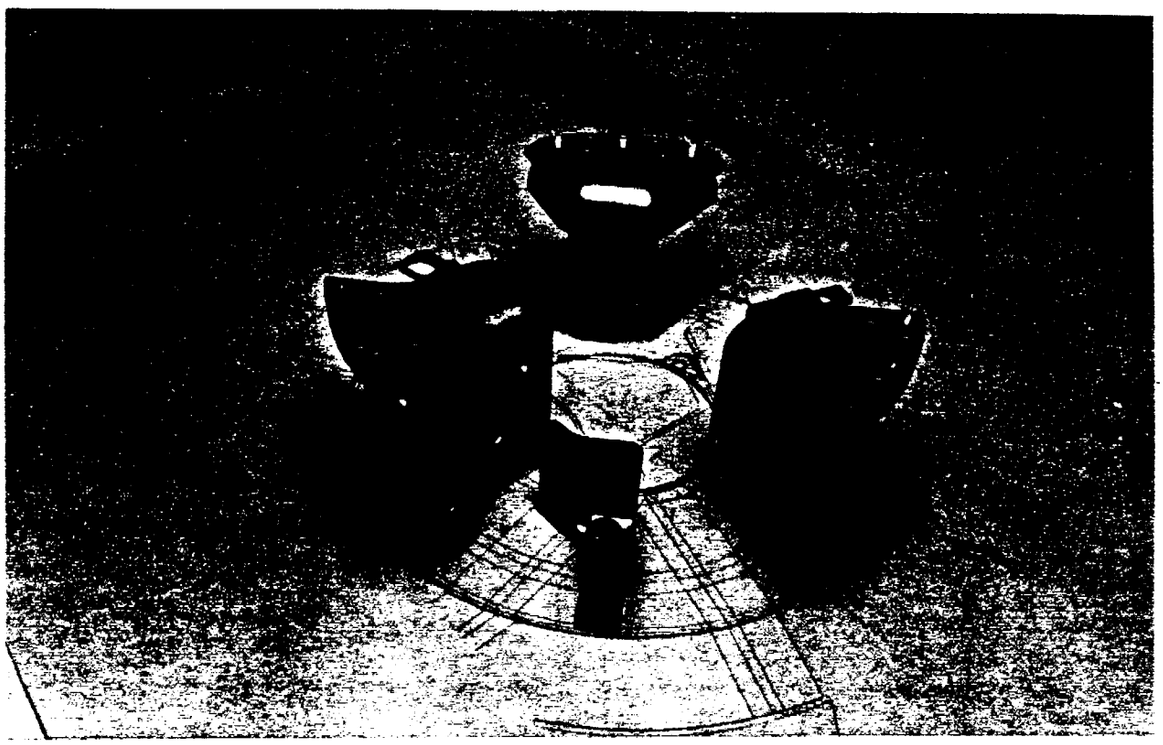

Figure 5.3: The central region dee tips and hill posts. The structures consist of 3 dee tips and three hill posts, one of which acts as a first-turn slit. The dee tip at the left is the puller while the post just above it is the first turn slit. The height of the dee tips is $\sim$ 2 cm.

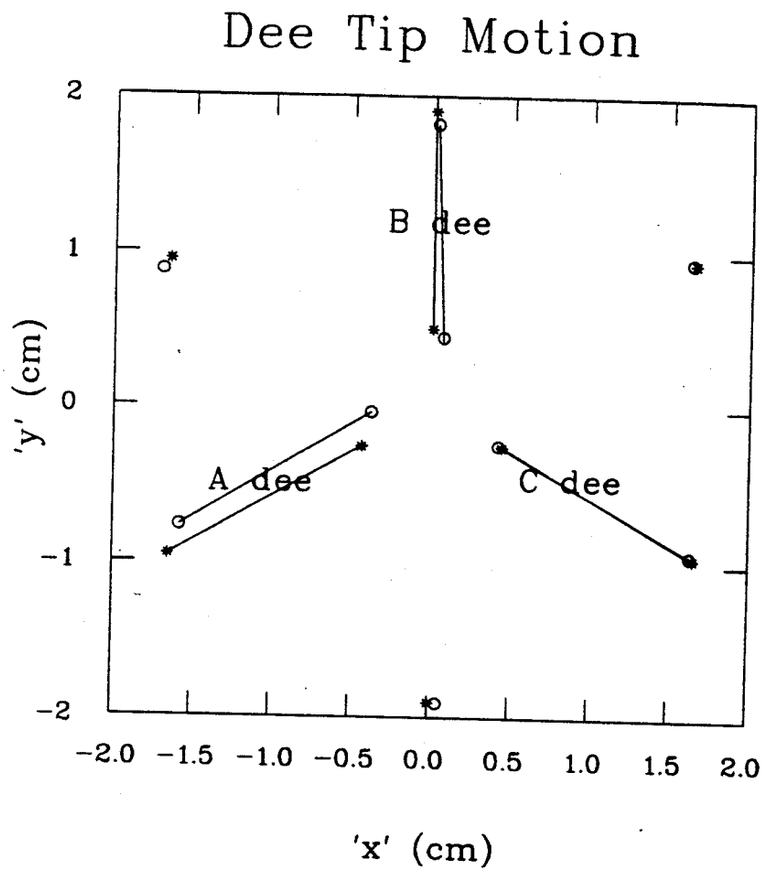

Figure 5.4: The position of the test dee tips before and after the K500 cap has been closed and the dee stem collars tightened. The asterisks mark the initial positions while the circles denote the final location of the reference holes. The points joined by lines represent the moveable dee tip holes while the others mark the location of the fixed hill posts. The small motion in the fixed positions is an artifact of the digitization and the change for view of the CCD camera between its cap up and cap down positions.

Chapter 6

Operation and Experimental Results

6.1 Beam Diagnostics

The K500 cyclotron is equipped with several diagnostic tools. The two devices most important to this study are the main probe and the internal timing detector.

The K500 main probe consists of a train of 20 carts which move along a track set in the center of the 0° hill (see figure 6.1). At the end of these carts, sits the probe head which is made up of an intercepting block (main probe). Attached to this is a 0.75 mm thick tungsten wire which precedes the main block radially inward. With this probe, current traces can be obtained between 7.5 cm and the extraction radius (66 cm). Additionally, the differential wire can be used to see turns in any region in which the turns are separated. Signal wires and water cooling run through the interior of the carts. The entire assembly is driven by a motor external to the cyclotron and the position of the probe determined via a calibration to an optical encoder located on the motor. Since there is some play between successive carts, the calibration can be done for either the condition where the probe is moving out or moving in. For all the following studies the probe has been calibrated moving out. The probe calibration is preset in the monitor system and to ensure proper values

were obtained, a set of measurements of probe position versus monitored position were made. Figure 6.2 shows the correction to the monitored position obtained for the first 20 cm.

To determine the timing spectrum of the internal beam, a timing probe was used. This probe is inserted through the opening of the M4 magnetic element which had been removed. The range in which the probe can move is limited by how close it comes to the B dee, and can be used only in the range of 58 – 66 cm. This is sufficient as the timing properties of the beam are most important at extraction. The probe itself has two versions. One consists of a 1.5 m steel tube which is inserted into the beam path. The gamma rays generated by beam collisions with the tube are picked up by an avalanche diode sitting just inside. To improve cooling to the detector, a 6 mm diameter water carrying copper pipe was inserted into the tube in contact with the diode assembly. The second detector is a Si PIN diode which directly intercepts the beam. This is the same type used for earlier timing studies in the K1200 [19].

In addition to to the timing and main probes, there are several other diagnostic tools available. The inflector voltage can be turned off and the beam current which then strikes it can be measured. This is referred to hereafter as the inflector monitor mode. There exists a viewer probe which consists of a square of scintillating material mounted at the end of an optical system. The scintillator is inserted into the beam chamber and the image of the beam on the material is carried to a CCD camera located outside the cyclotron. With this probe, the vertical and radial centering can be determined. Finally, there are several Faraday cups located along the ECR-K500 beam line and after the K500 extraction. Using these and the current probes mentioned before, a measure of the beam transmission can be obtained all the way from the ECR to the K500 extraction.

6.2 Experimental Results

The new second harmonic central region and inflector were first installed in Marcl of 1995. Commissioning began soon thereafter using a 15.5 MeV/u O^{+4} beam fron the SCECR (the Superconducting Electron Cyclotron Resonance ion source) with ar injection voltage of 20 kV. The dee voltage used was 48 kV with a frequency of 25.(MHz. This beam was used for all the following measurements.

6.2.1 Placement of the First Turn Slit

Before any studies of the performance of the central region design could be performed the first turn phase selection slit needed to be properly positioned. In order to de termine this, the K500 was run with the first turn slit removed. The SCECR-K50(beam line, inflector voltage and dee voltages were tuned to give maximum trans mission out to 18 cm. A differential probe trace was then taken to determine the locations of the turns between 7.5 and 18 cm. These positions were then compare(to the calculated values predicted by the Z3CYCLONE orbit code. Figure 6.3 shows the turn trace and a comparison with the location of the central ray for three dee voltages, V_{dee} = 46 kV, 48 kV, and 50 kV. The agreement between the two is poor at best and would suggest that the orbit code does not model the behavior of the beam well in this region. One reason for this may be the motion of the dee tips mentioned in Chapter 4. However, if one considers the beam as being made up of a range o central rays (and their surrounding phase spaces) a better agreement can be reached Figure 6.4 shows the calculated radial positions (at the main probe) for central rays with starting times in the range of τ_0=190-250°. It is evident from this picture that the peak current shifts in starting time with respect to turn number. Thus, looking at the location of peak currents for the full range of starting times τ_0 we can match

the calculated turn positions with the measured differential trace (see figure 6.4). It should be noted that the best fit (figure 6.4) occurs when a dee voltage of 50 kV is used in the orbit calculations. This 4% change in voltage can be attributed to both an error in the K500 dee control calibration and the increased clearance of the dee tips afforded by running at a higher voltage.

Once the Z3CYCLONE parameters were set to give good agreement with experiment in predicting the location of the turns in the K500, these parameters were used to determine the location of the first turn slit. Figure 6.5 shows the first turn beam path predicted by the orbit calculations for a range of starting times. Using this model, the location of the first turn slit was chosen so as to center the aperture around the central τ_0=210° ray. This resulted in the slit center being positioned at $r = 3.96$ cm. with t his position determined, the K500 was vented and the slit placed accordingly.

6.2.2 Operation with the First Turn Slit

With the first turn slit inserted, the O^{+4} test beam was again run. Table 6.1 shows the relevant operational parameters used for the run. Using the first harmonic centering bump, a radially well-behaved beam was obtained. Figure 6.6 shows the differential probe trace from 7.5 cm to extraction. Individual turns that are clearly seen in the first 23 cm, are lost completely from 23 cm to 32 cm and then return (though not completely separated) for the remainder of the machine radii. The appearance of defined turns out at 65 cm can be attributed to the first turn slit's phase limiting of the beam as well as the added turn separation expected by the change to second harmonic RF. To truly see the effect of the first turn slit we can compare the probe trace above to that found in figure 6.7 which was taken without the first turn slit. Clearly the addition of the slit significantly increases the turn definition.

Table 6.1: K500 Operating Values for 15 MeV/u O^{+4}

I_{coil1}	498.8A	V_{inf_anode}	4.63kV
I_{coil2}	341.4A	$V_{inf_cathode}$	-4.60kV
V_{Adee}=V_{Cdee}	46kV	B_{cntbmp}	40.5 gauss
V_{Bdee}	47kV	ϕ_{cntbmp}	300°

If we examine the first 1.5 cm of the probe trace (figure 6.6) we see the appearance of 'satellite' peaks around the main turn peaks. These may be the result of highly off-centered or off-phase segments of the injected beam, which pass around the slit, or they may be contributions from the phase spaces of similarly off-phase rays which pass through the slit aperture. Either way they vanish within the first 7 turns, a signature of greatly off-centered beam components.

Of more curious origin is the complete loss of turn separation in the $r = 23$ to 32 cm range. Since the turn separation reappears, we need to consider what mechanism will cause the overlap in this region alone. As discussed in Chapter 3, a phase-dependent centering error occurs in the beam during the first turn. This phase dependent centering error will cause an oscillation in the radial width of the beam. This oscillation is enhanced by the radial spread induced by the phase curve (equation 1.14). While this is advantageous with respect to phase selection, it causes a large additional energy and radial spread in the beam. This spreading of the radial beam width will cause a reduction in turn separation, and if severe enough could account for the complete loss seen on the differential probe trace. If we look along the probe path this phase induced spread peaks at around 30 cm, coinciding with the $\sin(\phi)$ going through zero. As the beam progress past this location, the phase swings positive and the energy spread is reduced. There still exists a phase dependent centering error but the longer the beam phase stays positive the smaller

the oscillation of the envelope becomes. This effect can be seen in figure 6.8, which shows the calculated radial spread, along the main beam probe track, for a set of central rays with starting times ranging from τ_0=200-220° and the energy spread for the same. We see from the figure a peak in the radial beam spread in the range of 23 to 35 cm, the same range in which the differential probe trace sees a loss of beam separation. We should therefore be able to reclaim separated turns in this region by further limiting the phase width of the beam.

6.2.3 Phase Selecting Pins

The first turn slit is not sufficient to reduce the phase width to the 3° FWHM required by the coupled cyclotron project. Thus, the two phase pins located at $r = 18$ cm are used to further limit the time spread of the beam. With the first turn slit in position and the K500 tuned to radially center the O^{+4} test beam for maximum transmission, the phase pins were inserted. The phase pins are 0.32 cm diameter tungsten wires mounted off-center of a rotating shaft. The pins may be rotated 360° by the drives resulting in a 1.27 cm radial motion. To determine the optimum positions for the two pins, a single pin was first inserted into the beam path. The pin was then rotated to a position which maximized the current out at 25 cm. The second pin was then inserted and rotated until, again, the current was maximized. In this manner the pins were positioned such that they intercepted the least amount of beam possible. At this point, the internal timing probe was moved into position ($r \approx 60$ cm) and a measurement of the phase width of the beam was made. The pins were then rotated, one at a time, and additional timing measurements made. A minimum phase width was obtained of 4.5° FWHM. With the pins so positioned, a differential probe trace was taken and the currents along the radial length of the K500 recorded.

The differential probe trace obtained with the first turn slit in place as well as both

Table 6.2: Transmission through the K500

1^{st} Harmonic	Buncher Off		Buncher On	
Location	Current	Transmission	Current	Transmission
Inflector	1.7eμA		1.7eμA	
FT Slit (r=15 cm)	72 enA	4.2%	360 enA	21.2%
Phase Pins (r=20 cm)	26 enA	1.5%	135 enA	7.9%

phase pins (adjusted to give minimum phase width at 60 cm) is shown in figure 6.9. Individual turns are clearly visible throughout the machine including the 23 to 32 cm range. Examination of the turn pattern out beyond $r = 40$ cm shows little turn bunching, which indicates a radially well-centered beam.

6.2.4 Phase Selection and Transmission

In order to determine the transmission properties and phase selection abilities of the K500 system, current levels and timing measurements were made for a variety of conditions. The internal timing probe was used to make measurements of the beam phase width for the K500 run with no phase selection, with the first turn slit only and with both the first turn slit and phase pins. Figure 6.10 shows the timing spectra for these three cases. Clearly, we can achieve the narrow peak required by the coupled cyclotron project. Table 6.2 shows the transmission percentages through the K500 for the various buncher and phase selection settings (the second harmonic buncher was, at the time of the measurements, inoperative). The transmission values obtained agree with those predicted by the orbit code calculations, as do the phase widths.

It should be noted that the transmission values given are for a final phase width of 5° FWHM with no second harmonic buncher. We expect a further factor of two increase in transmission from the addition of the second harmonic buncher, and a factor of two reduction when the phase width is further reduced.

6.3 Summary

An axial injection and central region system have been designed and constructed that meet the operating requirements for the K500⊗K1200 coupling project. The spiral inflector has been redesigned to account for the new scaling law, and a second harmonic central region has been devised. Computer calculations of the vertical focusing and radial centering properties of this central region have been performed, the results of which show good performance in both respects.

Calculations of the overall behavior of the axial injection and central region system show the production of a well-behaved beam. The centering error for the simulated beam is minimal as full energy is reached without the phase space distortions which accompany a miss-centered beam. In the simulations, the phase width has been reduced to 3° FWHM, and with the use of both the first and second harmonic bunchers, 6% of the input DC beam reaches full energy. The second harmonic buncher should give a factor of 2 increase in the transmitted beams and should certainly be used in the final system. The extraction bump, in conjunction with the final phase-reduced beam, produced good turn separation at extraction and a 2.2π mm-mrad emittance.

The above mentioned designs have been built and installed in the K500 cyclotron. During initial operations with the new inflector and central region, beam has been successfully accelerated up to full energy and extracted. The beam has been successfully centered through the use of the first harmonic bump coils. Comparisons of the calculated turn positions versus the observed values (using the main probe) show good agreement when a full range of starting times is used. The operating and calculated dee voltages needed to get such agreement differ and at this point it is not clear whether this is due to an uncertainty in the voltage calibration of the K500 monitoring system, a variation between the actual and assumed starting conditions,

or motion of the dee tips. Certainly, the dee tip motion will present a problem an as such should be addressed during the K500 upgrades.

The first turn slit has been placed according to computer simulations, and th phase-reduced beam produced has been accelerated to extraction. Observations c the enhancement of the turn separation caused by the slit have been made as wer internal timing measurements of the beam. The introduction of the phase pins allowe a further reduction in the phase spread of the beam thereby producing separated turn throughout the machine. In this way, the measured phase spread of the beam ha been reduced to 2.5° FWHM. Transmission calculations on a 5° FWHM beam hav shown that the first harmonic buncher increases the current by a factor of five an places nearly 8% of the input current into the reduced width. The instability of th RF system and the lack of a working second harmonic buncher limited the testing o the design.

Improvements to the RF supplies and mechanical systems need to be made t increase the stability of the machine and to limit the motion of the dee tips. Addi tionally it was found that tuning for maximum current through the first turn slit wa not always compatible with a vertically centered beam. By using a moveable firs turn slit, it may be possible to achieve both of these objectives.

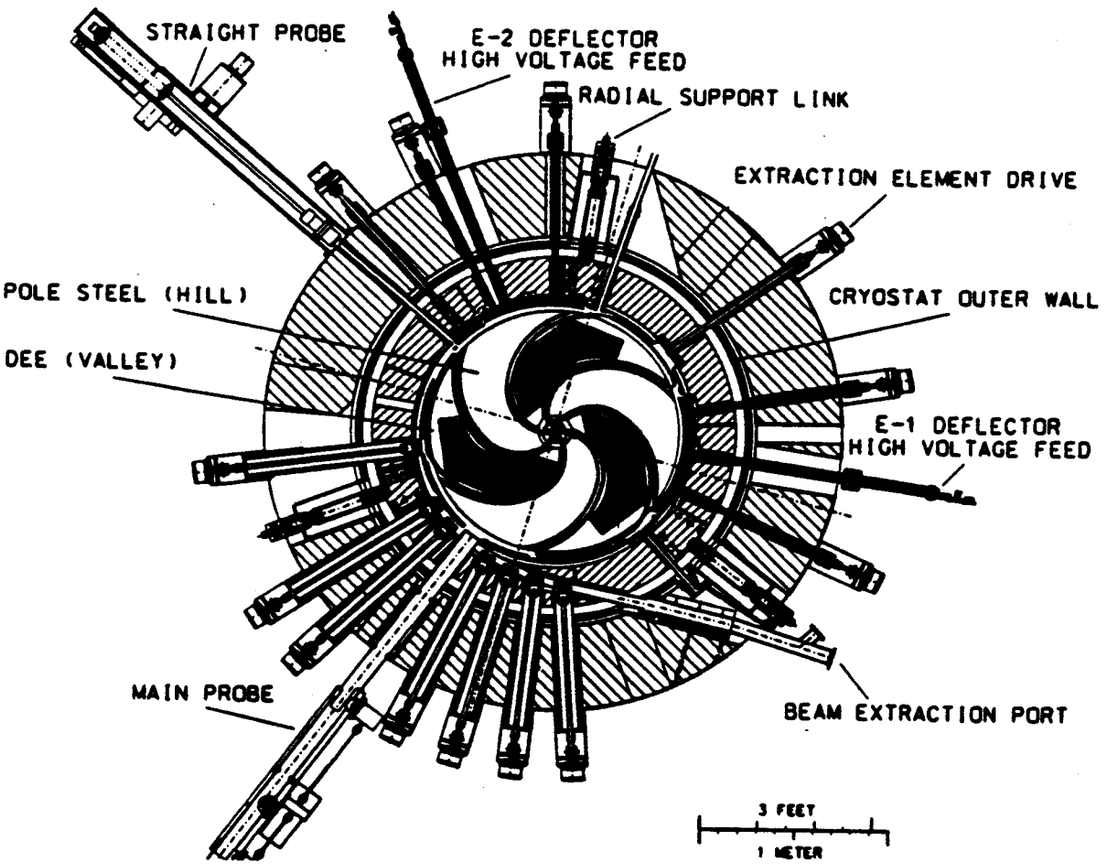

Figure 6.1: The K500 cyclotron top view showing the various beam diagnostic probes.

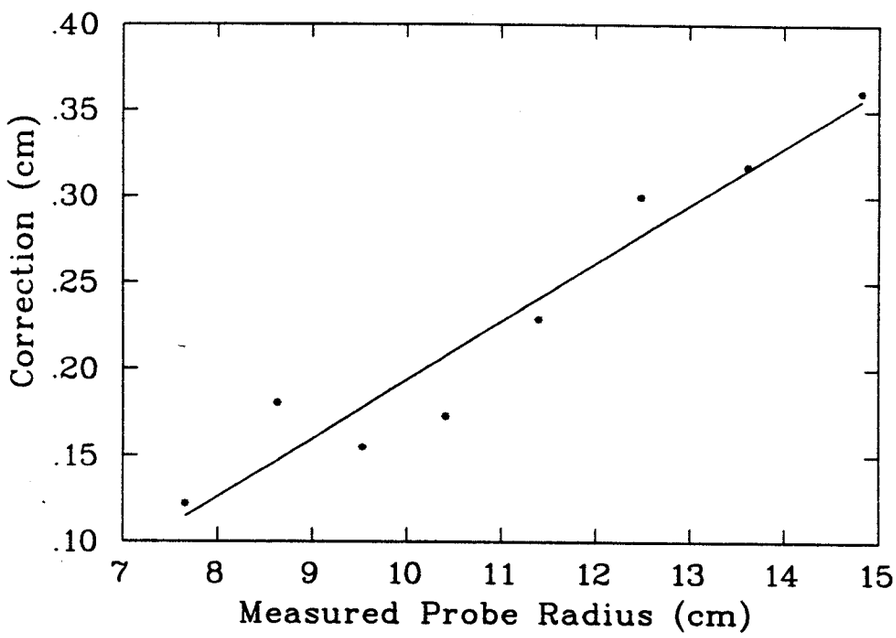

Figure 6.2: Main probe calibration corrections for the first 10 cm in the K500.

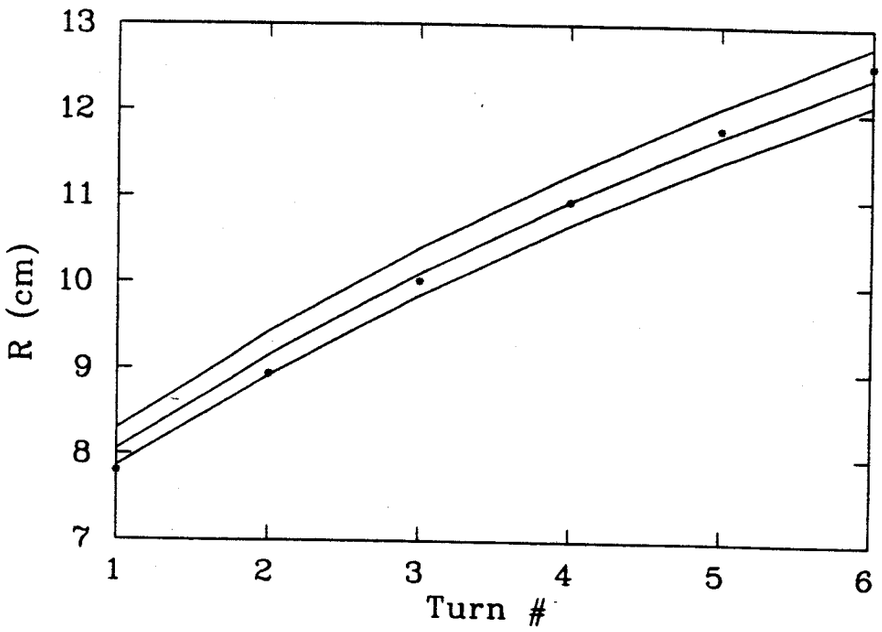

Figure 6.3: Comparison between Z3CYCLONE and the differential probe trace for $r = 7$ to 13 cm. The radial position vs. turn is shown along the path of the main probe. The lines are the values predicted by orbit code calculations for voltages of (top to bottom) 50 kV, 48 kV, and 46 kV, while the points are measured values.

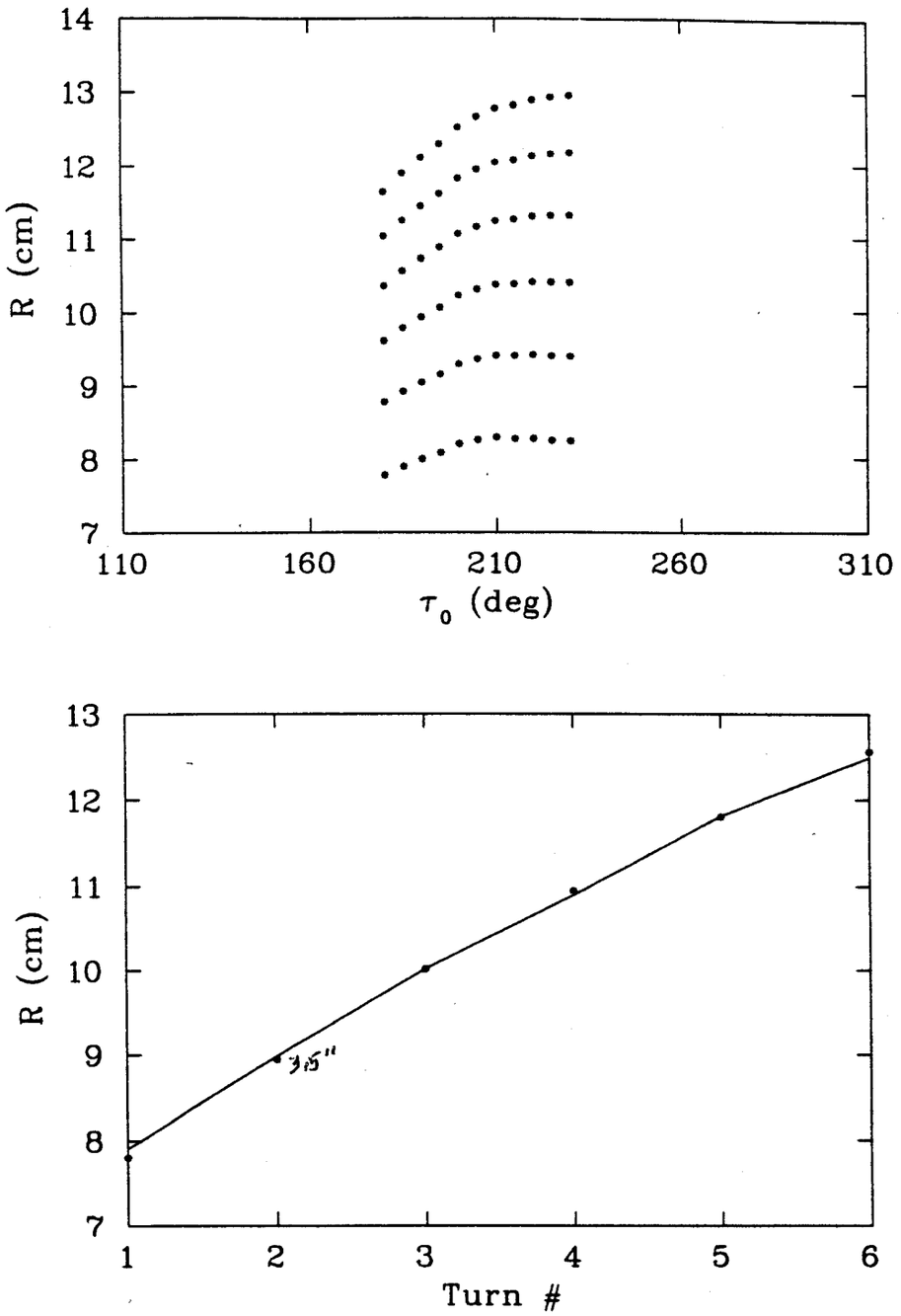

Figure 6.4: Top: Calculated radial position (for several turns) vs. starting time for rays with τ_0=190-250°. The radial density can be seen to shift in τ_0 with turn number. Bottom: A comparison of radial 'peak current' between the calculated values from the top graph and the probe trace. The line represents the calculated peaks while the points are the measured locations.

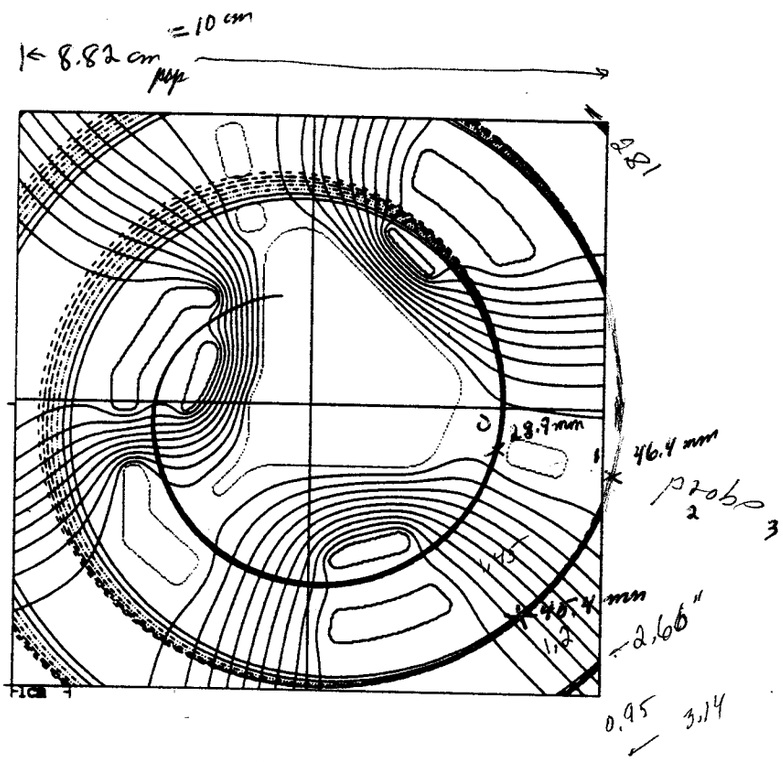

Figure 6.5: The central region design showing central rays with starting times between τ=190° and 230° in 5° steps. The location of the turns in this diagram were used to determine the location for the first turn slit.

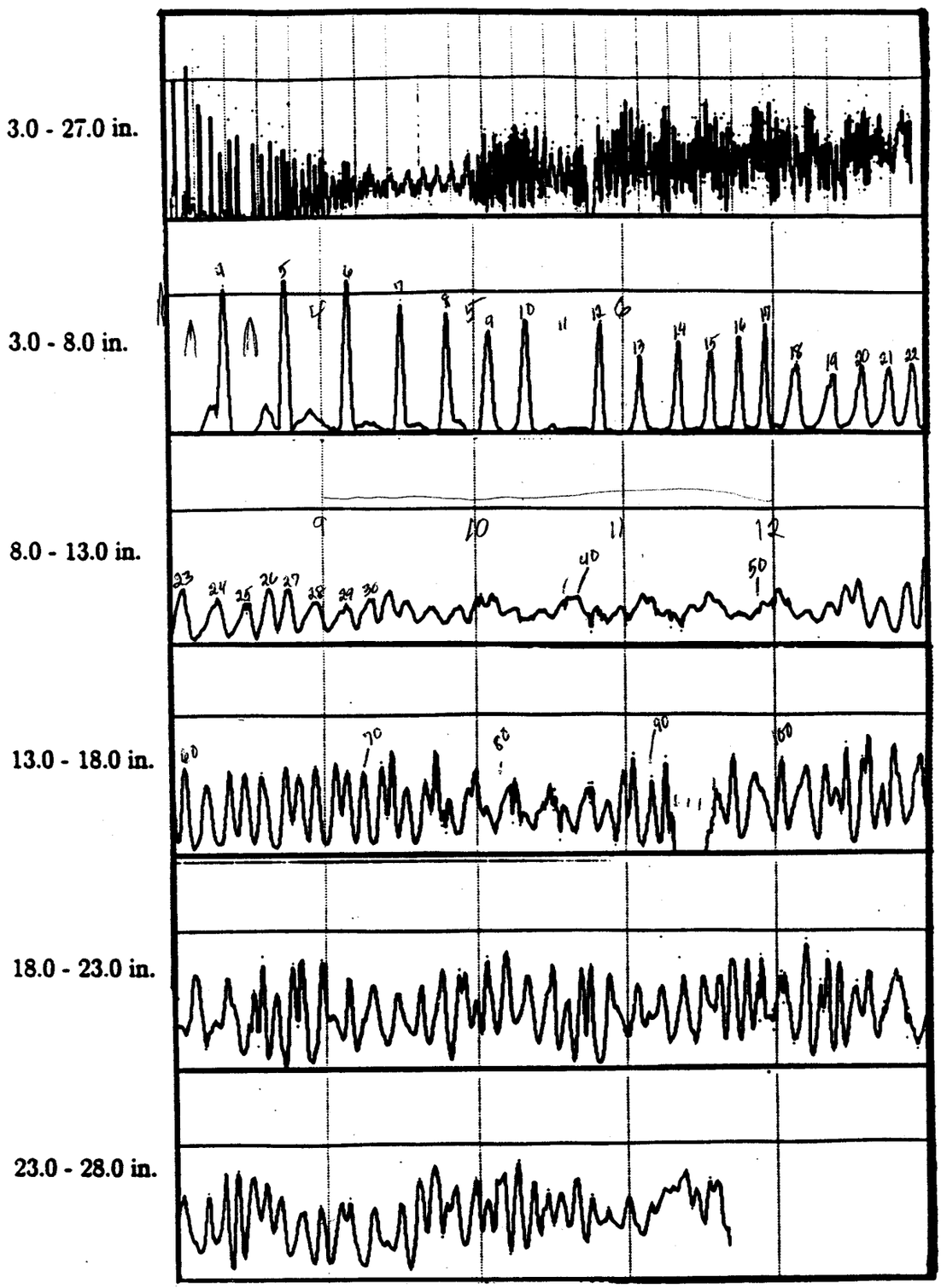

Figure 6.6: Differential probe trace for K500 15 MeV/u O^{+4} beam with the first turn slit in position. Individual turns are visible throughout the machine with the exception of $r = 23$ to 32 cm.

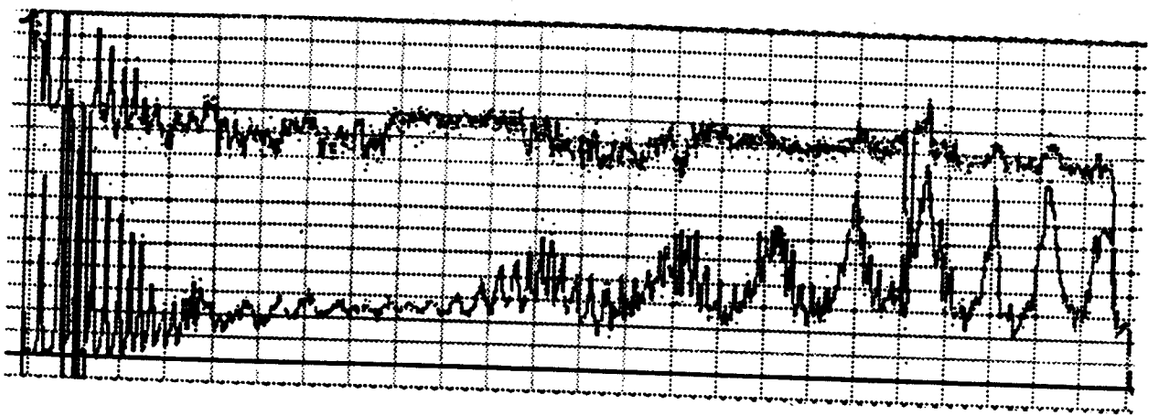

Figure 6.7: Differential probe trace for the K500 15 MeV/u O^{+4} beam without the first turn slit. Individual turns are visible for only the first 18 cm.

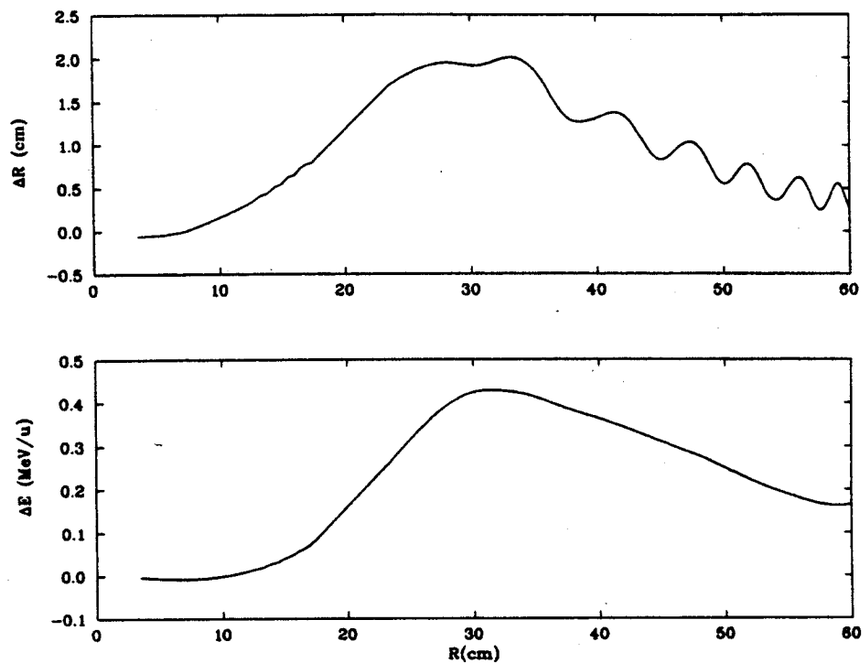

Figure 6.8: Calculated radial width vs. radius (solid line) along the main probe track for a beam consisting of central rays with starting times τ_0=190-230°. The beam width peaks at $\sim$ 30 cm and then declines corresponding to the loss of turn definition on the main probe trace. Also shown is the energy spread for the same rays vs. radius.

fig. 6.9 ?

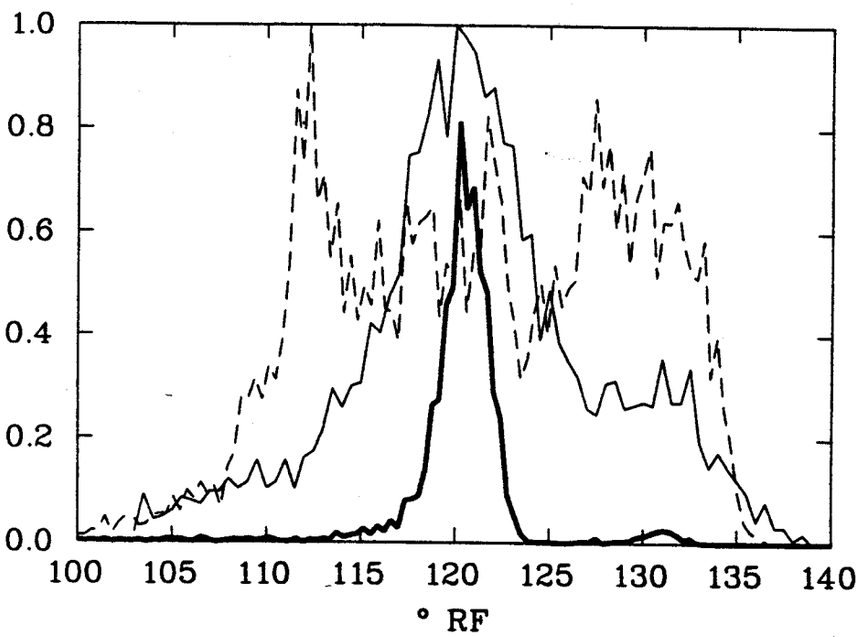

Figure 6.10: Internal timing probe measurements for three cases, no phase selection, first turn slit only, and first turn slit plus phase pins. Total widths of 25° (dashed), 12° (solid), and 3° (double thick) FWHM respectively are obtained.

Bibliography

[1] P.S. Miller, Proc. 10th Int. Cycl. Conf. E. Lansing, USA, (1984) 11.

[2] J.A. Nolen et al., Proc. 12th Int. Cycl. Conf. Berlin, (1989) 5.

[3] R.C. York et al., "The K500⊗K1200, A Coupled Cyclotron Facility", NSCL, E. Lansing, 1994.

[4] R.C. York et al., "Proposed Upgrade of the NSCL", 1995 Part. Accel. Conf., Dallas, 1995.

[5] M.M. Gordon, Effects of Spiral Electric Gaps in Superconducting Cyclotrons, Nucl. Inst. and Meths. **169**, (1980) 327.

[6] M.M. Gordon, "Single Turn Extraction", IEEE Trans. on Nucl. Sci., **NS-13**, (1966) 48.

[7] J.C. Collins, PhD thesis, Michigan State University, 1973.

[8] H.G. Blosser, "Problems and Performance in the Cyclotron Central Region", IEEE Trans. on Nucl.Sci., **NS-13**, (1966) 1.

[9] H.G. Blosser, Proc. 5th Int. Cycl. Conf. (Oxford 1969), 275.

[10] B.F. Milton. *Phase Selection in the K500 Cyclotron and the Developement of a Non-Linear Transfer Matrix Program.* PhD thesis, Michigan State Universtiy, 1986.

[11] L. Smith and A.A. Garren, Orbit Dynamics in the Spiral-ridged Cyclotron, Lawrence Rad. Lab., Berkely Calif., (1959).

[12] N.F. Verster and H.L. Hagedoorn, Orbits in an AVF Cyclotron, Proc. Int. Conf. on Sector-Focused Cycl., Los Angeles, CA, (1962) 201.

[13] L. J. Laslett and K.R. Symon, CERN Symposium on High-Energy Accelerators, (1959) 38.

[14] L.J. Laslett and S.J. Wolfson, MURA-497, Midwest Univ. Res. Assn., Madison, Wisc. (1959).

[15] M.M. Gordon and W. S. Hudec, Effects of Field Imperfections on Radial Stability in a Three-Sector Cyclotron, Nucl. Inst. and Meth. **18,19**, (1962) 243.

[16] M. Reiser, Central Orbit program for a Variable Energy Multi -particle Cyclotron, Nucl. Inst. and Meth **18,19**, (1962) 370.

[17] F. Marti and A. Gavalya. Axial injection in the K500 superconduction cyclotron. In *Proc. 11th Intl. Conf. on Cyclotrons and Their Applications.*

[18] F. Marti, J. Griffin and V. Taivassalo, IEEE Trans. on Nuc. Sci., **NS-32**, (1985) 2450.

[19] J.D. Bailey. *Phase Selection and Extraction Studies in a Superconduction Cyclotron.* PhD thesis, Michigan State University, 1994.

[20] R.W. Muller, Novel Inflectors for Cyclic Accelerators, Nucl. Instr. and Methods 54 (1967), 29.

[21] J.L. Belmont and J.L. Pabot, Proc. 6th Int. Cycl. Conf. Gatlinburg, USA, (1966) 191.

[22] W.B. Powell et al., Nucl. Instr. and Meth. **32**, (1965) 325.

[23] G. Bellomo et al., On the Feasibility of Axial Injection in Superconducting Cyclotrons, Nucl. Instr. and Meth. **206**, (1983) 19.

[24] F. Marti, Orbit Studies for Ion Inflectors Used in Cyclotrons, Part. Accel. Conf., (1987), 1287.

[25] L.W. Root, Design of an Inflector for the TRIUMF Cyclotron, PhD Thesis, Univ. of British Columbia, (1972).

[26] R. Baartman, The Spiral Inflector: Three Analytical Representation, TRI-DN-90-323, TRIUMF (1991).

[27] R. Baartman and W. Kleeven, A Canonical Treatment of the Spiral Inflector for Cyclotrons, Particle Accelerators 41, (1993) 41.

[28] W. Kleeven and R. Baartman, Beam Matching and Emittance Growth Resulting from Spiral Inflectors for Cyclotrons, Part. Accel. 41, (1993) 55.

[29] M.P. Dehnel, The Developement of an Injection System for a Compact H^- Cyclotron, The Concomitant Measurement of Injected Beam Properties and the Experimental Characterization of the Spiral Inflector, PhD Thesis (and such a thesis it is), Univ. of British Columbia, (1995).

[30] K.L. Brown et al., TRANSPORT, A Computer Program for Designing Charged Particle Beam Transport Systems, SLAC 91 (1973).

[31] F. Marti, J. Griffin, and V. Taivassalo. Design of the axial injection system for the NSCL cyclotrons. *IEEE Transiaction on Nuclear Science*, NS-32:2450-2452, 1985.

[32] A.M. Winslow.. Numerical solution of the quasilinear poisson equation in a nonuniform triangular mesh. *Journal of Computational Physics*, 2:149-172, 1967.

[33] Computer program POISSON. Technical Report LA-UR-87-126.9, Los Alamos National Lab.

[34] P.W. Hawkes and E. Kasper, Principles of Electron Optics, Vol. 1, Academic Press (1989) 74.

[35] A.J. Lichtenberg, Phase-Space Dynamics of Particles, John Wiley and Sons, Inc. (1969).

[36] H. Houtman and C. Kost, Proc. of the Europhysics Conference, Co Accelerator Design and Operation (Springer Verlag, Lect. Notes in Physics 215, Berlin, 1983) pp. 93-103.

[37] J.D. Jackson, Classical Electrodynamics, John Wiley and Sons , (1975) 590.

[38] F. Marti, M.M. Gordon, M.B. Chen, C. Salgado, T. Antaya, and E. Liukkonen. Design calculations for the central region of the NSCL 500 MeV superconducting cyclotron. In *Proc. 9th Intl. Conf. on Cyclotrons and Their Applications*, pages 465-468, Caen, France, 1981.

[39] W.I.B. Smith, Nucl. Instr. and Methods **9**(1960) 49.

[40] S.L. Snyder and F. Marti, Nucl. Instr. and Methods (1995) .

[41] L.H. Harwood, NSCL/MSU Annual Report, (1986).

[42] M.M. Gordon, IEEE Trans. Nucl. Sci., **NS-13**, (1966) 48.

[43] H.G. Blosser. *IEEE Transactions in Nuclear Science*, NS -13:1, 1966.